

# **Spatio-temporal pattern formation in microemulsions under different physical and chemical conditions**

**Dissertation**

zur Erlangung des akademischen Grades

**doctor rerum naturalium**

**(Dr. rer. nat.)**

genehmigt durch die Fakultät für Naturwissenschaften

der Otto-von-Guericke-Universität Magdeburg

von Dipl.-Phys. Patricia Dähmlow

geb. am 13.04.1988 in Magdeburg, Deutschland

Gutachter: Prof. Dr. Ralf Stannarius

Prof. Dr. Harald Engel

Eingereicht am: 25.08.2015

Verteidigt am: 23.02.2016



# Acknowledgments

I wish to acknowledge with a great deal of gratitude all of the people who contributed to this work. Especially, I express my gratitude to my supervisor Stefan C. Müller for giving me the opportunity to work in his group. I like to acknowledge Katja Guttman for helping me to organize a lab, where I was able to perform my experiments and for helpful and inspiring dialogs.

I also thank Vladimir K. Vanag, who invited me to work with him in Kaliningrad for a short period, for his helpful comments and his support to become familiar with the studied system. Jéssica Almeida is acknowledged for fruitful collaboration.

Dr. Wolfgang Jantóß, Dorothea Erndt, Heidrun Wólke, Silvia Simon and Petra Hünerbein, Gregor Nuglisch, Jürgen Weissenborn, Thomas Saar, Dirk Ehrlich, and Diana Ehrlich are acknowledged for their helpful assistance.

My special thanks go to Graduiertenförderung des Landes Sachsen-Anhalt, who gave me the opportunity to realize my research project.

Finally, I thank Tim and my family for their encouragement and support throughout my study.



# Abstract

In this work, pattern formation in the sodium-bis (2-ethylhexyl) sulfosuccinate (AOT) water-in-oil microemulsion is studied, loaded with the ferroin- and the bathoferroin-catalyzed Belousov-Zhabotinsky (BZ) reaction.

Such an emulsion has a close resemblance to living systems such as biological cells. Droplets are surrounded by a surfactant that acts as a membrane. The formed compartments play the role of small reaction chambers, where e. g. energy is produced. Single compartments can interact due to molecules, which interdiffuse among them. This type of interaction between compartments based on a self-induced (chemical) gradient represents the way biological cells communicate.

In the first part of this work, two different solvents are used, creating a set of four cases with differing chemical conditions. In the ferroin-catalyzed case, Turing patterns are found in both solvents. They differ in their interaction with coexisting bulk oscillations. For the bathoferroin-catalyzed BZ reaction, dash waves can be observed in both solvents. A curvature dependence of the splitting and merging of dashes is found. Furthermore, dashes are found to propagate into the gaps of the precursor wave, since the inhibitor is mainly produced in the dashes, such that the trail of the dashes is not excitable, when the next wave front follows.

In the second part, the organic substrate of the BZ reaction is changed to 1,4-cyclohexanedione (CHD), causing anomalous dispersion of waves. This combination of a microemulsion and the BZ-CHD reaction has not been studied before, such that new patterns are found: transient lines, as well as a well-known wave turbulence and an intermediate state.

Transient lines have a variable distance to each other and disappear after a short time. The intermediate state is a mixed pattern of transient lines and wave turbulence. The type of the emerging pattern depends on the initial concentrations of CHD, sulfuric acid and sodium bromate.

Before one of these three types develops, waves or oscillations occur and remain for several minutes. Afterwards, these waves do not leave behind a refractory state, but the system remains excited. This excited state lasts for several minutes during which no patterns are formed.

Finally, Turing patterns are investigated under the influence of an electric field above and below the percolation transition of the system. Above the transition, the electric field induces linear drift of the patterns with increasing electric field strength. However, below the percolation transition, this increase shows a nonlinear behavior. The patterns are observed to reorient under high electrical field strength, such that they are arranged perpendicular to the field lines.



# Zusammenfassung

In dieser Arbeit wird eine oszillierende chemische Reaktion, die Belousov-Zhabotinsky (BZ) Reaktion, in einem aus Kompartimenten bestehenden System untersucht.

Sie dient als Modellsystem für viele musterbildende Prozesse, wie sie in der Natur ablaufen. Als beliebtes Beispiel gilt hier die Dynamik von Erregungswellen auf dem Herzen. Die BZ Reaktion besteht aus mehreren Reaktionsteilnehmern, wie dem organischen Substrat Malonsäure, Natriumbromid, Schwefelsäure und dem Katalysator und Farbindikator Ferroin. Wird diese Reaktion in Kompartimente integriert, so ergibt sich eine völlig neue Dynamik, da das System nicht mehr homogen ist.

Im Falle des untersuchten Systems handelt es sich um eine inverse Emulsion aus Nanometer großen Wassertröpfchen, die in einem Öl schwimmen (Mikroemulsion genannt). In diesen isolierten Tröpfchen läuft die BZ Reaktion ab, und nur durch Zusammenstöße der Tröpfchen findet ein Massenaustausch statt. Die Tröpfchen sind von einer einlagigen Tensidschicht umgeben und schwimmen in einer Ölphase.

Mit diesen chemischen Bedingungen ist es möglich, Turing Muster zu beobachten, wie sie auf Tierhäuten zu finden sind, da der Aktivator der Reaktion deutlich langsamer diffundiert als der Inhibitor. Im Falle der Mikroemulsion ist der Aktivator in den Wassertröpfchen gefangen und diffundiert mit deren Geschwindigkeit. Der unpolare Inhibitor kann die Tensidschicht durchdringen und in die Ölphase gelangen. Damit kann der Inhibitor wesentlich schneller diffundieren, als der Aktivator.

In dieser Arbeit wird die Rezeptur der BZ Reaktion, die in die Mikroemulsion integriert wird, auf verschiedene Arten geändert, wie der Verwendung unterschiedlicher Katalysatoren und Lösungsmittel sowie die Variation des organischen Substrats. Weiterhin wird auch das Verhältnis der Reaktionsteilnehmer zueinander, d. h., deren Konzentrationen geändert. Die Kombination aus BZ Reaktion und Mikroemulsion fördert eine reiche Vielfalt an beobachtbaren Mustern zutage, die in dieser Arbeit untersucht werden.

In der Mikroemulsion gibt es aber auch andere Parameter, die geändert werden können, wie das Verhältnis zwischen Wasser, Öl und Tensid. Dieses Verhältnis beeinflusst die Anordnung der Wassertröpfchen und Tensidmoleküle sowie das Auftreten von Perkolation, also der Bildung eines infiniten Clusters aus Tröpfchen, welcher die Ölphase durchzieht. Perkolation wiederum bestimmt ebenfalls das Auftreten bestimmter Muster.

Die Bedingungen für die Bildung der oben genannten Turing Muster (stationäre Muster) ist in

---

der untersuchten Variante der BZ Reaktion erfüllt, wenn das System nicht perkoliert ist, also sich die Wassertröpfchen frei bewegen können, ohne Cluster zu bilden. Oberhalb der Perkolationsschwelle finden sich dann dynamische Muster in der Reaktion.

In dieser Studie werden zunächst Experimente in der BZ-Mikroemulsion durchgeführt, indem zwei verschiedene Katalysatoren und zwei verschiedene Öle verwendet werden. Somit ergeben sich vier Fälle, deren Muster genauer untersucht werden. Mit dem Katalysator Ferrouin können unterhalb der Perkolationsschwelle Turing Muster gefunden werden; mit Bathoferrouin als Katalysator werden segmentierte Wellenfronten und diskontinuierlich propagierende Erregungswellen beobachtet. Im Fall der Turing Muster wird festgestellt, dass die Interaktion zwischen sich bildenden Strukturen und einer, im System vorhandenen Oszillation, unterschiedlich für beide Öle ist (Turing-Hopf Interaktion). Mit dem Lösungsmittel n-Oktan verschmilzt die Oszillation mit den sich bildenden Mustern. Dies hat zur Folge, dass die Welle aufricht und in zwei gegensätzliche Richtungen propagiert: eine in Richtung der sich bildenden Muster und die andere in die Richtung, aus der die Oszillation kam. Im Falle von Hexan als Lösungsmittel verschmilzt die Oszillation nicht mit den sich bildenden Mustern, sondern formt einen Ring um die schon vorhandenen Strukturen.

Dieser Unterschied in der Turing-Hopf Interaktion liegt an der unterschiedlichen Lösbarkeit von Aktivator bzw. Inhibitor im jeweiligen Öl, was die Diffusion der beiden Substanzen beeinflusst und damit das Auftreten von Turing Mustern.

In den Experimenten mit Bathoferrouin wird beobachtet, dass die Segmente aufeinanderfolgender Wellenfronten immer in die Lücken der vorangegangenen Wellenfront laufen, zu denen sie um die Länge eines Segments versetzt sind. Der Grund hierfür ist, dass der Inhibitor vor allem in den Wellensegmenten gebildet wird und nicht in den Lücken. Somit ist die Spur eines Segments noch nicht wieder erregbar, die Spur der Lücke allerdings schon. Außerdem werden die Segmente länger, wenn sie in einer Welle mit positiver Krümmung laufen, da sich die Segmente so voneinander entfernen. Bei Erreichen einer bestimmten Länge brechen die Segmente in zwei Segmente auf. Ein Effekt des Lösungsmittels konnte nicht gefunden werden.

In weiteren Experimenten wird das organische Substrat, die Malonsäure, durch ein anderes ersetzt, dem 1,4-Cyklohexandione. Diese Chemikalie verhindert die in der Standardreaktion vorkommende Bildung von CO<sub>2</sub> Bläschen und führt zu einer anormalen Dispersionsrelation von Wellenfronten. In der Mikroemulsion wurde dieses Substrat bisher nicht verwendet, sodass die Kombination der blasenfreien BZ Reaktion und der Mikroemulsion in dieser Arbeit untersucht wurde.

In diesem Zusammenhang werden ebenfalls zwei verschiedene Katalysatoren verwendet, jedoch



---

nur ein Lösungsmittel. Beobachtet werden neue Strukturen, die zuvor unbekannt waren. Es konnten drei verschiedene Arten von Mustern gefunden werden, transiente Linien, turbulente Wellen und eine Zwischenstufe. Die Muster waren qualitativ gleich für beide Katalysatoren und ihr Auftreten konnte mit Hilfe des Konzentrationsverhältnisses vorausgesagt werden. Bevor diese Muster auftraten, startete die Reaktion zunächst mit Wellen oder Oszillationen, die nach kurzer Zeit keinen refraktären Zustand mehr hinter der Wellenfront bildeten. Jedoch erscheint eine neue Wellenfront hinter der ursprünglichen Welle, welche die Ursprüngliche dazu veranlasst, schneller zu propagieren als bisher. Die neu entstandene Welle hingegen läuft mit der ursprünglichen Geschwindigkeit der ersten Welle weiter. Ist die ursprüngliche Welle durch Kollision mit einer anderen verschwunden, bildet sich erneut eine Welle in deren Rücken. Nach einer Weile wachsen alle Wellen zusammen, da sie keine refraktäre Phase mehr bilden und das System verbleibt für mehrere Minuten bis zu einigen Stunden im erregten Zustand. In diesem Zeitraum können keine Muster beobachtet werden.

Im letzten Teil dieser Arbeit wird mit elektrischen Feldern gearbeitet. Es geht darum, deren Effekt auf die Muster in der BZ Mikroemulsion zu untersuchen.

Dazu wird die Standard-BZ Reaktion (mit Malonsäure) herangezogen und die Parameter so gewählt, dass stationäre Turing Muster auftreten. Unter einem konstanten homogenen Feld kann die Drift der Muster beobachtet werden. Diese Drift wird unterhalb und oberhalb der Perkolationschwelle untersucht. Oberhalb wird ein linearer Zusammenhang zwischen elektrischer Feldstärke und Driftgeschwindigkeit beobachtet, wie er von der wässrigen BZ Reaktion bekannt ist. Unterhalb hingegen wächst die Driftgeschwindigkeit exponentiell mit der Feldstärke an.

Außerdem kann beobachtet werden, dass sich die Turing Muster senkrecht zum Verlauf der Feldlinien ausrichten, wenn das Feld stark genug ist. Bei geringeren Feldstärken nehmen sie einen bevorzugten Winkel zu den Feldlinien ein.

Des Weiteren werden Experimente mit alternierendem elektrischen Feld gemacht, die allerdings kaum Resultate hervorbrachten, da das untersuchte System zu träge auf die Änderung der Polarität des Feldes reagiert.

Die in dieser Arbeit gewonnenen Erkenntnisse bilden eine solide Grundlage für die Entwicklung synthetischer Zellen. Da in solchen Zellen chemische Reaktionen zur Energiegewinnung in kleinen Kompartimenten (in Analogie zu Mitochondrien oder Chloroplasten) stattfinden müssen, eignen sich die Tröpfchen der Mikroemulsion gut als Modellsystem. Durch Kollisionen der Tröpfchen findet ein Massenaustausch statt und auch die Diffusion einzelner Stoffe kann durch die Wahl von geeigneten Proteinen beeinflusst werden. Auch mit Hilfe von chemischen oder elektrischen Gradientenfeldern lässt sich ein ähnlicher Effekt erreichen. Somit kann die

---

Kommunikation zwischen den Kompartimenten beeinflusst werden. Die Mikroemulsion bildet also auch für das Studium der Funktionsweise intrazellulärer Signalwege eine geeignete Grundlage.

# Contents

<b>I. Introduction and Goals</b>	<b>5</b>
<b>II. Theoretical Aspects</b>	<b>11</b>
<b>1. Reaction-Diffusion Systems</b>	<b>13</b>
1.1. Activator-Inhibitor Systems . . . . .	13
1.2. Excitable Media . . . . .	14
1.3. Turing Patterns . . . . .	15
<b>2. The Belousov-Zhabotinsky Reaction</b>	<b>17</b>
2.1. The Classical Belousov-Zhabotinsky Reaction . . . . .	17
2.2. The Bubble-Free Belousov-Zhabotinsky Reaction . . . . .	18
2.3. Oregonator Model . . . . .	20
2.4. Electric Fields in the Belousov-Zhabotinsky Reaction . . . . .	22
2.4.1. One-dimensional waves . . . . .	22
2.4.2. Two-dimensional waves . . . . .	23
2.4.3. Three-dimensional experiments . . . . .	26
<b>3. Microemulsions</b>	<b>29</b>
3.1. Physical Properties of Microemulsions . . . . .	29
3.2. Pattern Forming Microemulsions . . . . .	31
3.3. Percolation . . . . .	33
3.4. Gradients in Microemulsions . . . . .	35
3.4.1. Temperature . . . . .	35
3.4.2. Electric Fields . . . . .	37
<b>III. Material and Methods</b>	<b>41</b>
<b>4. Chemical Preparation</b>	<b>43</b>
4.1. Preparation of Stock Solutions . . . . .	43
4.2. Preparation of Microemulsions . . . . .	44

<b>5. Experimental Methods</b>	<b>49</b>
5.1. Measurement of Physical Properties . . . . .	49
5.2. Experimental Setup without Electric Fields . . . . .	50
5.3. Experimental Setup with Electric Fields . . . . .	51
5.4. Analysis of Image Data . . . . .	52
<b>IV. Results</b>	<b>57</b>
<b>6. Physical Properties</b>	<b>59</b>
6.1. Electrical Conductivity . . . . .	59
6.2. Droplet Radius . . . . .	60
6.3. Density and Viscosity . . . . .	62
6.4. Discussion . . . . .	63
<b>7. Patterns in the BZ-AOT System with Malonic Acid</b>	<b>65</b>
7.1. Ferriin-Catalyzed BZ Reaction . . . . .	65
7.2. Bathoferriin-Catalyzed BZ Reaction . . . . .	67
7.3. Aging of Microemulsions . . . . .	71
7.4. Discussion . . . . .	73
<b>8. The BZ-AOT system with 1,4-Cyclohexanedione</b>	<b>77</b>
8.1. Excited State . . . . .	78
8.2. Transient Lines . . . . .	81
8.3. Intermediate State . . . . .	84
8.4. Wave Turbulence . . . . .	86
8.5. Discussion . . . . .	87
<b>9. Electric Field Effects on Patterns in a Microemulsion</b>	<b>91</b>
9.1. Effect of the Layer Thickness . . . . .	91
9.2. Electric Field Effects in Microemulsions . . . . .	93
9.2.1. Direct Current . . . . .	93
9.2.2. Alternating Current . . . . .	98
9.3. Discussion . . . . .	99

<b>V. Conclusion and Outlook</b>	<b>103</b>
<b>Bibliography</b>	<b>107</b>
<b>Appendix</b>	<b>115</b>
A.1. Absorption Spectra of the Catalysts . . . . .	115
A.2. Statistical Test of Exponential Increase of Drift Velocity . . . . .	115
A.3. Experiments with 1,4-cyclohexanedione . . . . .	117
<b>Selbstständigkeitserklärung</b>	<b>121</b>
<b>Curriculum Vitae</b>	<b>123</b>



## **Part I.**

# **Introduction and Goals**





---

Pattern formation is one of nature's most fascinating phenomena. Starting with the formation of life, when cells and compartments start to separate and undertake different tasks all the way to the development of structures on animal skins or our finger prints, pattern formation in nature is quite impressive. Every individual has unique patterns, allowing us to precisely identify each animal or human being.

The patterns considered here are called Turing patterns. They were proposed by Alan Turing in 1952 [1] and form stationary patterns that appear only under certain chemical conditions. An example of Turing patterns is shown in Fig. 0.1. Here, the face of a Humphead wrasse is shown, giving a beautiful example of these patterns. The patterns range over the whole body and vary in wavelength. For example the wavelength at its face is much larger than behind its gill cover (right side of the image).



**Fig. 0.1.:** Humphead wrasse with Turing patterns on its face. *Image courtesy of Michael Fricke, Braunschweig.*

However, there are much more patterns, occurring in nature. Some of them are stationary in space, but not in time. They are called oscillons (see Fig. 0.2). Other patterns have both, dynamics in time and space. These are called spatio-temporal patterns with representatives like spiral waves or target patterns. They occur in biological systems and chemical reactions. One of the most important examples, is our heart. The pumping of this dynamic system is governed by cells that produce pulses propagating over the heart muscle. This enables the heart to pump blood through our body [2, 3].

When we think of heart diseases like cardiac arrhythmia, the triggers are spiral waves on the heart muscle, occurring as a consequence of breaking wave fronts from the initial pulse.

Furthermore, spiral waves can be found in biological systems like the cell aggregation of the slime

---

mold *Dictyostelium Discoideum* [4], in the chicken retina [5] and in the cytoplasm of *Xenopus laevis* oocytes [6] and also on the brain surface or cortex, during epilepsy [7] or migraine [8]. In 1959, the first homogeneously oscillating chemical reaction was found by Boris P. Belousov and later modified by Anatoli M. Zhabotinsky [9]. This reaction is called Belousov-Zhabotinsky reaction [10] and acts as a prototype to study spatio-temporal patterns, like spiral waves. An organic substrate (usually malonic acid) is oxidized by bromate in an acidified aqueous medium in the presence of a metal ion catalyst (e. g. ferroin) [11, 12].

In this work, the focus of interest lies on the formation of patterns, as occurring on animal skins and their manipulation. As mentioned above, Turing patterns occur only under certain chemical conditions, namely a certain relation between the diffusion of activator and inhibitor. The transport mechanism in such a system is diffusion-governed and chemical reactions produce the activating species autocatalytically, whereas the inhibitor species counteracts. One can imagine, that differences in diffusion of activator and inhibitor do not occur in an aqueous, homogeneous system. This made the experimental observation of these patterns challenging and took almost 40 years [13] after their prediction by Alan Turing. As a main requirement, the activator must diffuse much slower than the inhibitor. Experimentally, this can only be realized using a "trick". The first system, Turing patterns were observed in, is the chlorine-dioxide-iodine-malonic acid reaction. In that system, the activator is trapped in a gel matrix, which reduces its diffusion significantly [13].

Water-in-oil emulsions filled with the Belousov-Zhabotinsky (BZ) reaction [9, 10] are also suitable to observe Turing patterns, since the activator is trapped in nanometer-sized water droplets (consequently, it has the diffusion coefficient of the droplets) whereas the inhibitor can diffuse freely into the oil phase [14]. However, this works only if the system is not percolated, i. e., no infinite cluster of droplets is present in the system. The ratio between oil and water must be chosen such that water droplets in the system do not form clusters. To stabilize the droplets they are surrounded by a surfactant.

The fascinating thing about Turing patterns is that the pattern forming species are several orders of magnitude smaller than the resulting patterns. On animal skins, pigment cells like melanophores or xanthophores are the pattern forming species [15]. In the BZ microemulsion, they are located in the nanometer-sized water droplets, which form patterns with a wavelength of around 200  $\mu\text{m}$ . These pattern forming species are located in gradient fields, caused for example by differences in concentration of chemical species (e. g. protons). Thus, in this work, electric fields are used as source of these gradients in order to study their effect on Turing patterns. Over the past decades, microemulsion systems (in which Turing patterns can be observed) were

studied thoroughly with many modifications of the system. However, the influence of gradients on this system was rarely studied.

In the microemulsion system, different solvents can be used, as well as different catalysts. Furthermore, the variety of parameters of the chemical reaction is enormous. The ratio ( $\phi_d$ , droplet fraction) between surfactant, oil and water can also be changed to configure different phases in the system and with that, percolation. An overview of patterns occurring in the BZ microemulsion is shown in Fig. 0.2. However, this overview is incomplete. Two different catalysts are used here, which are not labeled in the figure. In the left column and in the upper row, ferroin is used as catalyst, whereas the shown segmented and bubble waves are observed using bathoferroin (BP), which is a derivate of ferroin.

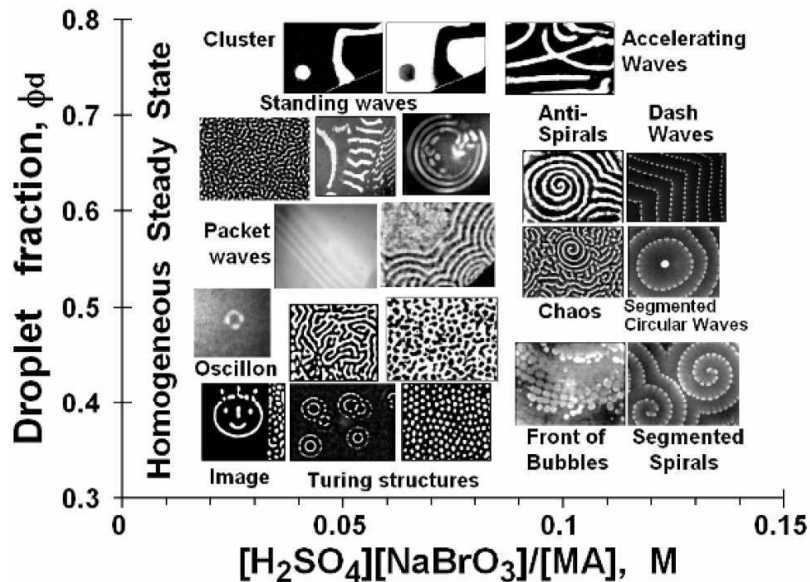


**Fig. 0.2.:** Overview of patterns occurring in the BZ reaction embedded in a microemulsion. The droplet fraction describes the ratio between volumes of water and surfactant and the volume of the entire microemulsion. The patterns in the right column are generated with BP [16].

To become familiar with all these chemical parameters and their effect on the microemulsion system, some of the chemical parameters are changed in this work. Two different solvents and catalysts are used in Sect. 7. Furthermore, the organic substrate of the chemical reaction is changed in Sect. 8. Thus, a new system is created combining the bubble-free BZ reaction and the microemulsion system. This system is studied with the goal of observing new patterns. In the bubble free BZ reaction, anomalous dispersion of the wave fronts can occur. In the standard BZ system, the velocity of a wave decreases with decreasing wavelength (normal dispersion). In the last part, the effect of gradients on Turing patterns is studied using electric fields (Sect. 9). Furthermore, the behavior of all patterns is studied below and above the percolation transition.

---

The microemulsion system with its complexity and its fascinating patterns would already be reason enough to investigate this system. On top of that, studying these patterns under the presence of a gradient field is closely related to pattern formation in nature. The understanding of these basic processes will improve our understanding of nature in general and may allow us to manipulate stationary and dynamic patterns when they are hazardous, such as spiral waves on the heart.

**Part II.**

# **Theoretical Aspects**



# 1. Reaction-Diffusion Systems

In general, reaction-diffusion systems are systems in which locally a chemical reaction takes place. Chemical species are transformed into each other and transported by diffusion [17].

## 1.1. Activator-Inhibitor Systems

Pattern formation in reaction-diffusion systems represents an important phenomenon in biological morphogenesis. In reaction-diffusion systems of the activator-inhibitor type, stationary patterns can occur, as found on animal skins [15]. In these systems, pattern formation occurs spontaneously. The homogeneous system is initially stable. As a result of a perturbation, the system becomes unstable and inhomogeneous, leading to the formation of patterns. The transport of chemical substances happens via diffusion in activator-inhibitor systems.

An activator is produced by autocatalytic processes and an inhibitor counteracts the production of the activator. If the activator diffuses much slower than the inhibitor, Turing patterns can occur. These patterns were first described by Alan Turing in 1952 [1].

The demanding conditions on the diffusion coefficients of activator and inhibitor made it experimentally challenging to observe Turing patterns. The diffusion coefficient of the activator needs to be reduced by a trick. The first experimental observation of Turing patterns was in 1990 in the chlorine-dioxide-iodine-malonic acid reaction, where the activator is immobilized in a gel matrix [13].

Activator-inhibitor systems can be described by the following partial differential equations, with diffusion:

$$\begin{aligned}\partial x / \partial t &= f_x(x, z) + D_x \Delta x, \\ \partial z / \partial t &= g_z(x, z) + D_z \Delta z.\end{aligned}\tag{1.1}$$

The functions  $f(x, z)$  and  $g(x, z)$  describe the reaction dynamics of the system for the coupling between activator  $x$  and inhibitor  $z$ .  $D_i$  represents the diffusion of the corresponding species  $i$  [1, 13]. In reaction-diffusion systems  $f(x, z)$  is a cubic function. The function  $g(x, z)$  is a polynomial of degree one or two. In most models it is a linear function. How the system behaves depends on the position of the functions relative to each other (i.e., where the intersections lie). The intersections of the functions can produce a stable or unstable solution of the system. Thus, it can be oscillating, excitable or bistable [18].

## 1.2. Excitable Media

Excitable media are common in nature. The brain and heart for example belong to this group of systems, since electric pulses propagate through these media [19]. However, excitability can also be found in chemical reactions, like the Belousov-Zhabotinsky reaction [10].

An excitable medium is a spatially distributed, continuous medium, in which a perturbation expands. Excitability means that a small perturbation, which is larger than a certain threshold, results in a macroscopic response of the system. As a consequence, the system proceeds from the excitable into the so-called excited state, which is followed by a refractory state. In this phase, the system does not respond to any further perturbations. After a while, the system returns to the excitable state, in which it becomes susceptible to perturbations again. The coupling in such a system is local and formed by diffusion-like transport [19, 20].

Due to the interplay of diffusion and chemical reactions, waves of excitation can propagate through the medium, forming patterns like spiral waves in space or oscillations in time [10]. Pattern formation in excitable media does not depend on the relation of diffusion coefficients of activator and inhibitor. Thus, it is experimentally much easier to observe pattern formation in these systems.

Propagation of waves in excitable media is governed by the refractory state behind a wave front. If two waves collide, they disappear, since none of them can propagate through the refractory phase of the other wave. Even spiral waves are limited by the refractoriness. Each wave front can only come as close to the precursor wave until it would propagate into the refractory regime of its predecessor.

The propagation velocity of an excitation wave  $v$  is determined by diffusion  $D_x$  and the rate coefficient of the chemical reaction  $k$  of the activator  $x$ :

$$v \sim \sqrt{k_x D_x}. \quad (1.2)$$

Another limiting factor of wave propagation is the dispersion relation of the system. It is defined as the velocity of a wave  $v$  divided by the distance between this wave and a predecessor, i. e., the wavelength  $\lambda$  [21]:

$$\frac{dv}{d\lambda} > 0. \quad (1.3)$$

The velocity of a wave decreases with the distance between the waves [21, 22].

Furthermore, the normal velocity of a wave  $v$  depends on its curvature  $K$ , which is described



by the Eikonal equation:

$$v = v_0 - DK = v_0 - D\frac{1}{r}, \quad (1.4)$$

where  $v_0$  is the velocity of a plain wave and  $r$  the radius of a curved wave. Thus, with increasing curvature, the velocity of a wave decreases [23]. From the Eikonal equation, it is clear that a critical curvature must exist, where wave propagation fails [23]:

$$K_{crit} = \frac{v_0}{D_x}. \quad (1.5)$$

This plays a role in the formation of a spiral wave, since its tip is the region of highest curvature that is possible in the system.

### 1.3. Turing Patterns

The Turing mechanism plays an important role in the formation of patterns on animal skins [15]. Its existence was proposed in 1952 by Alan Turing [1] in a system far from equilibrium. These homogeneous chemical systems require a constant supply of reactants [1]. Furthermore, the chemical reaction needs a positive feedback, e. g. autocatalysis of an activating species and an inhibitory species, which counteracts the activator. These conditions are already fulfilled in some chemical systems as the BZ reaction [10]. However, in this reaction, dynamic structures, such as spiral waves or oscillations, occur instead.

Turing patterns are stationary patterns that are found in systems, where chemical reactions  $f_i$  are coupled with diffusion processes (equation (1.1)). In these systems, a spontaneous symmetry breaking must occur (which is related to bifurcations of stationary state) to allow for the evolution of Turing patterns. The structures are a stable stationary solution of a set of reaction-diffusion equations (1.1) [1, 13].

The special thing about Turing patterns is that the wavelength of patterns is not governed by system geometry, but by the reactant concentrations (or their input rates), the diffusion coefficients and the reaction rates [1]. A dependency on the system size occurs only if the system is smaller than a few wavelengths. This results from the fit to the boundary conditions [1, 13].

However, the most important condition for the formation of Turing patterns is the difference in diffusion coefficients of activator and inhibitor. In homogeneous systems, the diffusion coefficient of activator and inhibitor are almost equal (they lie around  $10^{-5}$  cm s<sup>-1</sup>). To observe Turing patterns, it is necessary that the inhibitor diffuses significantly slower than the activator. Thus,

it was difficult to find experimental evidence of the existence of Turing structures [13].

The first experimental evidence of Turing patterns was found in the chlorine dioxide-iodine-malonic acid (CDIMA) reaction. Here, a chemical inert gel, polyacrylamide, is used to avoid convection. This gel strip was hemmed by two reservoirs of chemical reaction solutions, which diffuse into the gel strip, but do not react separately. Malonic acid is applied on one side and chlorite and iodite on the other side.

A sketch of the experimental setup is shown in Fig. 1.1. Within the gel strip, Turing patterns develop, which are made visible by adding the color indicator  $[I_3^-]/[I_2]$ . This indicator is bound to the gel and cannot diffuse [13, 24].

The patterns in this system consist of bright stripes that run perpendicular to the concentration gradient. With time these stripes break up, forming periodic spots arranged in lines. These patterns can be destroyed by an external perturbation, but rearrange with the same wavelength as before [13].

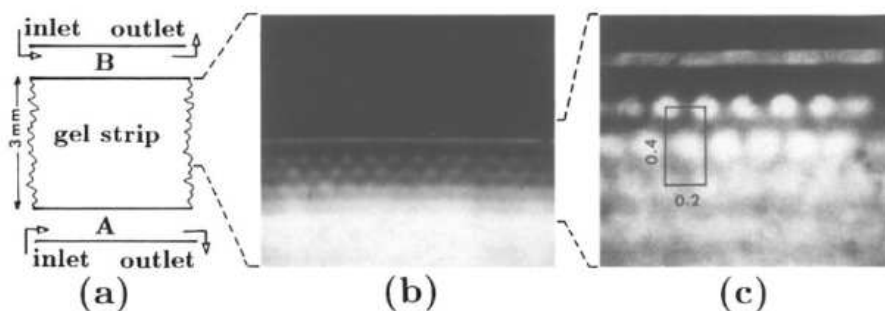


**Fig. 1.1.:** (a) Experimental setup of a gel strip reactor, in which Turing patterns can be found. A and B label the two nonreactive solutions, which are continuously fed. (b) Both solutions diffuse into the gel strip, where they react and form Turing structures. (c) Enlarged image of the region with patterns of (b) with dimensions in mm. The dark regions correspond to the reduced state, whereas the bright regions represent the oxidized state [13].

The patterns in the CDIMA reaction can be affected by temperature gradients and electric fields [13, 25]. Temperature controls the reaction rates and thus, well-defined concentrations are reached [13].

The application of a weak electric field causes a drift of the spots towards the negative electrode, with a constant speed for a given current. An increasing electric current results in an increasing velocity, such that a linear relation between both parameters can be found [25].

Thus, electric fields are able to change stationary Turing patterns, such that they show a time-dependent behavior. This drift suggests that the differential flow is the reason for the destabilization of stationary Turing patterns [25, 26].

## 2. The Belousov-Zhabotinsky Reaction

### 2.1. The Classical Belousov-Zhabotinsky Reaction

The classical BZ reaction is a complex chemical system, where an organic substrate (usually malonic acid) is oxidized by bromate in an acidified aqueous medium in the presence of a metal ion catalyst (e. g. ferroin) [11, 12]. The BZ reaction consist of several chemical reactions, which can be divided into three processes: In the first process, the inhibitor  $\text{Br}^-$  is consumed. When the concentration of  $\text{Br}^-$  falls below a certain concentration, the second process sets in. This process contains the autocatalytic production of the activator  $\text{HBrO}_2$ . Furthermore, the metal catalyst is oxidized in this process, until it is depleted. At this point, the third process sets in, in which malonic acid is brominated and the metal catalyst is reduced. Additionally,  $\text{Br}^-$  is produced in the last process. Due to the increase of its concentration, the first process will be activated [27].

The overall reaction is governed by the oxidation of malonic acid due to bromination [11]



The standard catalyst used in the BZ reaction is ferroin ( $\text{Fe}(1,10\text{-phenanthroline})_3^{2+}$ ), which has a deep red color. In its center, the iron atom is located, surrounded by three ligands of  $\text{C}_{12}\text{H}_8\text{N}_2$ . In its reduced state, it has a positive charge of two. Ferroin is oxidized during the reaction, which results in a positive charge of three. This oxidized form is called ferriin and shows a blue color.

In the two dimensional BZ reaction, patterns like spiral waves, target patterns or simple oscillations can occur. Spiral waves emerge, when an open wave front is created due to a perturbation. This open end can now propagate into several directions, since it receives an additional velocity component at the tip, which is perpendicular to the propagation direction of the wave front. This yields a winding of the wave front, where the open end (spiral tip) remains as the organizing center of the wave.

The wave propagation velocity  $v$  in the BZ reaction depends on proton concentration  $[\text{H}^+]$  and bromate concentration  $[\text{BrO}_3^-]$  [28]:

$$v \sim \sqrt{k_x D_x [\text{H}^+] [\text{BrO}_3^-]}, \quad (2.2)$$

where  $k_x$  is the reaction rate of the activator and  $D_x$  its diffusion coefficient.

For homogeneous oscillations, the initial concentrations of malonic acid, sulfuric acid and sodium bromate must be high compared to the catalyst concentration. In this case, oxidation waves travel through the reduced medium. If the ratio between malonic acid, sulfuric acid, sodium bromate and ferroin changes in a way that ferroin has a high concentration compared to the other three reactants, it is possible to observe reduction waves in the BZ medium [29].

Oxygen inhibits the BZ reaction. It diffuses into the liquid layer and inhibits the reaction within the first two millimeters of the liquid layer. During oxidation of malonic acid by the catalyst, the reaction depends on the oxygen concentration. If atmospheric oxygen diffuses into the reaction, the malonic acid radicals are caught and malonic acid is no longer available for the reaction [30, 31].

## 2.2. The Bubble-Free Belousov-Zhabotinsky Reaction

The classical BZ reaction produces carbon dioxide as a product (compare equation (2.1)). It forms bubbles in the reaction medium, which disturb the structures found in this system. Therefore, they are a severe drawback of this reaction. In the past, several approaches were studied to avoid bubble formation by changing the organic substrate [12]. However, these early approaches do not show the complete range of dynamics known from the classical BZ reaction. Kurin-Csörgei and colleagues [32] demonstrated pattern formation in the BZ reaction with 1,4-cyclohexanedione (CHD) with low catalyst concentration. Thus, they considered ferroin just as an indicator, which means that the studied reaction is an uncatalyzed bromate oscillator (UBO) [32, 33]. This reaction does not form any bubbles, even with high catalyst concentrations. The reaction mechanism of the UBO was extensively studied [32, 33]. Nevertheless, the reaction mechanism of the BZ-CHD reaction is poorly understood.

In the uncatalyzed bromate-CHD-acid oscillator, 1,4-hydroquinone ( $H_2Q$ ) plays a crucial role as an intermediate, which is produced at a constant rate from BrCHD during the overall reaction.  $H_2Q$  is further autocatalytically oxidized to 1,4-benzoquinone (Q) [34]. The different time scales between both reactions, the slow production of  $H_2Q$  and its fast autocatalytic consumption result in oscillatory kinetics [33, 34].

Additional reactions that appear when adding the catalyst makes the system more complex. Reactions between CHD,  $H_2Q$ ,  $HBrO_2$  and ferroin must be included in the considerations [33–35]. CHD is oxidized to Q via several intermediates on two important pathways: by bromate and by catalyst [34]. Furthermore, BrCHD and  $H_2Q$  are also oxidized by the catalyst. In general, the

most important steps in the BZ reaction with CHD are:

- consumption of  $\text{Br}^-$ , which controls the reaction,
- autocatalysis of  $\text{HBrO}_3$  with its two pathways (by bromination and catalyst),
- and the renewal of  $\text{Br}^-$  and  $\text{H}_2\text{Q}$ .

In the uncatalyzed system (i. e., UBO)  $\text{H}_2\text{Q}$  governs oscillations through its formation and autocatalytic consumption. If the concentration of the catalyst is high enough,  $\text{H}_2\text{Q}$  and  $\text{Br}^-$  are produced sufficiently, such that the oscillations of the uncatalyzed oscillator are suppressed by a clock reaction behavior [34].

Wave pulses in the BZ reaction underlie a dispersion relation, which is the relation between the velocity of a wave  $v$  and the distance between this wave and the leading pulse, i. e., the wavelength  $\lambda$  [21]. Most excitable systems, such as the classical BZ reaction show normal dispersion, which means that the velocity of a wave decreases with the distance between the waves [21, 22]. The minimum distance between wave pulses is limited by the refractoriness behind a precursor wave. This shows that the dispersion relation is coupled to the activator and inhibitor species of the reaction. Due to the autocatalytic production of the activator, an excitation pulse occurs. This is, however, limited by increasing inhibitor concentration [22, 36]. Thus, a refractory state is formed behind a wave pulse.

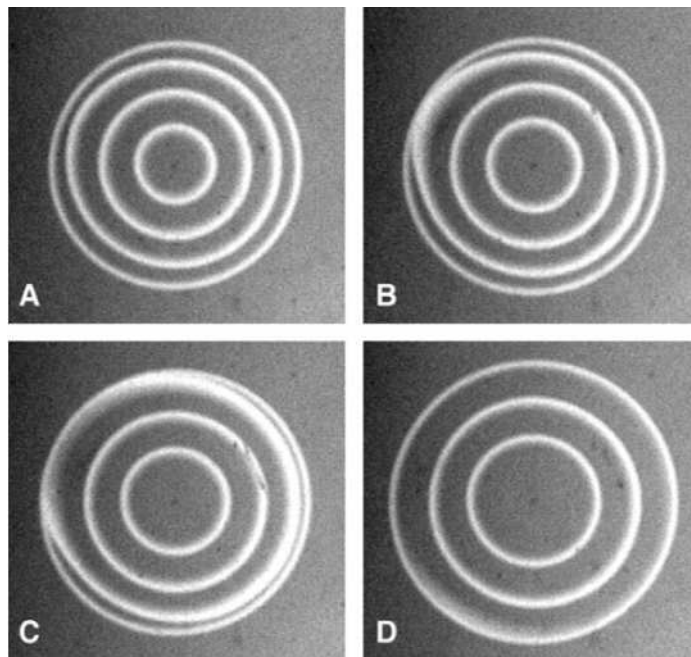


**Fig. 2.1.:** Snapshots of merging waves. The inner pulses of a target pattern in the bubble-free BZ reaction come close to the wave front and merges with it. Image size:  $13.8 \times 13.0 \text{ mm}^2$  [37].

In the BZ reaction with CHD as the organic substrate, anomalous dispersion can be found [22, 35, 37, 38]. This means that the velocity of a wave increases with decreasing wavelength ( $dv/d\lambda < 0$ ), which is true for wave trains. In other words, the leading pulse propagates slower than the following waves. Consequently, the distance between them decreases. This often results either in a merging [Fig. 2.1] of waves, which means, that faster propagating waves behind the leading pulse merges with the latter [22]. In another scenario, the following waves can stack behind the leading pulse [Fig. 2.2] and some kind of traffic jam can be observed [22].

Whether stacking or merging of the waves can be observed depends on the bromate concentration [22]. Low concentrations lead to merging of waves as shown in Fig. 2.1. At a high concentration, merging is prevented by decreasing propagation velocity of the waves when the distances between the wave pulses becomes smaller. However, in both cases, the waves have to propagate into the refractory state of the precursor wave.

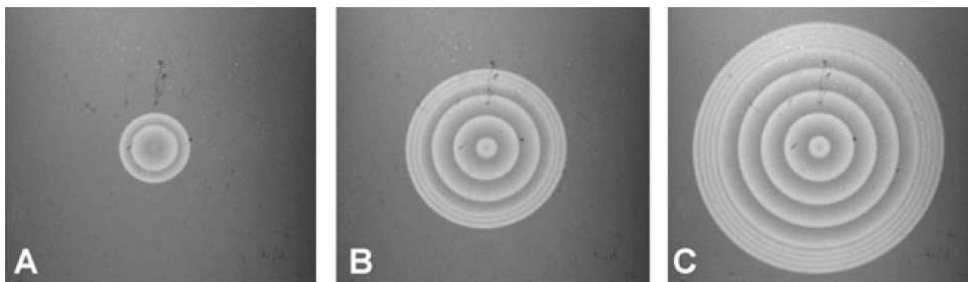
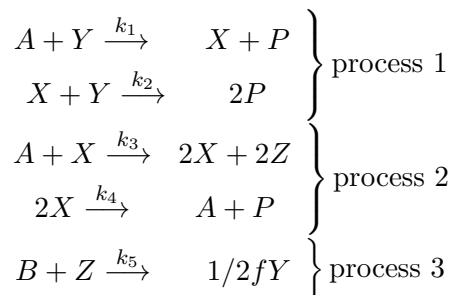


**Fig. 2.2.:** Snapshots of stacking waves of a target pattern in the bubble-free BZ reaction. The circular waves stack behind the outer one. Image size:  $25.3 \times 22.6 \text{ mm}^2$  [37].

## 2.3. Oregonator Model

The Oregonator is a model, developed especially for the BZ reaction by Field and Noyes in 1974 [28]. It consists of five reaction equations with six chemical species:



where  $A = \text{BrO}_3$ ,  $P = \text{HOBr}$  or  $\text{BrCH}(\text{COOH})_2$ ,  $X = \text{HBrO}_2$ ,  $Z = \text{Fe(III)}$  or  $\text{Ce(IV)}$ ,  $Y = \text{Br}^-$ ,  $f =$  stoichiometric factor,  $B = \text{CH}_2(\text{COOH})_2$  and  $k_i =$  rate parameter [39].

This model assumes, that  $A$ ,  $B$  and  $P$  are constant, because they are present in much higher

concentrations than the intermediates  $X$ ,  $Y$  and  $Z$  [39].  $X$  represents the activator species and  $Z$  the inhibitor species. The first reaction in process 2 contains the autocatalytic step, which indicates the inhibition process via process 3 until it ends in the last reaction in process 1 [39]. The resulting differential equations from the above mentioned model reactions are given in the following:

$$\begin{aligned}\frac{dX}{dt} &= k_1AY - k_2XY + k_3AX - 2k_4X^2, \\ \frac{dY}{dt} &= -k_1AY - k_2XY + 1/2fk_5BZ, \\ \frac{dZ}{dt} &= 2k_3AX - k_5BZ.\end{aligned}\tag{2.3}$$

When rescaling these equations [40], one ends up with the following equations:

$$\begin{aligned}\epsilon \frac{dx}{d\tau} &= qy - xy + x(1 - x), \\ \epsilon' \frac{dy}{d\tau} &= -qy - xy + fz, \\ \frac{dz}{d\tau} &= x - z.\end{aligned}\tag{2.4}$$

The scaling relationships and parameters in (2.4) are  $x = 2k_4X/(k_3A)$ ,  $y = k_2Y/(k_3A)$ ,  $z = k_5k_4BZ/(k_3A)^2$ ,  $\tau = k_5Bt$ ,  $\epsilon = k_5B/(k_3A) = 9.90 \times 10^{-3}$ ,  $\epsilon' = 2k_5k_4B/(k_2k_3A) = 1.98 \times 10^{-5}$ ,  $q = 2k_1k_4/(k_2k_3) = 7.62 \times 10^{-5}$  and with  $A = 0.06$  M,  $B = 0.02$  M,  $[H^+] = 0.8$  M and  $k_5 = 1$  M<sup>-1</sup>s<sup>-1</sup> [39, 40].

Equation (2.4) can be simplified, since  $\epsilon'$  is much smaller than  $\epsilon$  (steady-state approximation) [39, 41]. As a result,  $y$  can be written as

$$y_{ss} = \frac{fz}{q + x},\tag{2.5}$$

and (2.4) reduces to:

$$\begin{aligned}\epsilon \frac{dx}{d\tau} &= x(1 - x) - \frac{fz(x - q)}{q + x}, \\ \frac{dz}{d\tau} &= x - z.\end{aligned}\tag{2.6}$$

These are the final equations for the Oregonator system.

The chemistry of the BZ reaction is governed by the concentration of HBrO<sub>2</sub> ( $x$ ). If  $x$  jumps between high and low values, oscillations can be observed in the BZ reaction. This is reproduced in the relaxing nature of the Oregonator oscillator [39].

Propagating waves of excitation in the reaction are reflected by high  $x$ . They are found if the diffusion coefficients of activator and inhibitor are almost equal [42]. Turing patterns can also be found in the Oregonator model, if  $D_z > D_x$  [43]. This makes the Oregonator model suitable to simulate patterns of the BZ reaction embedded in a microemulsion, with appropriate modifications [16, 44].

## 2.4. Electric Fields in the Belousov-Zhabotinsky Reaction

Electric fields have large effects on the BZ reaction. Due to the large number of charge carriers in the chemical reaction, electric fields can act on the propagation direction of waves.

In this chapter, the effect of electric fields is described in one (Sect. 2.4.1), two (Sect. 2.4.2) and three dimensions (Sect. 2.4.3).

### 2.4.1. One-dimensional waves

In one dimension, an electric field can reverse the propagation direction of a wave [45, 46].

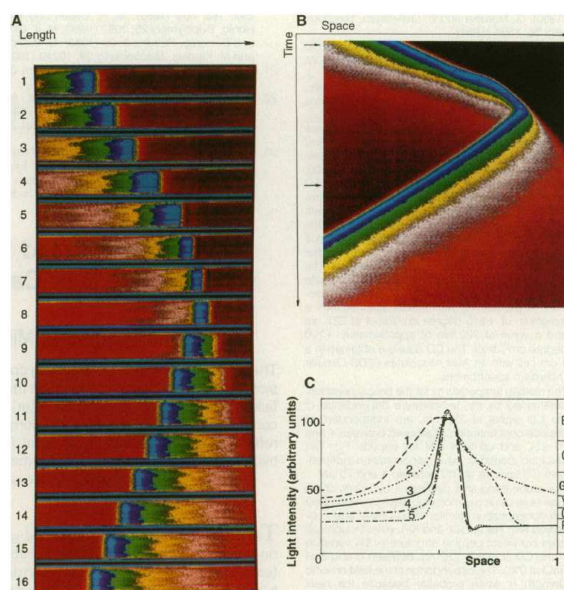


**Fig. 2.3.:** (a) Reversal of a chemical front in the quasi one-dimensional BZ reaction under the effect of an electric field. The wave travels in a rectangular cuvette and is monitored from the side. The time series of images is taken at 16 s intervals. The electric field is initially oriented from the cathode on the left to the anode on the right. After time step 3, the polarity is changed. The negative electrode exerts a repulsive force against the negatively charged bromide ions in the wave front, forcing the wave to reverse its propagation direction. (b) Corresponding time-space plot. (c) Evolution of the profile of the wave front during reversal [46].

This reversal is remarkable, since waves of excitation are followed by a refractory state, which technically does not allow any backward motion. However, the electric field can force a wave to



reverse its direction [Fig. 2.3]. When the polarity is chosen in the way that the wave travels towards the positive electrode, the propagation velocity is reduced, since the field is counteracting the overall motion of the negatively charged bromide ions. A reversal of a wave is induced if the strength of the field is sufficiently high. Thus, the field causes the front to move backwards with respect to its original propagation direction [45, 46].

Furthermore, it may also occur that at the point of reversal, the wave splits into two parts: one of them continuing to propagate along the original path, the other reversing its direction [46]. Reversal and splitting of an excitation wave demonstrate the large influence of electric fields on wave dynamics that normally organizes itself. Under the influence of an electric field, a transient bistable situation occurs at the reversal point, which offers the possibility to choose between two directions for further traveling. This change in the local dynamics of the system is evoked by the interaction of an electric field of proper intensity and polarity with the concentration gradients along the traveling wave [46].

#### 2.4.2. Two-dimensional waves

The dynamics of waves in one dimension is restricted to forward or backward motion. In two dimensions (thin layers), however, more complex patterns like spiral waves, target patterns or even wave turbulence and irregular decomposition patterns can occur [47, 48].

The effect of an electric field on spiral waves is very interesting, since the chirality of the spirals becomes an additional parameter [48]. Fig. 2.4 shows a pair of counter-rotating spirals that is affected by an electric field. The negative electrode is located at the bottom side of Fig. 2.4(c). The corresponding trajectory of the drifting spiral tips is given in Fig. 2.4(a). It shows a clear drift towards the negative electrode. The trajectory is not a straight line, but consists of a continuous track with successive loops. Here, the relative distance of the spiral tips increases, due to the chirality [48]. Although the trajectories of both spirals point towards the bottom side of Fig. 2.4(c), one finds that the clockwise rotating pattern is also pulled to the left, while the counterclockwise rotating wave is pulled to the right. The velocity of the spiral drift depends linearly on the electric current, as depicted in Fig. 2.4(b).

Another phenomenon produced by the drift of spirals is the deformation of the initially Archimedian shape (i. e., constant pitch) of the spiral wave [48]. The deviations from the unperturbed wavelength reach a maximum in the back of the drift direction (compare Fig. 2.4(c)). Apparently, the different wavelengths in the upper and lower part of this image appear due to the Doppler effect.

Changing the polarity of the electric field in Fig. 2.4 causes a drift back towards the initial

locations. Nevertheless, how close the spirals come together depends on the distance between the spiral tips. If they move towards each other and reach a certain distance, spirals continue with a parallel drift [49]. The spirals can get as close as less than one wavelength. Thus, a repulsive force between the spirals exists, which depends on the mutual distance between the spiral cores [49].

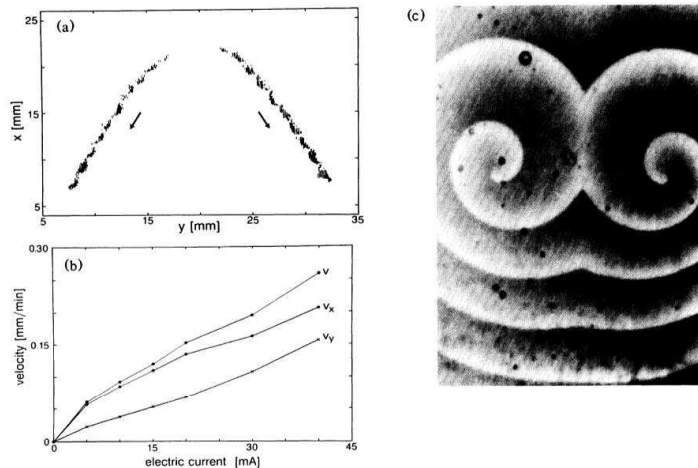


**Fig. 2.4.:** Electric field induced drift of a pair of spiral waves in the ferroin-catalyzed BZ system. Field lines are parallel and oriented vertically with the anode located at the bottom side of (a). (a) Trajectory of the spiral tips of a counter-rotating spiral pair. (b) The velocity of the drift  $v$  depending on the electric current.  $v_x$  and  $v_y$  are the components of  $v$  in  $x$  and  $y$  direction, respectively. (c) The electric field induces a drift towards the anode and a distinct deformation of the Archimedean spiral geometry due to the Doppler effect [48].

Spiral waves can move towards each other, when the polarity and strength of the electric field is appropriate. Under certain conditions, they can also collide [Fig. 2.5]. In this figure, a sequence of four snapshots illustrate such a spiral wave collision. The initial pattern (a) is a pair of counter-rotating spiral waves that have almost identical size and phase. A constant electric field is applied to the spirals with the anode located parallel to the right side of a subfigure. The field causes a drift of the counter-rotating spirals towards each other. Below a critical distance ( $\ll$  wavelength) the spiral tips annihilate, which ends in a removal of the spirals from the system [Fig. 2.5(b) and (c)]. A pacemaker remains, which has a lower frequency than the spirals [Fig. 2.5(d)]. Bulk dynamics in this BZ system are, in fact, not excitable but oscillatory, with rather long oscillation periods. However, due to the higher frequency of a spiral, these oscillations have been suppressed. The collision of a spiral pair has led to its annihilation and eventually to the creation of a target pattern with its pacemaker located in the spiral collision region.

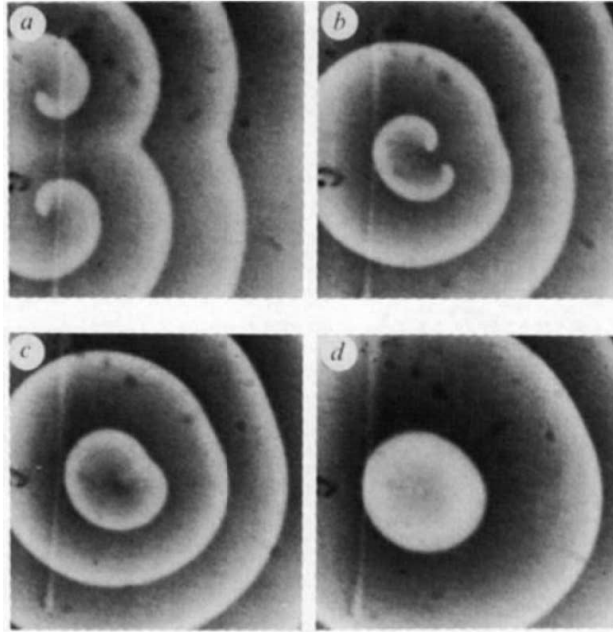


**Fig. 2.5.:** Annihilation of a pair of counter-rotating spiral waves due to an electric field induced drift. The electric field is oriented horizontally (anode on the right). (a) The spiral tips are close together and (b) further reduce their relative distance. (c) Below a certain critical size, annihilation occurs. (d) After collision, a pacemaker is formed in the central region of spiral wave annihilation [50].

In the last paragraph, only continuously constant electric fields have been considered. However, experiments with pulses of electric current and alternating electric fields were also performed in the past.

Spiral waves can be manipulated with pulses of current applied at the spiral tip. This results in a successively increasing and decreasing core size [51, 52]. The motion of the spiral tip becomes meandering, when stepwise pulses of electric current are applied. This leads to a formation of superstructures and the spiral shows an asymmetric shape. Such super-spirals can be considered as the outcome of the approach between wave fronts of the initial spiral. Thus, the wave period changes periodically with time and the Doppler effect makes its contribution [51].

Furthermore, wavelength and period of the spiral wave increase by a factor of three with the application of electric current. The same effect can be found with the application of direct as well as alternating current [52].

The core size increases, since the needle electrode is immersed in the core region of the spiral. Thus, the inhibitor concentration increases near the metal electrode and with that the voltage. The higher voltage induces an electrostatic screening effect around the needle electrode. Even a hysteresis effect can be observed, when the electric current is turned off. When the voltage is decreased, the period of the wave lies not on the same curve as with increasing voltage. This occurs, since the period of a spiral wave becomes larger than the period of an autonomous

pacemaker in the system due to the application of an electric field. Thus, the space required by the spiral reduces with time [52].

In a later work from 1994, the authors were able to induce resonance in spiral waves [53]. In this work, an alternating electric field was applied, which had twice the frequency of the vortex rotation. With that, a drift of the vortex was induced, that does not coincide with the direction of the electric field. The vortex drifts along a straight line.

When the polarity of the electric field oscillates, the spiral would not drift. Since a positive polarity displaces the charge carriers into one direction and a change in polarity would yield a displacement into the opposite direction, the total movement is zero. Nevertheless, a drift was observed. The chosen frequency of the polarity changes with twice the frequency of the vortex rotation. Thus, the oscillations of the electric field and the vortex rotation are synchronized. Therefore, positive polarity affects only the normal velocity of the vortex while the negative polarity affects the growing velocity. Hence, the effect of the electric field differs for both components and the symmetry of space is broken, such that a drift in a selected direction occurs [53].

### 2.4.3. Three-dimensional experiments

In three dimensions, extended spiral waves can occur. These waves are called scroll waves and can be interpreted as a stack of spiral waves, which are organized by the filament, i. e., the line connecting the spiral cores. When the filament has a circular shape, the waves are called scroll rings.

Under the effect of an electric field, scroll rings show a reorientation of the filament [54, 55]. However, they are not stable in an unperturbed system and far away from the boundary [54, 56]. They contract and annihilate after some rotations. An electric field causes a reorientation with respect to the direction of the applied current [54, 55]. Depending on the initial angle between the vector of the scroll ring  $\mathbf{S}$  and the vector of the electric current  $\mathbf{J}$ , the scroll ring is stable or reorients. The latter scenario is shown in [Fig. 2.6]. The direction of the applied current points to the right side of the figure and the reorientation is accompanied by a linear drift towards the positive electrode (to the left of the figure) [54, 55].

Different initial angles  $\alpha$  were used to study the stability of the filament plane alignment. For an angle between  $\mathbf{J}$  and  $\mathbf{S}$  in the interval of  $6^\circ < \Theta < 180^\circ$ , scroll rings are found to change their orientation. When  $\Theta = 0^\circ$  or  $\Theta = 180^\circ$ , the orientation of the scroll rings remains unchanged. However, every  $\Theta > 6^\circ$  leads to an increase of the angle towards  $180^\circ$ .  $\Theta = 0^\circ$  is an unstable stationary state, whereas  $\Theta = 180^\circ$  is a stable one [54, 55].

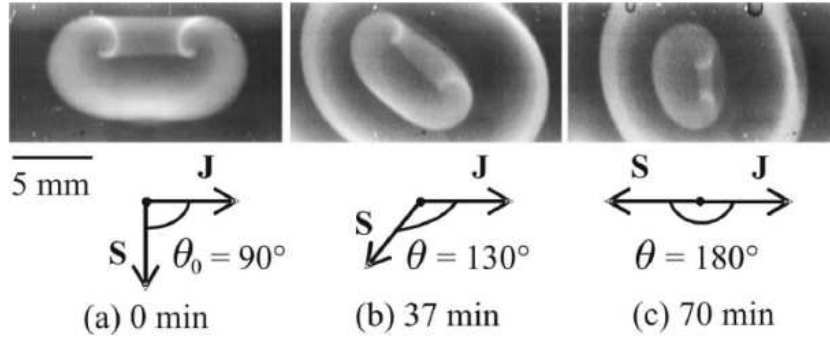


**Fig. 2.6.:** Reorientation of a scroll ring under an applied electrical current in the three-dimensional BZ reaction (lateral view). The circular filament, which connects the spiral tips, is located horizontally, i. e., parallel to the vector of the current  $\mathbf{J}$ . With time, the filament plane turns, such that it becomes perpendicular to the current vector ( $\mathbf{S}$  becomes antiparallel to  $\mathbf{J}$ ) [55].



# 3. Microemulsions

## 3.1. Physical Properties of Microemulsions

Water-in-oil microemulsions formed with non-ionic and ionic surfactants (to stabilize the system) were extensively studied in the past decades [57, 58]. The formation of such a microemulsion is driven by entropy, since the development of the interface between water and oil requires only little work [59]. It is known, that the microemulsion with sodium-bis (2-ethylhexyl) sulfosuccinate (AOT) as surfactant shows the  $L_2$  phase over a wide range [Fig. 3.1]. In this phase, the microemulsion consist of spherical water droplets, surrounded by a monolayer of the surfactant [59].

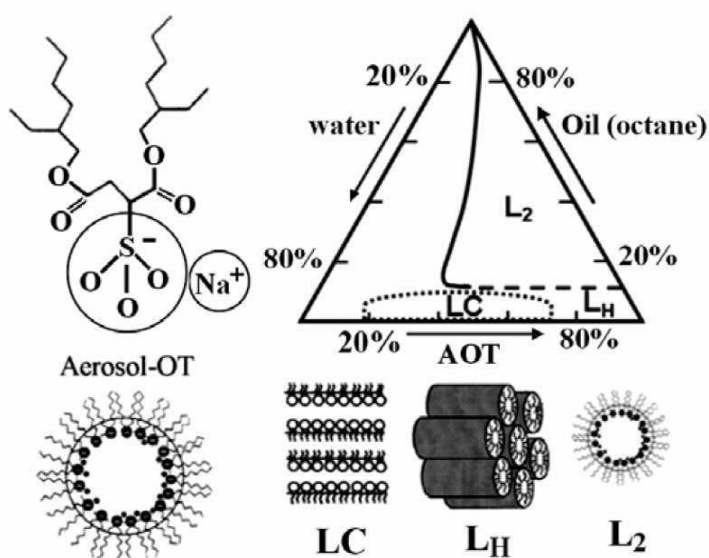


**Fig. 3.1.:** Left: Sketch of the surfactant AOT with its polar head group  $\text{SO}_3^-$ . Right: Phase diagram of the water-AOT-oil system. The  $L_2$  phase is a reverse microemulsion (water-in-oil microemulsion), in which most of the experiments in this work are performed.  $L_H$  – hexagonal phase;  $L_C$  – lamellar phase (liquid crystal) [16].

A water-in-oil microemulsion consists of nanometer-sized water droplets, that execute Brownian motion in the oil phase. They can collide and merge, such that they form droplet clusters, which can split again. As the solvent, a saturated hydrocarbon is used, like n-octane or hexane. The microemulsion is thermodynamically stable, since a surfactant (AOT in this case, which is a strong electrolyte) surrounds the water droplets. AOT is an anionic surfactant consisting of a polar head group ( $\text{SO}_3^-$ ) and two hydrophobic tails [Fig. 3.1]. The sodium ions in the head group form a semi-diffusive electric double layer inside the droplets. The anions of the surfactant are

accumulated at the water/oil interface. Thus, the AOT molecules form a monolayer around the water droplets [60].

Properties of an emulsion are determined by two parameters: The molar ratio between water and AOT concentration  $\omega$

$$\omega = \frac{[H_2O]}{[AOT]}, \quad (3.1)$$

and the volume droplet fraction of the dispersed phase  $\varphi_d$ . This is the ratio of the sum of the individual volumes of water ( $V_W$ ) and AOT ( $V_{AOT}$ ) and the entire volume of the emulsion:

$$\varphi_d = \frac{V_W + V_{AOT}}{V_W + V_{AOT} + V_{oil}}. \quad (3.2)$$

Depending on the ratio between water, oil and surfactant, the microemulsion system can show different configurations, as shown in Fig. 3.1. Most experiments presented in this work are performed in the  $L_2$  phase, where the water droplets move freely in the oil phase. With the help of  $\omega$ , the droplet radius  $R_w$  of the water core can be estimated with the empirical equation

$$R_w[nm] = 0.17\omega. \quad (3.3)$$

This relation means, that a constant area of the monolayer is occupied by the surfactant [61].  $R_w$  is the radius of the water core in the droplets, without the AOT-molecule [62]. To calculate the radius of the droplet including the surfactant, the length of the AOT-molecule must be added ( $\approx 1.1$  nm) [44, 63].

Most of the physical properties of microemulsions are governed by the droplet fraction  $\varphi_d$  and show a threshold-like behavior. This occurs due to percolation of the system. With increasing amount of water, the droplets start to form clusters until water channels pervade the entire medium. This happens around a droplet fraction of 0.5 ( $\varphi_d \approx \varphi_{cr}$  [44]; for details see Sect. 3.3). Due to percolation, viscosity and electric conductivity show a threshold-like behavior. For  $\varphi_d \ll \varphi_{cr}$ , the droplets move nearly free in the oil phase. The emulsion has a high viscosity due to the large amount of oil and its electric conductivity is close to that of pure oil (around  $0.02 \mu\text{S cm}^{-1}$  for  $\varphi_d = 0.25$  [64]).

Nanodroplets in pure water-in-oil microemulsions can carry positive or negative excess charges generating a higher conductivity due to diffusion of the droplets [65]. In microemulsions loaded with the BZ reaction, the electric conductivity is again higher than in pure ones without the BZ reaction (around  $0.5 \mu\text{S cm}^{-1}$  for  $\varphi_d = 0.23$  [66]).



For pure water-in-oil microemulsions the following equation describes the electric conductivity [65]:

$$\sigma = \frac{\epsilon_0 \epsilon k_B T \varphi_d}{2\pi\eta R_d^3}, \quad (3.4)$$

( $\epsilon_0$  - dielectric permittivity,  $\epsilon$  - dielectric constant of the solvent (1.962 in n-octane [67]),  $k_B$  - Boltzmann constant,  $T$  - temperature,  $R_d$  - droplet radius and  $\eta$  - dynamic viscosity).

Coming closer to the percolation threshold, the viscosity increases by one or two orders of magnitude and the conductivity increases by four to five orders of magnitude, since the electric current can flow directly through the water channels [44].

The diffusion of the water droplets  $D_d$  can be described using the Stokes-Einstein equation:

$$D_d = \frac{kT}{6\pi\eta R_d}, \quad (3.5)$$

where  $k$  is the Boltzmann constant,  $T$  - temperature,  $\eta$  - dynamic viscosity of the solvent and  $R_d$  the droplet radius including AOT-molecules.

The substances dissolved in the droplets have almost the same diffusion coefficient as the droplet itself.

## 3.2. Pattern Forming Microemulsions

Microemulsions loaded with the BZ reaction show a whole zoo of patterns, which can be dynamic or stationary (compare Fig. 0.2). The BZ reaction takes place inside the water droplets. Mass exchange is realized by collisions of the droplets. The characteristic time for mass exchange lies in the range between  $10^{-4} - 10^{-2}$  s. Thus, it is some orders of magnitude smaller (seconds to minutes) as in the aqueous BZ reaction [44]. The above mentioned variety of parameters is also a result of the use of two different catalysts in the reaction, ferroin and BP (which is a derivate of ferroin).

With BP, dash waves, as well as discontinuously propagating waves can be found, which develop from spiral waves or target patterns. Jumping and rotating waves are thick waves, which occur in front of a smooth wave front (without any visible connection to this front) and turn around this front, until they encompass the predecessor wave. From these waves, bubble waves can develop, which have no closed wave front, but consist of many spots, propagating almost like a wave [44, 68].

Dash waves also develop from a smooth wave front that splits up, such that coherently mov-

ing wave segments separated by lateral gaps occur [44, 68]. The segmentation of wave fronts always starts near the center of a spiral, since the curvature is highest there. In the dashes, the inhibitor is predominantly generated. It is diffusing faster than the activator, suppressing the autocatalytic reaction in the neighboring gaps [69].

Before segmentation of the front, an instability transverse to the wave front ("ripples") may occur through lateral inhibition or a kinetic interaction of the wave with a reactant in front of it. The concentration of the activator increases at the crests (leading parts of the propagaing wave) of the wave, but decreases at the valleys (lagging parts) [70]. This instability, however, does not lead to a wave breakup with a slow diffusing inhibitor, but with a fast diffusing one [71–74]. A segment (dash) can split up further, when reaching a certain length.

With ferroin, dash waves occur only above the percolation transition, whereas with BP, they can be found below and above the percolation transition [75].

In the BZ-AOT system, Turing patterns can be found [14], since the activator ( $\text{HBrO}_2$ ) is trapped in the droplets and the non-polar inhibitor ( $\text{Br}_2$ ) is able to diffuse into the oil phase. Thus, the diffusion coefficient of the inhibitor is much higher than that of the activator [1, 16, 76].

When the droplet cluster becomes infinite, such that a transient network of water channels is formed, the system is percolated. This happens around  $\varphi_d \approx 0.5$  [68].

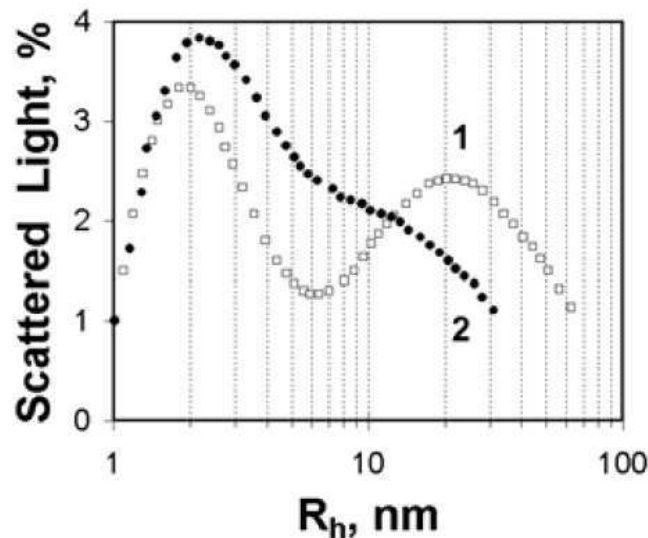


**Fig. 3.2.:** Distribution of droplet radii in the BZ-AOT system of (1) a freshly prepared and (2) of an one day old microemulsion, measured by means of dynamic light scattering [16].

Percolation yields a bimodal distribution of droplets radius (see Fig. 3.2) [77, 78], which favors the formation of discontinuously propagating waves (like jumping, rotating and bubble waves)

and dash waves [68, 77].

A bimodal distribution of the droplet radius occurs only in freshly prepared microemulsions [Fig. 3.2]. This shows that not only single nanodroplets are present in the system but also some larger droplets or droplet clusters. The rate of mass exchange between the droplets within a cluster lies in the range of  $10^3$  to  $10^5$   $\text{M}^{-1}\text{s}^{-1}$ , which means that the BZ reaction is slower in the microemulsion than in the aqueous reaction [79].

If the microemulsion is kept for some days, the two peaks will form a single one and the microemulsion becomes monodisperse [16].

Experiments with the BZ-AOT system are always performed in thin layers of 80 to 100  $\mu\text{m}$ , to avoid three-dimensional effects. The characteristic wavelength of Turing patterns found in this system lies around 200  $\mu\text{m}$  [66, 80]. Thinner layers cannot be used, since the contrast would be worse. Additionally, though exciting waves in the BZ reaction are not able to propagate in layers much thinner than 100  $\mu\text{m}$ . In this range, boundary effects play a role and the diffusion on the boundaries will significantly affect the reaction dynamics [81].

### 3.3. Percolation

Percolation in general means that components of a system form connected clusters. If a cluster reaches all ends of a system, the latter is percolated. Some practical examples are water in a coffee filter or forest fires and their models [82].

A forest is considered, with the trees located on the points of a grid. The density of trees is the order parameter of the system and called  $p$ . Some trees do not have any neighbors ( $p$  close to zero) and other trees have many ( $p$  close to one). If a fire breaks out, the trees with a few neighbors are destroyed by fire, but cannot torch other trees and the fire stops. Around  $p$  close to one, each line of trees can torch the next one. Intuitively, a critical value  $p_c$  exists, where exactly one path appears on which each tree can precisely torch the next one until the fire reaches the opposite end of the grid. This line is called minimal or chemical path. A system is percolated if at least one of these lines appears [82].

In water-in-oil emulsions percolation can also take place, namely when the amount of water is increased. The droplets start to form clusters, which become as large that they pervade the oil phase. A condition for this scenario is the minority of water compared to oil [61, 83]. The order parameter in this system is the droplet volume fraction of the dispersed phase  $\varphi_d$  (equation (3.2)). Most of physical properties of a emulsion depend on this droplet fraction  $\varphi_d$  and show a threshold-like behavior, which is caused by percolation ( $\varphi_{cr} \cong 0.5$ ).

The percolation process in the emulsion system is governed by an increase of the cluster size, the attractive interactions and the mass exchange [84]. In other words, there are so many water droplets present in the oil that they coalesce faster than they separate. Thus, transient water channels are formed in the oil, fully pervading the oil phase [44].

The percolation threshold  $\varphi_{cr}$  is reached if the first infinite droplet cluster is formed. Above this threshold, the number of such clusters increases rapidly [84]. Below and far away from the percolation threshold, water, the used surfactant AOT and droplets diffuse with almost the same velocity, such that the conductivity of this system can be described with the charge fluctuation model [65, 84]. In this model, the electric conductivity is explained with electrophoretic migration of charged droplets in an electric field [65, 84]. During percolation process, only the transport of cations contributes to the conductivity. However, above the percolation threshold, anions and cations migrate within a cluster and the conductivity increases [84].

In a microemulsion loaded with the BZ reaction, much more charge carriers, such as protons, are present in the system. Some products of the BZ reaction, such as molecular bromine  $\text{Br}_2$  and the radical  $\text{BrO}_2^\bullet$ , which are inhibitors of the system, are soluble in the oil phase and can diffuse out of the droplet. Thus, their diffusion coefficient rises by 10 to 100 of the original value while that of the activator (trapped in the droplets) remains constant. Hence, the conditions for the occurrence of Turing patterns are fulfilled (compare Sect. 1.1) [44].

In the BZ-AOT microemulsion below the percolation transition, Turing patterns can be observed. When droplets start to form clusters, the monolayer of AOT can open up, leading to an exchange of water between the droplets. The diffusion coefficient of the activator starts to increase [16]. In this regime, Turing patterns can still be observed [80]. Above the percolation transition, a bimodal distribution of the droplets radius is found [Fig. 3.2] [77, 78], favoring the formation of discontinuously propagating waves (like jumping, rotating and bubble waves) and dash waves [68, 77]. The latter develop from a smooth wave front, which splits up such that coherently moving wave segments separated by lateral gaps occur [44, 68].

However, the percolation process in a system appears in a continuous fashion, starting with local cluster formation until these clusters are distributed over the whole medium. If the terms "above" and "below the percolation threshold" are used for the studied system, it provides just a rough estimation of the state of the system. Saying "below the percolation threshold" means that cluster formation might just have started, whereas it is probably not fully completed "above the threshold". Thus, in terms of  $\varphi_d$  the threshold must be estimated for each used recipe.

Additionally, the percolation threshold can be shifted if a temperature gradient or an electric field is applied [84, 85] (see Sect. 3.4).

## 3.4. Gradients in Microemulsions

### 3.4.1. Temperature

Temperature induced percolation can be observed by measuring static electric conductivity and viscosity [61]. However, the way the system behaves when percolation takes place furthermore depends on the surfactant. A non-ionic surfactant (Igepal CO-520, for example) behaves differently than AOT does [59].

The structure of a microemulsion on the microscopic level strongly depends on the temperature. A change by a few degrees already results in a rapid increase of electric conductivity [61].

The geometric structure of the surfactant molecule in the monolayer also plays an important role. The surfactant is formed like a wedge. In the case of water droplets in oil, the tails of the surfactant have lots of space and the thick end of the wedge points towards the oil phase.

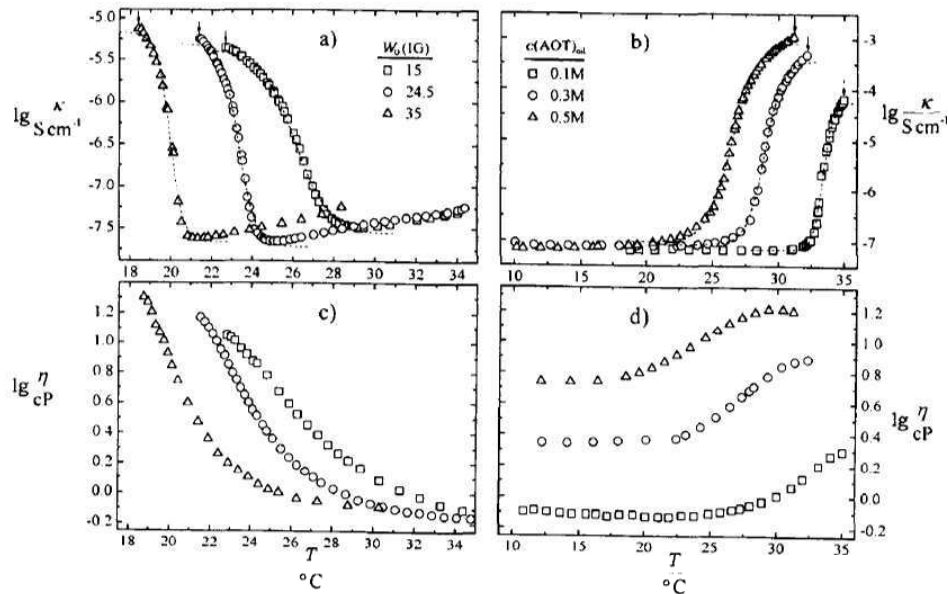


**Fig. 3.3.:** Comparison of temperature induced percolation in the Igepal system for different droplet sizes  $W_0$  (left) and the AOT system for different droplet concentrations  $c(\text{AOT})_{oil}$  (right). The upper row shows the behavior of the electric conductivity  $\kappa$  and the lower row that of the viscosity  $\eta$  [61].

In the non-ionic Igepal system, a strong hydration of the polar molecule groups at lower temperatures occurs, changing the wedge form of the surfactant. This increases the solubility of the surfactant in water. A continuous phase of water is formed due to the increasing effective volume of the head groups of the surfactant, which forces the monolayer into a positive curvature [61].

If the temperature increases, hydrogen bonds break up such that the polar groups are less hydrated. Thus, the curvature of the surfactant monolayer becomes negative. A reverse microemulsion with a continuous oil phase is formed [61].

However, with AOT as surfactant, this temperature behavior is contrary [Fig. 3.3]. With increasing temperature, the electric conductivity and viscosity of the Igepal system decreases, whereas it increases in the AOT system. If one compares the course of electric conductivity and viscosity, it can be seen that the viscosity shows the formation of an infinite network (percolation). However, before such a cluster is formed, structural changes of the system can be observed due to changes in the viscosity [61, 83]. The reason for this behavior lies in the inverse temperature dependence of the surfactants solubility in water [61]. Ionic surfactants are better hydrated, which results in a good solubility, whereas non-ionic surfactants become less soluble.

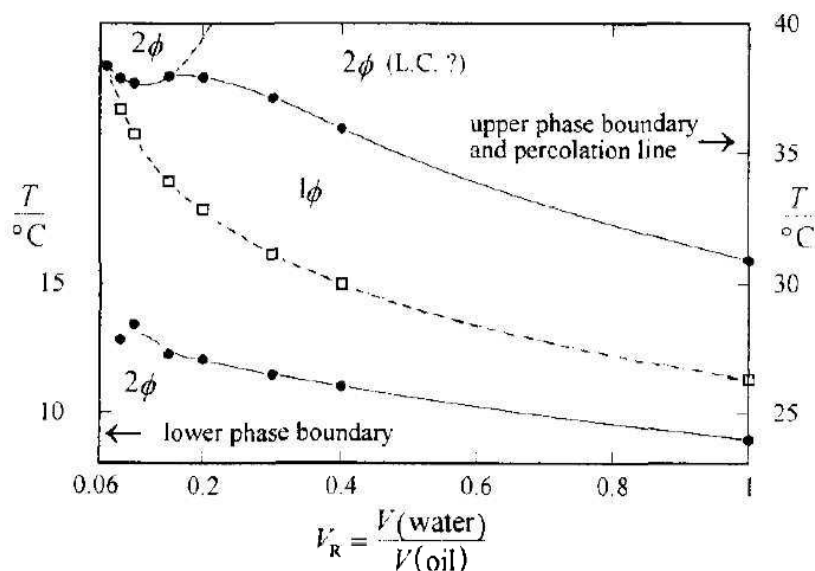


**Fig. 3.4.:** Temperature dependent phase boundaries (black circles) of the AOT microemulsion system for different water to oil ratios  $V_R$ . The percolation curve (open squares) lies between the phases. The volume fraction  $\Phi_{H_2O,AOT}$  between water and AOT is given by  $\Phi_{H_2O,AOT} = 1.39/(1.39 + V_R^{-1})$ . The upper and lower phase boundaries are labeled in the figure [61].

The point of percolation depends on the droplet concentration if the radius of the droplets is constant. If the droplet concentration increases, the percolation point is shifted away from the phase separation temperature, which is the upper phase boundary of the AOT system and the lower one in the Igepal system (compare Fig. 3.4) [61].

The AOT microemulsion is known to remain in the  $L_2$  phase for a broad range of parameter changes, always preserving the spherical form of the water droplets [84]. If the temperature of such a reverse microemulsion is increased, percolation occurs, even if the droplet fraction

constantly remains below the initial percolation transition.

In pattern forming microemulsions, a much larger variance of patterns can be found compared to the standard BZ-AOT system, when a temperature gradient is applied. Due to the shift of the percolation threshold, patterns that occur above and below the percolation threshold can be observed in a single system [86, 87].

In the  $\text{Ru}(\text{bpy})_3^{2+}$ -catalyzed BZ-AOT system, transitions between different type of patterns can be observed, when a temperature gradient is applied. This transition starts with Turing patterns and ends up with reduction waves [86]. The transition between these patterns can be explained by the temperature dependence of the electric conductivity and hence, the diffusion coefficients of activator and inhibitor change [84, 86].

### 3.4.2. Electric Fields

The effect of temperature and electric field gradients on microemulsions is very similar, since electric conductivity is temperature dependent and increases in the AOT system with increasing temperature [84, 86].

When applying weak electric fields to an anionic microemulsion, negligible effects can be observed. The head groups of the AOT molecules can dissociate into  $\text{SO}_3^-$  and  $\text{Na}^+$ . Under the influence of the electric field, the charges can concentrate at the inner surface of a micelle, leading to a polarization of the latter. This affects the electric conductivity [84]. However, rising the electric field strength in a water-in-oil microemulsion with AOT leads to a transition from elongated droplets towards a slow formation of a percolating cluster, which involves many droplets. This shows, that the percolation curve can be shifted [61, 84, 85, 88].

However, if the electric field is turned off, this cluster decays rapidly [83]. Due to the presence of different charge carriers, the formation of percolation clusters is promoted by the polarization and deformation of water droplets [89]. This effect is called Kerr effect [83]. The deformation (elongation) of droplets increases the conductivity of the microemulsion. Furthermore, the polarization of the droplets is supported by  $\text{Na}^+$  ion migration in the ionic surfactant system [89]. Nevertheless, a critical field strength is necessary to induce percolation, since the polarized water droplets start forming channels above a critical field strength. The process of this formation is depicted in Fig. 3.5. The critical electric field strength lies in the order of  $\text{kV cm}^{-1}$ , which induces a phase separation and thus, percolation [59, 89].

The value of the critical electric field depends on the properties of the interface between water and oil, i. e., the distance of the phase boundaries [85].

When measuring the electric conductivity, to determine the percolation threshold, three regimes

can be found, characterized by the magnitude of the conductivity [85, 89]:

1. Immediately after the application of the electric field, a small current occurs, which is induced by Ohmic resistance of the conductivity cell. However, this current is negligible.
2. A higher magnitude of the current yields an additional current, which reaches a stationary value after a certain time. This can be interpreted as elongation of water droplets with respect to the electric field lines.
3. Above the critical field strength, a very high conductivity can be measured. A field-dependent time evolution is found.

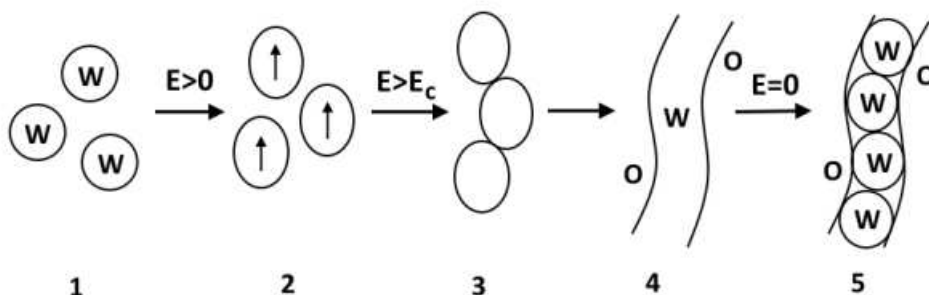


**Fig. 3.5.:** Sketch of electric field-induced percolation in a reverse microemulsion. 1 - Water droplets (W) diffuse freely in an oil phase (O). 2 - After the application of a weak electric field  $E$ , the droplets become polarized. 3 - When the strength of the electric field becomes larger than a critical value  $E_c$ , the polarized droplets form chains. 4 - Within these droplet chains, the surfactant monolayer opens up and water channels are formed. 5 - When the electric field is turned off, the water channels return rapidly to droplet configuration.

However, not in all experiments with a reverse microemulsion under an electric field, a critical field strength can be found. Depending on molar ratio between water and AOT  $\omega$ , the current increases further (regime 2), such that no regime 3 can be found [85].

As far as it is known, the electric field affects the exchange of charge carriers within the droplet clusters and the aggregation of droplets, which is even affected by percolation. Why the AOT system reacts on electric fields in the way it does, cannot be fully explained [85]. The conductivity of the microemulsion increases when an electric field is applied. The increase lies in the same range, as induced by percolation (without electric field), which gives a hint at formation of clusters. Thus, it is assumed, that the electric field does not affect single droplets, but extended clusters [85].

In the past, experiments with electric fields in combination with BZ-AOT microemulsions were only performed below the percolation threshold. In these experiments, the microemulsion was sandwiched between two glass plates with a height of 100  $\mu\text{m}$ . Thus, the solution played the role of a dielectric in a parallel-plate condensator. Two platinum electrodes are used as the



condensator and also played the role of a spacer. A maximum field strength of  $E = 10 \text{ V cm}^{-1}$  was used [80].

In these experiments, Turing spots were found to drift along the field lines of the electric field with a constant velocity. In other words, the dynamics of an initially stationary pattern can be changed into a time-dependent behavior [80]. Using different strengths of the electric field (maximum  $10 \text{ V cm}^{-1}$ ), a change of the wavelength of Turing spots could not be observed, which shows that the wavelength is independent of the flow of ions [80, 90].

Furthermore, in experiments of Carballido-Landeira *et al.* [80], a droplet fraction of 0.56 was used and Turing patterns could still be observed. This indicates, that at this droplet fraction the system is not yet percolated.



## **Part III.**

# **Material and Methods**



## 4. Chemical Preparation

### 4.1. Preparation of Stock Solutions

Many different recipes of the BZ-AOT system are used in this work, which requires a pool of stock solutions from the following reactants: malonic acid, sodium bromate, 1,4-cyclohexanedione, ferroin, iron(II)-sulfate, AOT in n-octane or hexane, bathophenanthroline with AOT in n-octane or hexane. Furthermore, solutions of n-octane, hexane and sulfuric acid are needed. The reactive microemulsion is always prepared freshly.

The stock solutions are prepared as follows: The mass  $m$  of a substance is calculated, which yields the desired concentration  $c$  of the stock solution for a certain volume  $V$

$$m = c \left[ \frac{\text{mol}}{\text{l}} \right] M \left[ \frac{\text{g}}{\text{mol}} \right] V [\text{l}], \quad (4.1)$$

where  $M$  is the molar mass of the chemical substance. The results are listed in Table 4.1.

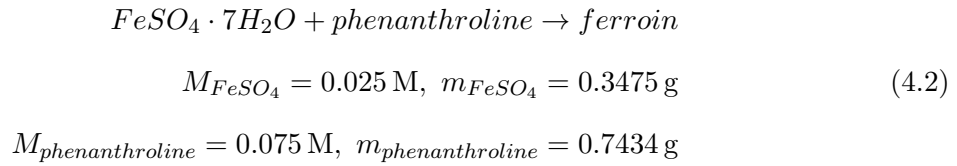
N-octane (*Arcos Organics*) is purified with concentrated sulfuric acid (95 – 97 %; *Merck*). Thus, both solutions are mixed with a ratio of 4 : 1 and stirred for almost a week to remove impurities. Sulfuric acid is not soluble in n-octane, allowing for the removal of n-octane with a pipette before use. Hexane (*Sigma-Aldrich*) is used without purification. The stock solution of AOT is prepared with hexane or purified n-octane.

**Table 4.1.:** Chemical substances with their chemical formula and manufacturer. The mass is calculated for a volume of 50 ml with equation (4.1).

Substance name	Formula	Company	$c$ [mol/l]	$M$ [ $\frac{\text{g}}{\text{mol}}$ ]	$m$ [g]
malonic acid	$\text{CH}_2(\text{COOH})_2$	<i>Merck</i>	2.000	104.60	10.4600
sodium bromate	$\text{NaBrO}_3$	<i>Merck</i>	1.000	150.90	7.5450
1,4-Cyclohexanedione	$\text{C}_6\text{H}_8\text{O}_2$	<i>Merck</i>	1.000	112.13	5.6060
Bathophenanthroline in solvent	$\text{C}_{24}\text{H}_{16}\text{N}_2$	<i>abcr</i>	0.123	332.41	0.2044
Iron(II)-sulfate	$\text{FeSO}_4$	<i>Merck</i>	0.250	278.02	3.4740
AOT in solvent	$\text{C}_{20}\text{H}_{37}\text{NaO}_7\text{S}$	<i>Sigma</i>	1.500	444.56	33.3420

The preparation of ferroin ( $V = 50$  ml) with the concentration of  $c = 25$  mM in 25 mM  $\text{H}_2\text{SO}_4$  is more time-consuming than the preparation of the other BZ stock solutions. The reactants  $\text{FeSO}_4$  and phenanthroline (*R. d. H.*) are mixed in a way, that the ratio of the molar masses of

both substances is 1 : 3:



To this mixture, 2.5 ml of 0.5 M  $H_2SO_4$  is added and filled up to 40 ml with deionized water and stirred for almost 30 min. After stirring, the missing amount of water is added to the solution. The preparation of BP is a little challenging, since it is neither soluble in water nor in pure oil. However, it can be solved in a stock solution of AOT solved in n-octane or hexane [68]. Thus, AOT stock solution is used for the preparation of the stock solution of the so-called batho-AOT. It takes up to three days of stirring until large particles of bathophenanthroline are solved. The stock solution of iron(II)-sulfate must always be prepared freshly, since the iron reacts with the oxygen in the water, such that the iron is oxidized and a yellow-brownish precipitation occurs after a while. For the experiments with BP, a certain amount of the freshly prepared  $FeSO_4$  is added to the microemulsion, such that a molar mass ratio between  $FeSO_4$  and BP of 1 : 3 is reached. The solution of 5 M sulfuric acid (*Fluka*) is commercially available.

## 4.2. Preparation of Microemulsions

For all experiments, two non-reactive microemulsions are prepared, having the same molar ratio  $\omega$  and droplet fraction  $\varphi_d$ . The first microemulsion (ME1) consists of AOT, water, malonic acid (or CHD) and sulfuric acid. Depending on the used catalyst, the second microemulsion (ME2) consists of AOT, water, sodium bromate and ferrioin, or batho-AOT, water, sodium bromate and iron(II)-sulfate. The order of the reactants in ME1 or ME2 corresponds to the mentioned order, starting with AOT. Both microemulsions are stirred until they appear homogeneously. The BZ reaction does not start not until both microemulsions are brought together. They are mixed with a ratio of 1 : 1 and a certain volume of the solvent (n-octane or hexane) is added, depending on the requested droplet fraction  $\varphi_d$ . The value  $\varphi_d$  is chosen below and above the percolation transition with values between 0.35 and 0.7.

The calculation of the volumes of the reactants is realized by the knowledge of the final concentrations in the reactive microemulsion, as well as the value of  $\omega$ :

$$\omega = \frac{[H_2O]}{[AOT]}.
 \tag{4.3}$$

For the calculation of the needed volume of water, the concentration of water in water  $c_{H_2O}$  is required. It can be calculated as follows:

$$\frac{m_{H_2O} \text{ per liter}}{M_{H_2O} \text{ per mol}} = \frac{1000 \text{ [g/l]}}{18.015 \text{ [g/mol]}} \quad (4.4)$$

and results in a value of 55.51 M. Thus, (3.1) can be written as:

$$\omega = \frac{V_{H_2O} c_{H_2O}}{V_{gesAOT} c_{AOT}} \quad (4.5)$$

which yields a volume of water  $V_{H_2O} = 1.947$  ml for both microemulsions, with a volume of AOT  $V_{gesAOT} = 4$  ml and  $c_{AOT} = 1.5$  M.

Given the total volume of the reactive microemulsion, volumes of the reactants can be calculated (concentrations are given). Note, that the total volume is the volume of the water phase, since there is no reaction in the oil phase.

With the equation for the droplet fraction  $\varphi_d$  the volume of oil  $V_{oil}$  of the reactive microemulsion can be calculated ( $V_{H_2O}$  corresponds to the volume of water):

$$\varphi_d = \frac{V_{AOT} + V_{H_2O}}{V_{AOT} + V_{H_2O} + V_{oil}}. \quad (4.6)$$

However, the volume of AOT  $V_{AOT}$  must be calculated first. The used volume of AOT  $V_{gesAOT}$  is chosen to be 4 ml, in order to have enough volume for stirring. Subsequently, the actual volume of AOT  $V_{AOT}$  in the solvent must be calculated, starting with the mass  $m_{AOT}$ :

$$m_{AOT} = c_{AOT} V_{gesAOT} M_{AOT}, \quad (4.7)$$

$$m_{AOT} = 1.5 \text{ [M]} \cdot 0.04 \text{ [l]} \cdot 444.56 \left[ \frac{\text{g}}{\text{mol}} \right], \quad (4.8)$$

$$m_{AOT} = 2.667 \text{ [g]}.$$

With the measured density of AOT  $\rho_{AOT} = 1.15$  g/l the volume of AOT in the solvent can be calculated:

$$V_{AOT} = \frac{m_{AOT}}{\rho_{AOT}}, \quad (4.9)$$

$$V_{AOT} = 2.319 \text{ [ml]} \text{ in } 4 \text{ ml AOT stock solution.}$$

The result of this calculation for experiments under presence of electric fields can be seen in Table 4.2.

## 4.2. PREPARATION OF MICROEMULSIONS

**Table 4.2.:** Recipe for Turing Patterns used for the experiments with the electric field with the following concentrations:  $[MA] = 0.259$  M,  $[NaBrO_3] = 0.155$  M,  $[H_2SO_4] = 0.207$  M and  $[Ferroin] = 1.74$  mM and  $\omega = 18.03$ . For the droplet fraction of 0.48 and 0.52, the ratio between ME1, ME2 and solvent is 1 : 1 : 1, or 1 : 1 : 0.8, respectively.

Microemulsion 1		Microemulsion 2	
reactant	volume [ml]	reactant	volume [ml]
AOT in n-octane (1.5 M)	2.000	AOT in n-octane (1.5 M)	2.000
H <sub>2</sub> O	0.680	H <sub>2</sub> O	0.498
MA (2 M)	0.252	NaBrO <sub>3</sub> (1 M)	0.291
H <sub>2</sub> SO <sub>4</sub> (5 M)	0.080	Ferroin (25 mM)	0.135

For experiments without electric fields (Sect. 7) the used recipes are listed in Tables 4.4 and 4.5.

**Table 4.4.:** Concentrations of the reactants in the ferroin-catalyzed BZ-AOT system in n-octane and hexane for different ratios  $\omega$ .

$\omega$	solvent	MA [M]	H <sub>2</sub> SO <sub>4</sub> [M]	NaBrO <sub>3</sub> [M]	ferroin [mM]	$\varphi_d$
12	octane	0.250	0.175	0.150	4.20	0.455
	hexane	0.300	0.200		4.00	
15	both	0.247	0.197	0.177	4.41	0.468
18	both	0.259	0.207	0.155	4.14	0.480
20	both	0.3	0.200	0.150	4.00	0.485

**Table 4.5.:** Concentrations of the reactants in the BP-catalyzed BZ-AOT system in n-octane and hexane for different  $\omega$ . The recipes are equal for both solvents.

$\omega$	MA [M]	H <sub>2</sub> SO <sub>4</sub> [M]	NaBrO <sub>3</sub> [M]	BP [mM]	$\varphi_d$
12	0.242	0.174	0.194	6.00	0.455
15	0.243	0.175	0.194	4.87	0.360
20	0.242	0.174	0.194	3.80	0.485

In Sect. 8 experiments with CHD as organic substrate are presented. An overview of the concentrations is given in Tabs. 4.6 and 4.7. A complete list of the used concentrations is given



in Table C.4.

**Table 4.6.:** Concentrations of the reactants in the ferroin-catalyzed BZ-AOT system with CHD ( $\omega = 18$ ).

recipe	CHD [M]	H <sub>2</sub> SO <sub>4</sub> [M]	NaBrO <sub>3</sub> [M]	ferroin [mM]	$\varphi_d$	$\varepsilon$
I	0.23	0.20	0.120	2.50	0.59	0.104
II	0.23	0.20	0.170	2.50	0.40	0.148
III	0.20	0.35	0.155	2.05	0.59	0.271

**Table 4.7.:** Concentrations of the reactants in the BP-catalyzed BZ-AOT system with CHD ( $\omega = 18$ ).

recipe	CHD [M]	H <sub>2</sub> SO <sub>4</sub> [M]	NaBrO <sub>3</sub> [M]	BP [mM]	$\varphi_d$	$\varepsilon$
1	0.25	0.20	0.12	5.0	0.40	0.096
2	0.12	0.16	0.15	4.1	0.40	0.200
3	0.30	0.20	0.23	5.0	0.59	0.261



# 5. Experimental Methods

## 5.1. Measurement of Physical Properties

The electric conductivity is measured with the conductivity meter YSI model 3200 with the electrode 3254. The device produces an alternating electric field of 1000 Hz to avoid polarization of nanodroplets in the microemulsion. Starting with an initial droplet fraction  $\varphi_d$  between 0.68 and 0.74 of the reactive microemulsion, the solvent is added gradually until reaching a conductivity below  $1 \mu\text{S cm}^{-1}$ .

The radius of the water droplets is measured using dynamic light scattering (Wyatt DynaPro Nano Star). A small amount of the reactive microemulsion ( $\sim 15 \mu\text{l}$ ) is put into a glass cuvette, which is insert into the device. Afterwards, a few minutes of waiting are required for the microemulsion to stabilize. After that, the laser (wavelength 662.18 nm) can be turned on. When intensity fluctuations fall below 20% the measurement is started.

The viscosity of the microemulsions is measured using a micro-Ubbelohde viscometer (Schott, type 50113, Ic micro) [Fig. 5.1]. This viscometer has a constant  $K = 0.03 \text{ mm}^2 \text{ s}^{-2}$  and a diameter of 0.42 mm, which yields a measuring range of the kinematic viscosity between  $1.2$  and  $18 \text{ mm}^2 \text{ s}^{-1}$ .

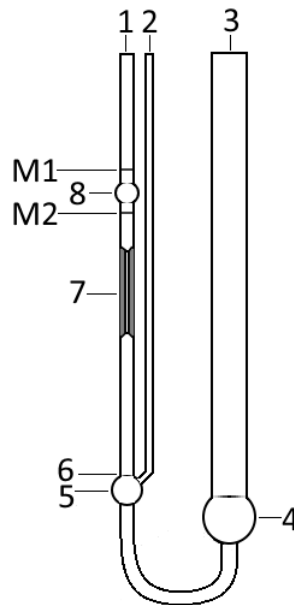


**Fig. 5.1.:** Schematic view of a micro-Ubbelohde viscometer (Schott). 1 - capillary tube, 2 - venting tube, 3 - filling tube, 4 - reservoir, 5 - reference level vessel, 6 - dome-shaped top part, 7 - capillary, 8 - measuring sphere, M1 - upper timing mark and M2 - lower timing mark.

The measurement is done as follows: The liquid is filled into the reservoir (4) and a pipe is attached at the capillary tube (1). The venting tube (2) is closed with a finger. Using the pipe, the liquid is drawn through the reference level vessel (5), the capillary (7) and the measuring sphere (8), until the liquid is almost 10 mm above M1. The pipe is removed and the venting tube is opened. A stop watch is used to measure the time the liquid needs to pass M2 (starting at M1). The measurement is repeated five times and the mean value of the flow time is calculated. This value is multiplied with the cell constant to get the kinematic viscosity  $\nu$  [ $\text{mm}^2\text{s}^{-1}$ ]. The dynamic viscosity  $\eta$  is calculated using the density of the liquid  $\rho$ :

$$\eta[\text{Pa s}] = \rho[\text{g cm}^{-3}] \nu[\text{mm}^2 \text{s}^{-1}]. \quad (5.1)$$

The density is measured with a pycnometer (Schott) with a volume of  $24.823 \text{ cm}^3$ . It is filled with the liquid and the mass of the liquid is measured.

The temperature in the laboratory remained constant at  $(21 \pm 1)^\circ\text{C}$ .

## 5.2. Experimental Setup without Electric Fields

To observe the patterns forming in the reactive microemulsion, a small amount of the latter is given into the reactor [Fig. 5.2].

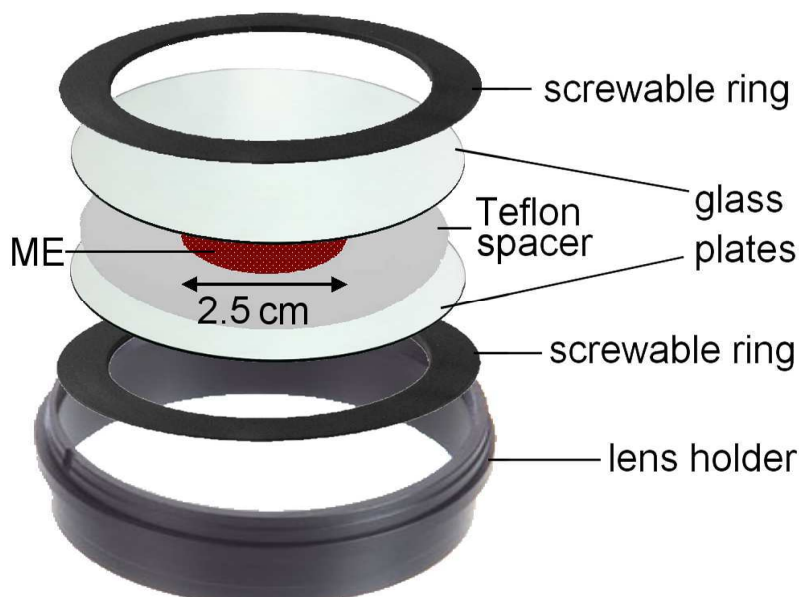


**Fig. 5.2.:** Reaction container for the experiments without electric fields. The microemulsion is sandwiched between two glass plates. The inner diameter of the Teflon spacer is 2.5 cm and its thickness is  $80 \mu\text{m}$ .

It consists of two glass plates and a Teflon spacer (thickness  $80 \mu\text{m}$ ). The microemulsion is

sandwiched between the glass plates, such that no air bubbles remain. The plates are wrapped with Teflon tape, put into the lens holder and screwed with the rings.

The reactor is inserted into in the experimental setup [Fig. 5.3]. The illumination is realized by a self-made LED panel with 100 white LEDs (maximum intensity around 455 nm) through an interference filter (480 nm, bandwidth 10 nm). This wavelength is used, since the absorption spectrum of ferroin and ferriin has a maximum distance around 480 nm, which yields a good contrast.

The observation of the patterns is ensured through a stereo microscope (Zeiss GSZ 2T), with a CCD camera (AVT Stingray F-046B), which is connected to a computer. The frame rate is 0.495 Hz, if no other frame rate is mentioned.

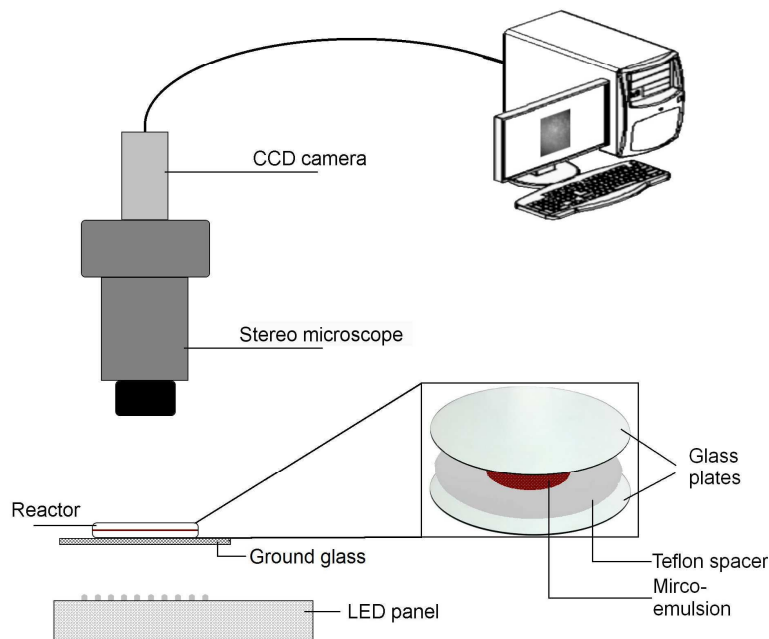


**Fig. 5.3.:** Sketch of the experimental setup, which is used for monitoring the patterns in the microemulsion. The reactor is illuminated by a LED panel through an interference filter (480 nm, bandwidth 10 nm). The ground glass is used to create homogeneous illumination. The images of the patterns are recorded with a CCD camera through a stereo microscope.

### 5.3. Experimental Setup with Electric Fields

The optical setup for experiments with electric fields is equal to the one presented in Sect. 5.2. However, the reactor is different, since the reactor in Sect. 5.2 is not suitable for experiments with electric fields. It is necessary to put some electrodes into the reactor.

Platinum/iridium (90/10 wt%) electrodes (*Alfa Aesar*) with a thickness of 220  $\mu\text{m}$  and 100  $\mu\text{m}$  (length 2.5 cm) are used. They are immersed directly into the microemulsion, additionally taking the role of a spacer [Fig. 5.4]. As they are made of precious metal, the electrodes do not interfere with the microemulsion. No electrolysis can be observed on the electrodes.

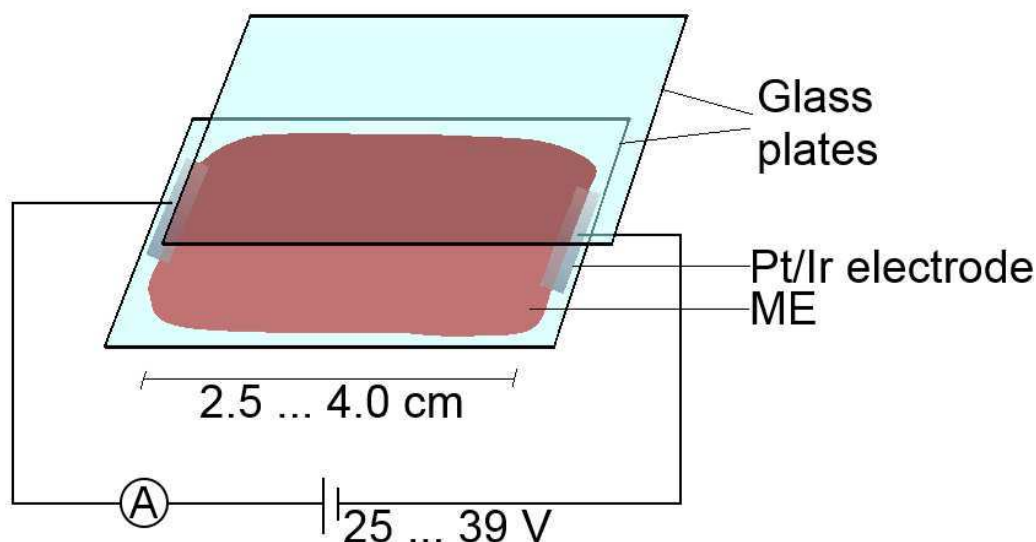


**Fig. 5.4.:** Reaction container for the experiments with electric fields. The microemulsion is sandwiched between two Plexiglas plates. The platinum/iridium electrodes play the role of a spacer and are connected to a voltage source. The electric current is measured with an ammeter. The distance between the electrodes is variable.

The distance between the electrodes can be varied between 2.5 and 4 cm in 0.5 cm steps. This is realized by differently sized cover plates. Measurements using direct current (DC) are performed in the following way: Electrodes are connected to a voltage source (Voltcraft DIGI 40) and an ammeter (Präcitronic MV 40). When the patterns are fully developed, the electric field is switched on. Simultaneously, the current is measured with the ammeter.

For alternating current (AC), a waveform generator (PeakTech 4045) is used as the voltage source. With this generator, different wave forms can be applied, such as sine, pulses and square waves. The frequency of the pulses is varied between 0.001 and 10 Hz. The voltage oscillates within the interval of -10 and 10 V (peak-to-peak).

## 5.4. Analysis of Image Data

The recorded image data are preprocessed using several different image processing techniques, written in IDL (Interactive Data Language, ITT Visual Information Solutions).

First, a contrast enhancement is applied to improve the quality of the images [Fig. 5.5]. For

this purpose, the maximum and minimum gray value from all images of an experiment are determined. Based on this information, the gray values are linearly rescaled, such that they vary between 0 and 255. Subsequently, the background is calculated as the mean of all images and subtracted from each individual image. Afterwards, the contrast enhancement routine is repeated and the contrast improved images are saved [Fig. 5.5(b)].

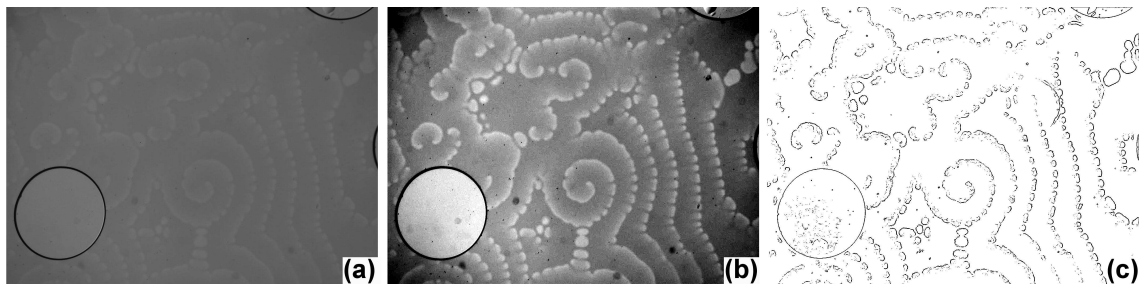


**Fig. 5.5.:** Snapshot of an experiment, to show the steps of image processing: (a) original data, (b) contrast enhanced image and (c) binarized image. The circle is a gas bubble, which develops during the experiment. Image size:  $8.1 \times 6.1 \text{ mm}^2$ .

For experiments with BP, binarized images, showing just the wave fronts represented by thin lines, are calculated [Fig. 5.5(c)]. The contrast improved images are low-pass filtered (in Fourier domain) to reduce noise, followed by a gray value spreading. In the resulting images, the darkest gray values are clipped, such that only pixel values above a certain threshold remain (this threshold must be chosen individually for each experiment). Again, the gray values are spread to the whole interval between 0 and 255. Now, wave fronts are segmented using an edge detection algorithm. This is possible since gray values of neighboring pixels have much higher differences in front of a wave, than at its tail. This procedure is followed by another gray value spreading, in order to improve visibility for the subsequent manual clipping of the darkest pixel values. After that, gray values are rescaled to the full interval again. Now, the function MORPH\_GRADIENT is applied. It subtracts an eroded version of a gray scale image from a dilated version of the image, to highlight edges [91]. Finally, the image is binarized (threshold defined manually). This procedure is done for all images of a measurement. An exemplary result is shown in Fig. 5.5(c).

Using the presented image processing routine, snapshots covering almost ten minutes of a measurement can be illustrated within a single image. For this purpose, binarized images are calculated every 30 to 50 seconds and super-positioned into a combined result [Fig. 5.6]. If the time interval is chosen too short, the waves have not propagated far enough [Fig. 5.6(a)]. When the time interval is too long, no information can be recognized. Thus, it is important to take the right length of the interval as well as the right time lag between the single images [Fig. 5.6(b)].

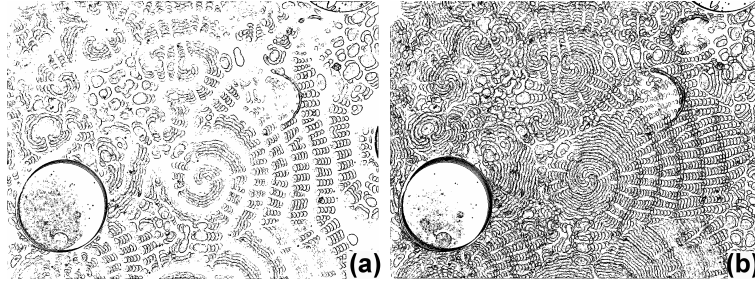


**Fig. 5.6.:** Superposition of binarized images from an image series of a measurement (a) showing 3.9 min of the measurement and (b) 7.9 min of the measurement. The time lag between the superpositioned images is 50 s. Note, that the black lines in the binarized images and superpositions represent the oxidized state of the reaction. The large circle corresponds to a gas bubble. Image size:  $8.1 \times 6.1 \text{ mm}^2$

The contrast enhanced images are used to compute a horizontal and a vertical time-space plot. In the case of experiments with electric fields, the time-space plot is used to calculate the drift velocity  $v$  of the patterns [Fig. 5.7]:  $v = \Delta x / \Delta t$ . The values of  $\Delta x$  and  $\Delta t$  are estimated manually from the images and must be multiplied with the corresponding resolution.

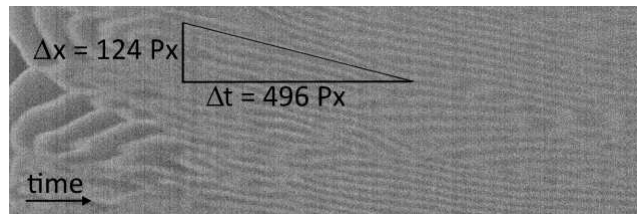


**Fig. 5.7.:** Image section of a time-space plot to visualize the estimation of the drift velocity  $v$  of the patterns. The space resolution is 1 pixel = 0.66 mm and the time resolution 1 pixel = 2 s.

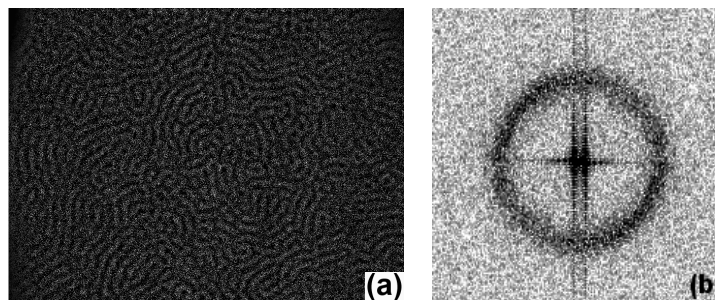


**Fig. 5.8.:** (a) Turing pattern with (b) the corresponding amplitude spectrum. Image size:  $5.2 \times 3.8 \text{ mm}^2$ . The inverse wavelength is determined, measuring the distance between point of origin and the circle around this point (which gives the frequency).

When Turing patterns are observed, a spatial Fourier transform from an original image is done, yielding an amplitude spectrum, from which the characteristic wavelength of the patterns can be determined [Fig. 5.8]. If a dominant wavelength is present in the original image, the amplitude spectrum is expected to contain a distinct maximum at the corresponding spacial frequency. In case of random orientation of the waves, this maximum will form a circle in the spectrum.



Therefore, the inverse wavelength of the pattern can be determined as the distance of this circle from the origin.

The curvature of a wave front is determined with an ImageJ plugin, called ThreePointCircularROI. With this plugin, three spots on a wave front are marked manually. To ensure highest accuracy, they should lie far away from each other. From these three spots, the corresponding circle is calculated which should fit the wave front [Fig. 5.9]. The radius of this circle is the inverse curvature of the circle and thus, of the wave front.

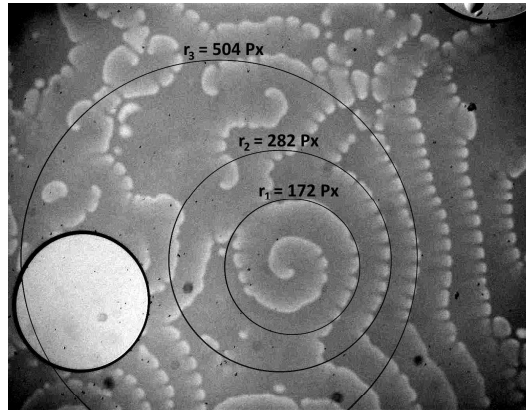


**Fig. 5.9.:** Determination of wave front curvature. Three spots of a wave front are marked, which should lie as far as possible away from each other to reduce errors to a minimum. From these spots, the corresponding circle is calculated and the curvature of the circle can be estimated. Image size:  $8.1 \times 6.1 \text{ mm}^2$ .



**Part IV.**

**Results**



## 6. Physical Properties

In this chapter, some important physical properties of the pattern forming microemulsion are investigated, such as electric conductivity (Sect. 6.1) and droplet radius (Sect. 6.2) as well as density and viscosity (Sect. 6.3). These properties are important to characterize the microemulsion and to understand pattern formation, governed by the percolation process.

### 6.1. Electrical Conductivity

Electric conductivity provides information on the onset of percolation in the system. For a large amount of oil (i. e.,  $V_{oil} \gg V_{water}$ ), the conductivity lies above the typical value of an apolar solvent, i. e.,  $0.02 \mu\text{S cm}^{-1}$  for  $\varphi_d = 0.25$  [64]. This value is non-zero, since nanodroplets in pure water-in-oil microemulsions can carry positive or negative excess charges generating a higher conductivity due to diffusion of droplets [65]. In microemulsions loaded with the BZ reaction, the electric conductivity is again higher than in pure ones without BZ reaction (around  $0.5 \mu\text{S cm}^{-1}$  for  $\varphi_d = 0.23$  [66]).

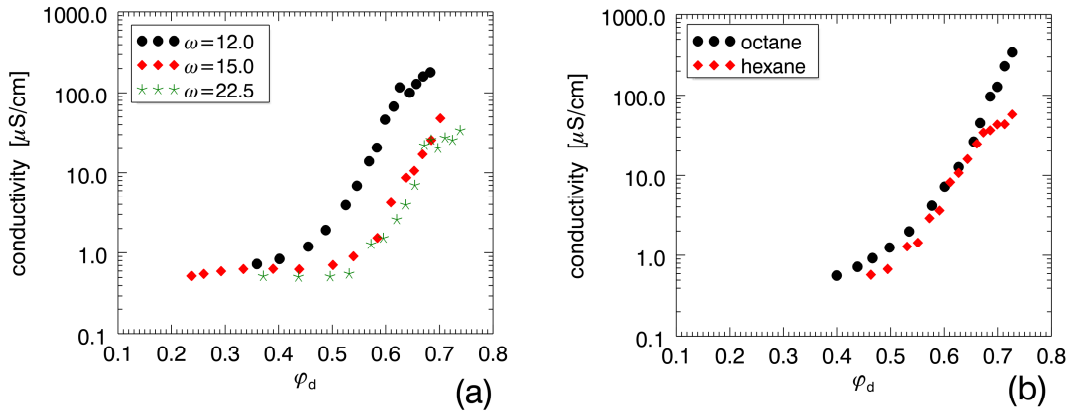


**Fig. 6.1.:** (a) Conductivity of the BZ-AOT microemulsion dissolved in hexane as a function  $\varphi_d$  and (b) comparison of the conductivity for n-octane and hexane at  $\omega = 20$ . For recipes see Table 4.4 [66].

The conductivity for pure water-in-oil microemulsions can be calculated using equation (3.4). In most of the studied patterns, a droplet fraction of 0.48 is used. This yields a droplet radius  $R_w = (2.4 \pm 0.2)$  nm. The dynamic viscosity of the microemulsion for  $\varphi_d = 0.48$  is  $(9.234 \pm 0.028)$  mPas and for  $\varphi_d = 0.52$  it is  $(13.39 \pm 0.03)$  mPas (see Sect. 6.3). The calculation of  $\sigma$  with

(3.4) yields  $(0.038 \pm 0.002) \mu\text{S cm}^{-1}$ . The conductivity above the percolation threshold cannot be calculated (in that manner). For  $\varphi_d = 0.52$  the droplet radius increases due to cluster formation and lies in the range between 20 and 100 nm. Thus, a definition of the droplet radius is not possible.

In Fig. 6.1 a typical plot of a conductivity measurement is shown for different recipes (a) and solvents (b). The initial value of  $\varphi_d$  depends on  $\omega$ , since both values are not completely independent of each other. They are connected by the volume of AOT. Equation (3.1) requires the concentration of AOT and equation (4.6) the volume of AOT (without solvent). However, if the amount of oil increases,  $\varphi_d$  changes, while  $\omega$  remains the same.

The conductivity remains below  $1 \mu\text{S cm}^{-1}$  for  $\varphi_d = 0.4 - 0.5$  and  $\omega = 15 - 22$ , whereas for  $\omega = 12$  the conductivity is significantly increased. The same holds true for BP as the catalyst.

## 6.2. Droplet Radius

In this section, results of droplet radius measurements are presented. Note, that the values of the droplet radius refer to the inner radius (without the AOT molecule). To get the entire radius of the droplet, the length of the AOT-molecule must be added, which is 1.1 nm [44, 63]. In all cases, two different droplet radii are found, one in the order of 1 nm and the other, one order of magnitude larger (compare Fig. 11).

The radius of the water core of the droplets  $R_w$  can be estimated as follows:  $R_w = 0.17 \omega$  [44]. However, this estimation works only for radii in the order of 1 nm. The second peak correspond to droplet clusters. The amount of these clusters increase with increasing  $\varphi_d$ .

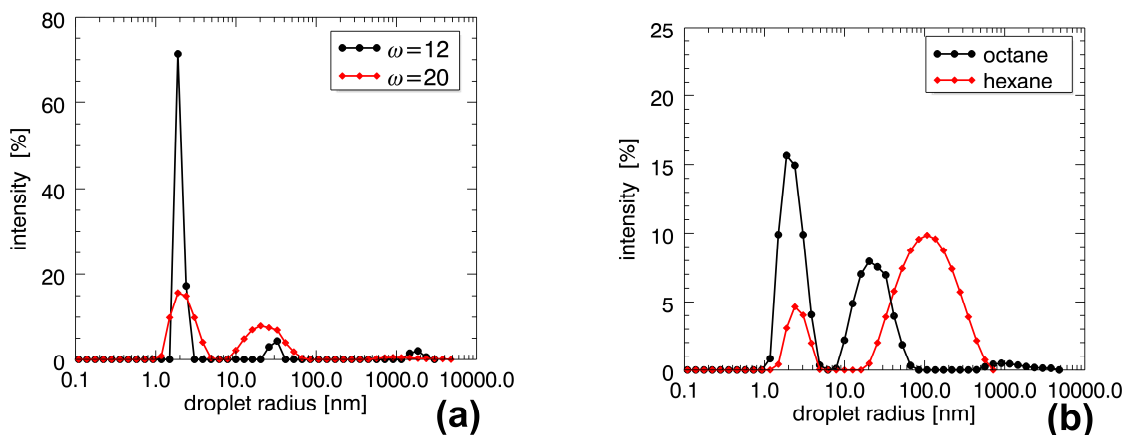


**Fig. 6.2.:** (a) Droplet radius in the ferroin-catalyzed microemulsion with n-octane for  $\omega = 12$ ,  $\varphi_d = 0.455$  and  $\omega = 20$ ,  $\varphi_d = 0.349$ . (b) Comparison of the droplet radius for n-octane ( $\varphi_d = 0.349$ ) and hexane at  $\omega = 20$  and  $\varphi_d = 0.727$ . Note, that the experiment with hexane has a value of  $\varphi_d$  above the percolation threshold. Thus, the second peak for hexane consists of droplet clusters. For recipes see Table 4.4.

An overview of measured and estimated droplet radii is given in Table 6.1 for different  $\omega$  and both solvents and catalysts used in this work.

In Fig. 6.2(a) the droplet radii for two different  $\omega$  with n-octane as solvent are shown. The droplet radius lies at 2.00 nm for  $\omega = 12$  and at 2.65 nm for  $\omega = 20$ . If the droplet radius is estimated with equation (3.3), the droplet radius for  $\omega = 12$  should be 2.04 nm and 3.40 nm for  $\omega = 20$  (compare Table 6.1).

Figure 6.2(b) shows the droplet radius in n-octane and hexane with  $\omega = 20$ . The peak of the radius lies at 2.65 nm for both solvents. However,  $\varphi_d$  differs significantly for both solvents.

The second peak for hexane ( $\varphi_d = 0.727$ ) is much larger than for n-octane ( $\varphi_d = 0.349$ ). Thus, it can clearly be observed, that the system with hexane is more percolated due to the higher droplet fraction, than the system with octane.

**Table 6.1.:** Measured and estimated droplet radii according to equation (3.3) with ferroin and BP in n-octane and hexane for different  $\omega$ .

catalyst	$\omega$	solvent	$R_w$ [nm] (measured)	$R_w$ [nm] (estimated)
ferroin	12	n-octane	2.00	2.04
		hexane	2.18	
	15	n-octane	2.39	2.55
		hexane	2.18	
	18	n-octane	2.00	3.06
		hexane	1.17	
20	n-octane	2.65	3.40	
	hexane	2.65		
BP	12	n-octane	2.15	2.04
		hexane	1.00	
	15	n-octane	2.39	2.55
		hexane	1.10	
	18	hexane	1.17	3.06
		n-octane	2.39	
	20	n-octane	2.39	3.40
		hexane	1.17	

In Fig. 6.3(a) the droplet radii of the BP-catalyzed microemulsion with n-octane and hexane are depicted. The radius of the droplets with hexane is a little smaller than in octane (for values see Table 6.1). In all measurements, the radius of the droplets in hexane is found to be smaller or equal to that in octane. Fig. 6.3(b) shows the droplet radii for ferroin and BP in n-octane.

The radius of the droplets with BP is slightly larger than that of the ferroin droplets. Especially the second peak lies at significantly larger radii.

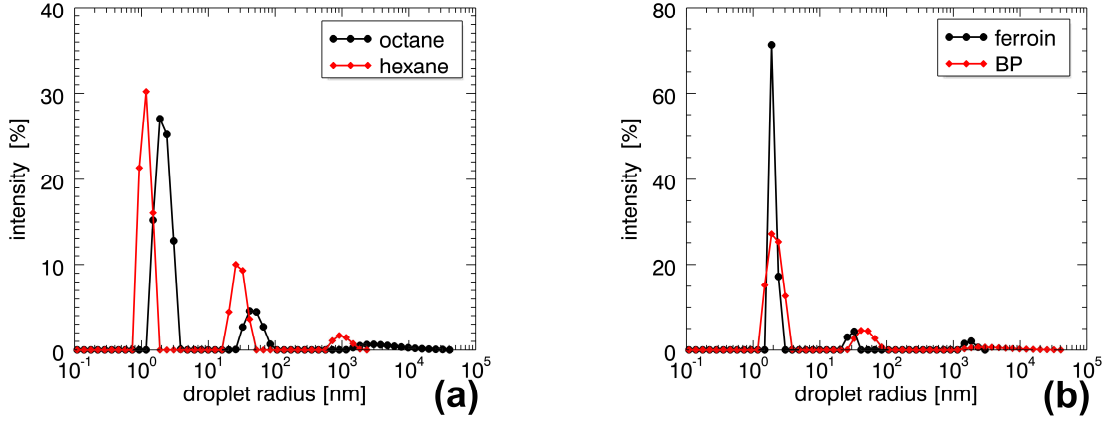


**Fig. 6.3.:** (a) Comparison of the droplet radius with BP in n-octane ( $\omega = 12$ ,  $\varphi_d = 0.455$ ) and hexane ( $\omega = 18$ ,  $\varphi_d = 0.478$ ) and (b) comparison of the droplet radius with ferroin and BP in n-octane (both  $\omega = 12$ ,  $\varphi_d = 0.455$ ). For recipes see Table 4.5.

### 6.3. Density and Viscosity

The density  $\rho$  and the kinematic viscosity  $\nu$  of the BZ-AOT system are measured for the following recipe:  $[\text{MA}] = 0.259 \text{ M}$ ,  $[\text{NaBrO}_3] = 0.155 \text{ M}$ ,  $[\text{H}_2\text{SO}_4] = 0.207 \text{ M}$  and  $[\text{ferroin}] = 1.74 \text{ mM}$ ,  $\omega = 18.03$ . The droplet fraction  $\varphi_d$  varies between 0.31 and 0.52.

Using the density, the dynamic viscosity  $\eta$  of the microemulsion can be calculated:  $\eta = \rho \nu$  (Table 6.2).

**Table 6.2.:** Measured density, kinematic viscosity  $\nu$  and dynamic viscosity  $\eta$  of a microemulsion with different droplet fractions  $\varphi_d$ .

$\varphi_d$	$\rho$ [ $\text{g cm}^{-3}$ ]	$\nu$ [ $\text{mm}^2 \text{s}^{-1}$ ]	$\eta$ [ $\text{mPa s}$ ]
0.31	0.84	5.66	$4.76 \pm 0.03$
0.48	0.79	11.67	$9.23 \pm 0.03$
0.52	0.90	14.86	$13.39 \pm 0.03$

With the values of the dynamic viscosity, the diffusion coefficient of the activator in the system can be estimated using the Stokes-Einstein equation (3.5). With  $\varphi_d = 0.48$  the diffusion coefficient of the activator is  $9.75 \times 10^{-8} \text{ cm}^2 \text{s}^{-1}$  and with  $\varphi_d = 0.31$  it is found to be  $2.26 \times 10^{-7} \text{ cm}^2 \text{s}^{-1}$ .



## 6.4. Discussion

In this chapter, physical properties of the used microemulsions are studied. The electric conductivity (Sect. 6.1) provides information on the percolation process of the system. Comparing the conductivity and the observed patterns in the system, the progress of percolation can be estimated, i. e., if the system only contains droplets or if droplet clusters are already present. Especially in the case of Turing patterns, this comparison is important, since these patterns can only be observed below the percolation transition, when the activator is trapped in the droplets [16].

Percolation takes place around  $\varphi_d \approx 0.5$  [68]. The conductivity starts to increase around  $\varphi_d = 0.4$ . However, it is still below  $1 \mu\text{S cm}^{-1}$  at  $\varphi_d = 0.5$  [Fig. 6.1]. Note, that percolation does not occur at a fixed value but is a continuous process starting with local cluster formation until these clusters are distributed over the whole medium. The threshold may vary with the used recipes, but in most cases the conductivity at  $\varphi_d = 0.5$  is below  $1 \mu\text{S cm}^{-1}$  [66].

The terms "above" and "below" the percolation threshold just provide a rough estimation of the system's state. Saying "below the percolation threshold" means that cluster formation might just have started, whereas it is probably not fully completed "above the threshold". Thus, in terms of  $\varphi_d$  the threshold must be estimated for each used recipe.

Moreover, the percolation threshold can be changed applying a temperature gradient or an electric field [84, 85].

The droplet radius also gives information on the percolation process. Basically, a bimodal distribution of the droplet radius can be found [69, 78]. When droplet clusters are present in the microemulsion, the measured amount of droplets with a droplet radius around 10 nm increases [Fig. 6.3(b)].

Also the droplet radius in experiments with BP should be larger than in experiments with ferroin for the unclustered droplets (first peak in Fig. 6.3(b)). BP is more hydrophobic and located mostly in the AOT shell [66]. A slightly larger radius can be found in the measurements, however, not very prominent (compare Fig. 6.3(b)).

Certainly, the results of the dynamic light scattering measurements would have higher accuracy without using a catalyst, since the catalyst changes the absorption properties of the sample. However, differences in the droplet radius caused by the corresponding catalysts cannot be observed this way.

The use of the catalysts, which influence the measured droplet radius, may be the reason for the sharp peaks in the intensity that are observed in most experiments. Thus, the values around 1

nm are expected to have large errors.

An effect of the two different oils on the droplet radius was not found. When the system has a higher droplet fraction, more droplets have a radius around 10 nm and the amount of 1 nm sized droplets is getting smaller. This also provides information about the percolation of the system and hence, the observable patterns. Using the value of the droplet radius as well as the dynamic viscosity of the microemulsion (as measured in Sect. 7.3), the diffusion coefficient of the activator can be estimated to  $9.75 \times 10^{-8} \text{ cm}^2 \text{ s}^{-1}$  for  $\varphi_d = 0.48$  ( $2.26 \times 10^{-7} \text{ cm}^2 \text{ s}^{-1}$  with  $\varphi_d = 0.31$ ). These values perfectly agree with the values mentioned in Ref. [92].

# 7. Patterns in the BZ-AOT System with Malonic Acid

## 7.1. Ferroin-Catalyzed BZ Reaction

In this section, the BZ-AOT system, with malonic acid as the organic substrate and ferroin as the catalyst, is studied, using different recipes and two different solvents: n-octane and hexane. With this experimental constellation, labyrinth-like Turing patterns can be observed. Droplet fractions between 0.36 and 0.58 are used, such that some experiments are performed very close to the percolation transition as well as below the transition.

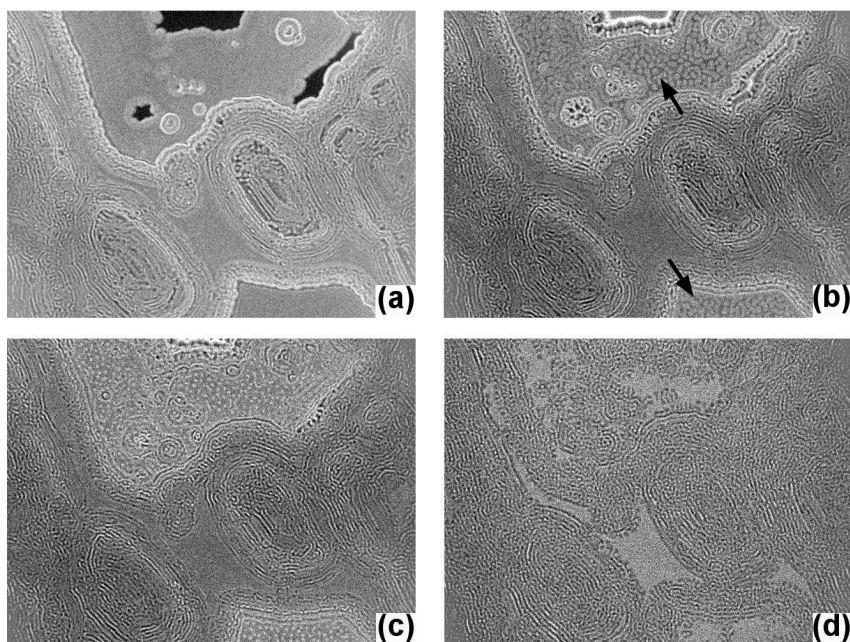


**Fig. 7.1.:** Snapshots of developing Turing patterns close to the percolation transition (a) at 11.3 min, (b) at 13.0 min, (c) at 15.5 min and (d) at 28.9 min. (b) At the upper and lower image border (arrows), some spots emerge, that look similar to those in the BP-catalyzed system. (c) These structures develop into Turing spots. Recipe: n-octane, [MA] = 0.3 M, [NaBrO<sub>3</sub>] = 0.2 M, [H<sub>2</sub>SO<sub>4</sub>] = 0.2 M, [ferroin] = 1.97 mM,  $\omega = 14$  and  $\varphi_d = 0.58$ . Image size:  $11.9 \times 8.9 \text{ mm}^2$ .

The characteristic Turing wavelength  $\lambda$  and the dynamic behavior of the observed Turing patterns are almost equal in a series of experiments with identical initial conditions. However, the particular shape of patterns can be different. In this chapter,  $\omega$  is changed from 12 to 20 for both solvents and the concentrations of the reactants are varied slightly (see Table 4.4). The wavelength  $\lambda$  lies around 200  $\mu\text{m}$  with octane and hexane, decreasing with increasing  $\omega$ . Also the period of the bulk oscillations is almost equal for octane and hexane. However, it varies

strongly for different  $\omega$  and lies in the range between 102 and  $(284 \pm 2)$  s.

With a droplet fraction of  $\varphi_d = 0.58$ , Turing patterns can still be observed. However, in these experiments, some regimes in the reaction container show different structures [Fig. 7.1]. Bubble like structures emerge [Fig. 7.1(b)], which look similar to those in the BP-catalyzed system (see Sect. 7.2). Later, they develop into Turing spots, such that they co-exist with labyrinth-like Turing patterns (c). With time, the spots disappear and the labyrinth patterns occupy the entire reactor (d).

The interaction between the emerging structures and bulk oscillations is studied in detail, since the bulk oscillations are observed to affect the emergence of the structures. Thus, the development of labyrinth-like Turing structures looks different in n-octane and hexane, but the resulting pattern is the same [Fig. 7.2].

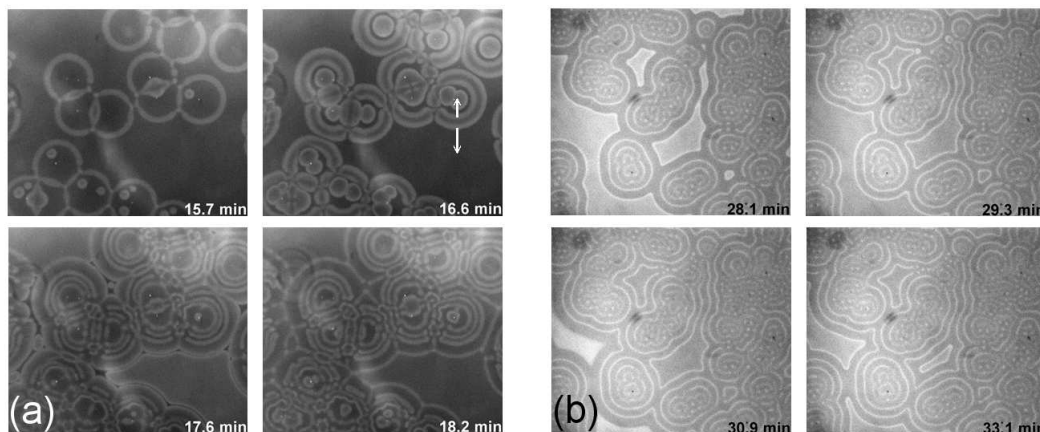


**Fig. 7.2.:** Snapshots of Turing patterns interacting with bulk oscillations ( $\omega = 18.03$ ,  $\varphi_d = 0.48$ ) at different time instants (a) in n-octane (b) and in hexane. In n-octane (a), the outer wave front merges with the bulk oscillation. The former splits up into two waves which propagate into opposite directions (arrows). The front, propagating into the direction of existing patterns forms the labyrinth structure. The outer wave merges with the next oscillation. Using hexane (b), the bulk oscillation stops before reaching the existing pattern and forms a new ring around. With time, this ring breaks into segments forming the labyrinth-like patterns. For recipes see Table 4.4. Image size:  $5.3 \times 4.6$  mm<sup>2</sup> [66].

In n-octane, the oscillation does not extinguish the evolving Turing patterns, but it merges with the existing front. This front gets thin and a moment later it drifts apart, such that one part propagates into the direction away from the emerging Turing patterns and the other part towards the emerging patterns [arrows in Fig. 7.2(a)]. The front propagating towards the patterns later forms the labyrinth-like structures with the developing structures inside the rings.

However, in hexane a bulk oscillation forms a new ring around the evolving Turing patterns. The oscillation stops at a distance a little smaller than the characteristic wavelength of the

system and the medium between the oscillatory part and the existing patterns remains in the reduced state. When, the oscillating medium returns to the reduced state, the ring formed by the oscillation remains [Fig. 7.2(b)].

The described phenomenon of the interaction between bulk oscillations and emerging Turing patterns in n-octane and hexane can be clearly seen in the corresponding time-space plot [Fig. 7.3]. The horizontal lines correspond to bulk oscillations. In n-octane [Fig. 7.3(a)], the waves merge with the oscillations (arrows), such that the remaining wave splits up into two waves. Figure 7.3(b) shows the interaction with the solvent hexane. Here, the oscillations do not disappear, but form rings around the existing patterns and remain almost stationary in space.

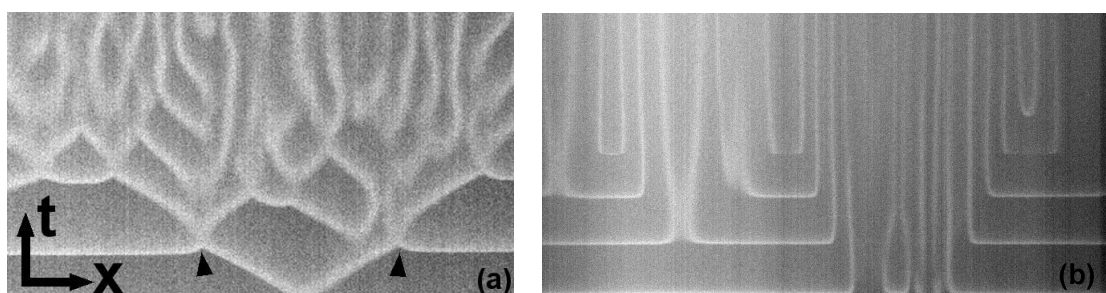


**Fig. 7.3.:** Time-space plots of the interaction between developing Turing patterns and bulk oscillations (a) in n-octane and (b) in hexane corresponding to Fig. 7.3. The horizontal lines are bulk oscillations. In (a), the oscillation merges with the waves, such that they split up (arrows). In (b) the oscillation forms a new ring around existing structures, which propagates slightly into the direction of patterns. However, the ring remains at a distance a little shorter than the characteristic wavelength of the patterns. The space resolution is 1 pixel = 0.58 mm and the time resolution 1 pixel = 2 s.

## 7.2. Bathoferroin-Catalyzed BZ Reaction

When the BZ reaction is embedded in a microemulsion, in particular with the catalyst BP, a rich variety of patterns can be found, which is surpassing by far the complexity found in the standard preparation in water or in an aqueous gel. One finds so-called dash waves and discontinuously propagating waves (jumping, rotating and bubble waves) [Fig. 7.4].

Under certain conditions, bubble waves are found to form anti-pacemakers, i. e., a situation in which wave fronts coming from different directions move towards a common center [Fig. 7.4(d)]. Dash waves can occur in a stable manner or in different unstable ones. In this case, stable means, that the initial wave front, from with the dashes evolve, can clearly be recognized and the dashes propagate like the original shape of the wave front. If dash waves become slightly unstable, they propagate like the initial wave only for a short time and start forming counter-rotating spiral waves. As the dashes become more unstable, they immediately start forming

spirals and the shape of the initial wave gets lost. The stability depends on the used recipe of the microemulsion. Dash waves are normally found around a droplet fraction of 0.45 [69]. However, the concentration of the reactants plays a crucial role. The ratio between the reactants is defined as  $\varepsilon = [\text{NaBrO}_3][\text{H}_2\text{SO}_4][\text{MA}]^{-1}$  [16]. This ratio should be around 0.14 to guarantee stable dash waves.

Bubble waves occur mostly at droplet fractions between 0.6 and 0.7 and  $\varepsilon = 0.12$  [16]. However, dash and bubble waves can co-exist in a narrow regime [Fig. 7.5(a)]. Bubble waves can evolve from rotating waves, but they can also be the initial pattern, which depends again on initial reactant concentrations.

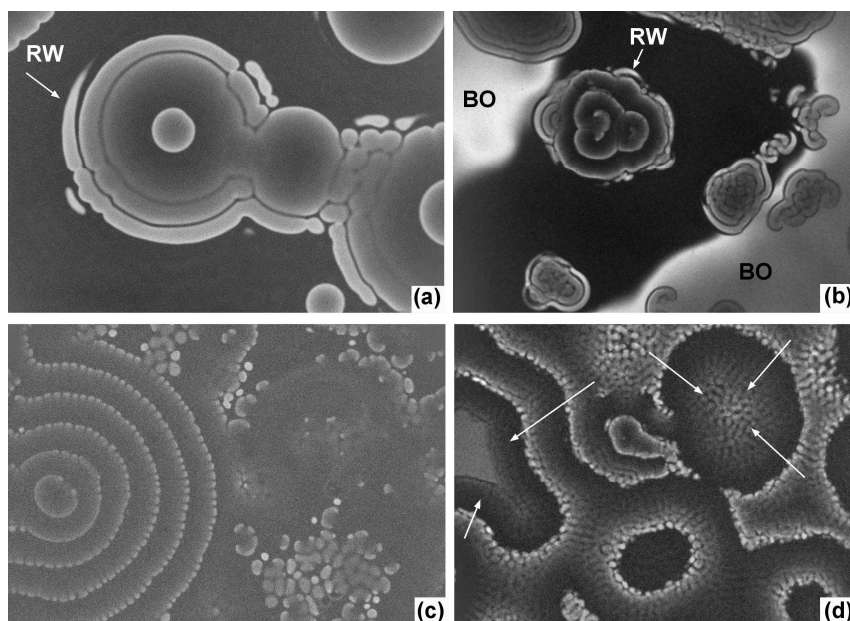


**Fig. 7.4.:** Overview of patterns occurring in the BP-catalyzed BZ reaction with n-octane. (a) Rotating waves (RW) occur in front of a wave front and rotate around it. Image size:  $8.1 \times 6.1 \text{ mm}^2$ . (b) RWs can co-exist with bulk oscillations (BO). Image size:  $11.8 \times 8.5 \text{ mm}^2$ . (c) Dash waves evolve from a target patterns, which can co-exist with bubble waves. Image size:  $5.3 \times 4.0 \text{ mm}^2$ . (d) Bubble waves can form anti-pacemaker (arrows show propagation direction of waves). Image size:  $11.8 \times 8.5 \text{ mm}^2$ .

In the following, some representative images are shown for patterns occurring in the BP-catalyzed microemulsion. Using hexane as the solvent, the patterns are qualitatively equal to that with n-octane [Fig. 7.5]. In the example with n-octane, a pacemaker occurs due to a small impurity at the beginning of the measurement, as shown in Fig. 7.4(a), which is an earlier instant of time of Fig. 7.5(a). Towards it, dash waves propagate from the upper left corner [Fig. 7.5(a)]. The patterns produced by the pacemaker develop from target patterns into rotating waves, which occur in front of the outer wave front. The rotating wave turns around this front, until it encompasses it. Then, the next wave occurs in front of the encompassed rotating wave. Over time, these waves propagate slowly away from the center of the pacemaker, since they disappear

after they occupied the whole reaction medium. Later, rotating waves develop into bubble waves [Fig. 7.5(a)]. When those discontinuously propagating waves approach the dash waves, they propagate much slower and stop before reaching the dash wave front. Therefore, the originally circular shape produced by the pacemaker disappears.

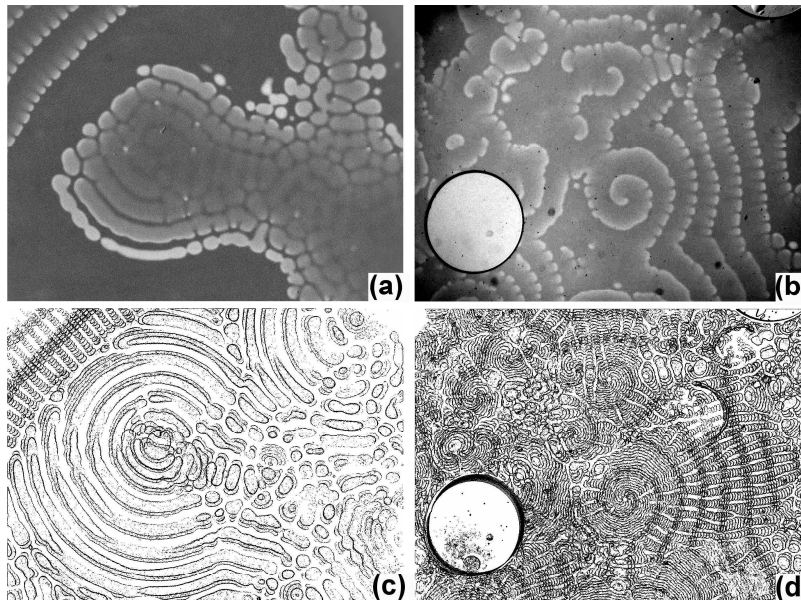


**Fig. 7.5.:** Snapshots of patterns in the BP-catalyzed BZ reaction with  $\omega = 12$  ( $\varphi_d = 0.455$ ) at  $t = 224.8$  min (a) in octane and (b) in hexane. Superposition of binarized images (c) in octane between 180.0 min and 189.2 min and (d) in hexane between 220.0 and 227.9 min with time interval of 40 s. Image size:  $8.1 \times 6.1$  mm<sup>2</sup>. For recipes see Table 4.5. Note, that the black lines in the superposition represent the oxidized state of the reaction [66].

Dash waves are also found for the same recipe with the other solvent. In experiments with hexane, a spiral wave is found. It is exemplarily depicted in Fig. 7.5(c). The wave front of this spiral is segmented. Interestingly, the dashes of one wave front propagate into the gaps of the previous one, i. e., the fronts are displaced relative to their precursor by the length of a dash [Figs. 7.5(b) and 7.5(d)].

The length of the dashes varies between 90 and  $(163 \pm 2)$   $\mu\text{m}$  and the length of the gaps varies from 40 to  $(104 \pm 2)$   $\mu\text{m}$  in both solvents for different  $\omega$ , respectively. The ratio between the length of the dashes and the length of the gaps ranges from 2.1 to  $2.4 \pm 0.1$  in the different experiments.

For convex waves, a splitting of dashes can be observed. The dashes propagate away from each other and their length increases, whereas the size of the gaps remains constant. Therefore, the length of the dashes immediately before splitting is 1.7 to  $1.9 \pm 0.1$  times larger than the length of the initial dashes. The segmentation begins near the core of the spiral or at the inner wave front produced by a pacemaker, since the curvature of the wave fronts is larger there than at the outer fronts.

A histogram of the curvature for different experiments is shown in Fig. 7.6, where the black curve corresponds to the experiments in Fig. 7.5(c). For a mid-range curvature (1.0 to 2.0  $\text{mm}^{-1}$ ), the number of splitting dashes is much higher than for small or large curvatures. This can be explained by the fact that large curvatures occur only near the spiral core, where the number of dashes is much smaller than at the outer wave fronts. With decreasing curvature, the dashes do not have enough lateral space to split up.

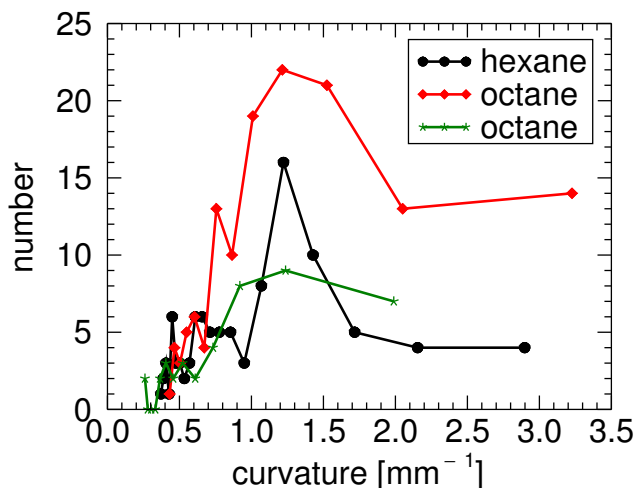


**Fig. 7.6.:** Histogram of the curvature  $K$  of a wave front, at which a splitting of a dash occurs. The recipes are equal for all experiments except the solvents:  $[\text{MA}] = 0.242 \text{ M}$ ,  $[\text{NaBrO}_3] = 0.174 \text{ M}$ ,  $[\text{H}_2\text{SO}_4] = 0.194 \text{ M}$ ,  $[\text{BP}] = 6 \text{ mM}$ ,  $\omega = 12$  and  $\varphi_d = 0.455$ . The pattern of the red curve is a dashed spiral wave, black is the dashed spiral in Fig. 7.5(b) and green is a dashed target pattern [66].

A splitting of the dashes can only be observed for convex wave fronts, where the dashes propagate away from each other. For a concave curvature (as in Fig. 7.5(a)) a merging of dashes is found. The gaps are getting smaller, such that dashes move closer together until they merge. Splitting or merging of the dashes cannot be observed for a curvature  $K$  between  $-0.10$  and  $(0.21 \pm 0.1) \text{ mm}^{-1}$ . Thus, for almost plain wave fronts, the dashes propagate straightforward without changing their length.

Using the Eikonal equation (1.4) [23], the influence of curvature on the velocity of a curved front is evaluated. The velocity of a plain wave  $v_0$  is chosen to  $1.1 \text{ m s}^{-1}$ , representing a typical value for the experiments. The diffusion coefficient  $D$  is taken from the approximation with the Stokes-Einstein equation (see Sect. 6.3):  $D = 2.26 \times 10^{-7} \text{ cm}^2 \text{ s}^{-1}$  or  $9.75 \times 10^{-8} \text{ cm}^2 \text{ s}^{-1}$  (depending on the droplet fraction). In Fig. 7.7 the result of the Eikonal equation is shown for all measured curvatures. From these results, it becomes apparent that the change in velocity of curved wave fronts is very small. Therefore, it is not necessary to take it into account in the experiments.



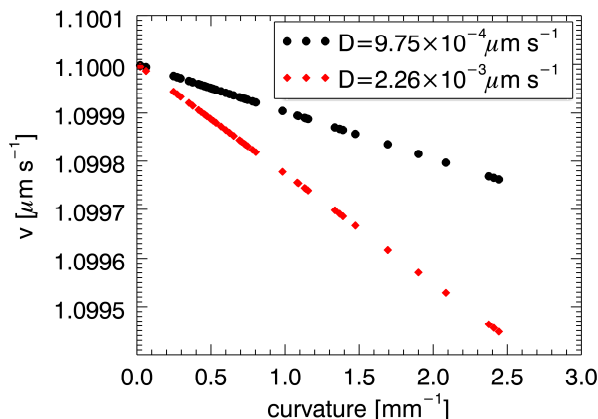


**Fig. 7.7.:** Influence of curvature on wave propagation velocity. Propagation velocities have been computed for all measured curvatures using the Eikonal equation. Results are shown for two different diffusion coefficients  $D$ . The initial velocity (of a plane wave) has been defined as  $1.1 \text{ m s}^{-1}$ . Chemical concentrations:  $[\text{MA}] = 0.242 \text{ M}$ ,  $[\text{NaBrO}_3] = 0.174 \text{ M}$ ,  $[\text{H}_2\text{SO}_4] = 0.194 \text{ M}$ ,  $[\text{BP}] = 6 \text{ mM}$ ,  $\varphi_d = 0.455$ ,  $\omega = 12$ .

### 7.3. Aging of Microemulsions

Storage of the microemulsion for more than one day results in different patterns. Hence, the microemulsions should always be prepared freshly to provide consistent results. For the experimental investigation of this effect, non-reactive microemulsions have been stored for a well-defined period of time. They have been mixed together immediately before the measurement starts, forming the reactive microemulsion.

The differences of patterns in a fresh and an old microemulsion can be clearly seen in Fig. 7.8. Here, patterns in a freshly prepared emulsion are shown in (a), where a target pattern develops into bubble waves (lower right corner). The outer wave fronts form a mixture of rotating and bubble waves, since the bubble like waves rotates clockwise.

The patterns of a one day old microemulsion can be seen in Fig. 7.8(b). Here, the system oscillates (bright regime in the upper left corner) and forms oscillatory localized patterns that are called oscillons [93]. The bright and the dark rings of the target-like structure oscillate alternately. After a short time, the oscillons break into small spots and a chaotic pattern emerges. This looks like many tiny counter-rotating spiral waves (left boundary of Fig. 7.8(b)). Furthermore, the patterns can only be found a few minutes after the start of the experiment in aged microemulsions. On the contrary, in freshly prepared emulsions patterns still occur 8 hours after the start of the experiment.

When storing the non-reactive microemulsions for more than one day, patterns can still be

observed. However, the time interval in which patterns are formed, becomes smaller and the oscillons turn out to be less stable. The chaotic pattern emerges earlier.

In experiments with BP, the resulting chaotic pattern of at least one day old microemulsions is the same, as with ferroin.

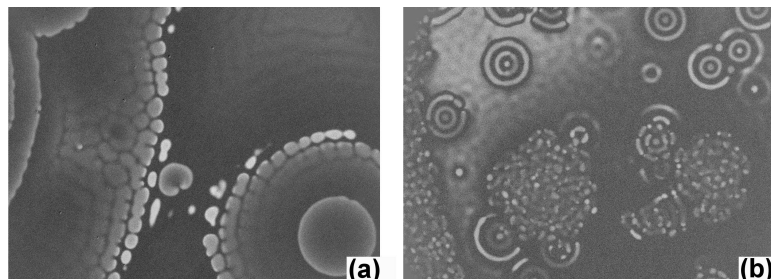


**Fig. 7.8.:** Effect of aging on the patterns in the microemulsion (n-octane, BP,  $\omega = 20$ ,  $\varphi_d = 0.478$ ). (a) Freshly prepared microemulsion. The patterns are monitored at  $t = 131.4$  min. (b) The two non-reactive microemulsions are stored for one day and mixed immediately before measuring ( $t = 25.5$  min). Image size:  $8.1 \times 6.1$  mm<sup>2</sup>.

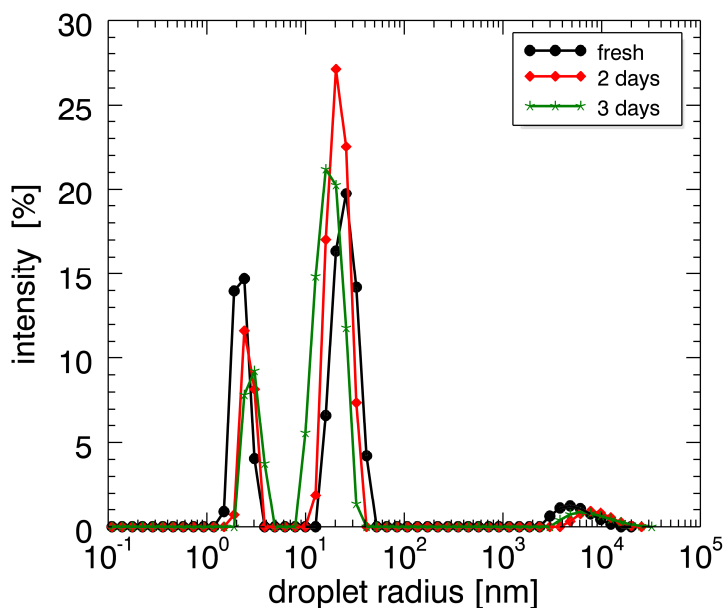


**Fig. 7.9.:** Effect of aging on the droplet radius in the BP-catalyzed microemulsion with n-octane ( $\omega = 20$ ,  $\varphi_d = 0.478$ ).

The effect of aging can also be seen in the droplet radius [Fig. 7.9]. The first maximum of the intensity peaks is shifted towards larger values of the droplet radius with the age of the system. The second peak shows the opposite behavior. A freshly prepared microemulsion has peaks at 2.39 nm and 25.75 nm, the two days old one at 2.39 nm and 20.31 nm and the three days old one at 3.036 nm and 16.01 nm. This means, that the two peaks move closer together and eventually, will form a single one. In this case the microemulsion would have reached thermodynamic

equilibrium.

## 7.4. Discussion

In this chapter, a mechanism for the effect of two different hydrocarbon solvents on the corresponding pattern formation is suggested. Previously, this was thought not to be of importance for pattern formation. Microemulsions with different chemical conditions are studied. Two different solvents and catalysts have been used, such that a total of four different cases can be compared. In the ferroin-catalyzed system, Turing patterns are observed, whereas with BP discontinuously propagating waves and dash waves can be found in both solvents. A phase diagram of patterns found in the BZ-AOT system is shown in Fig. 0.2.

In the ferroin-catalyzed system, the interaction of bulk oscillations with stationary Turing patterns differs for the used solvents. In n-octane, bulk oscillations merge with developing Turing patterns, whereas in hexane, the bulk oscillations form a new excited ring around the developing patterns. This type of development of Turing patterns is called "frozen waves" [94]), although this name was used earlier for precipitation waves in the BZ reaction [95].

The interaction between patterns and oscillations is called Turing-Hopf interaction. With octane, these interactions resemble the phase diffusion waves studied in Ref. [96], where a perturbation leads to a trigger wave. Moreover, the Turing-Hopf interaction observed in this work, can lead to different spatio-temporal patterns like oscillatory Turing patterns (see for example Refs. [87, 97]).

The interaction between bulk oscillations and waves in the aqueous BZ reaction, however, is competently different. Here, the oscillation extinguishes the outer wave front. Due to the larger period of oscillation compared to that of the wave pattern, a spiral wave or target pattern is able to occupy the whole reaction media, such that no oscillations exist at a late state of the experiment [47].

The differing Turing-Hopf type interactions for the solvents n-octane and hexane might be caused by the different partition coefficients for the activator ( $\text{HBrO}_2$ ;  $P_{act} = [\text{HBrO}_2]_{oil}/[\text{HBrO}_2]_{droplet}$ ) and the inhibitor  $\text{Br}_2$  in both solvents. The partition coefficient for  $\text{Br}_2$  between water and n-octane is 0.5 [98]. In the literature, no value for this coefficient could be found for hexane. If the coefficients  $P_{act}$  and/or  $P_{inh}$  change with the solvent, different patterns can emerge in different solvents, as observed for the BZ-microdroplets in a microfluidic device [99]. The ratio  $P_{act}/P_{inh}$  can affect the pattern formation in a quite similar manner as the ratio between diffusion coefficients.

In the BP-catalyzed system, dash waves and discontinuously propagating waves are observed [44]. The differences compared to the patterns found in the ferroin-catalyzed BZ-AOT system might occur due to the more hydrophobic character of BP, which is not soluble in water. Its molecules are located mostly in the hydrophobic AOT shell, yielding a clustering of nanodroplets [66]. This effect can be observed in dynamical light scattering measurements, where peaks at 50 - 100 nm occur, which are absent (or extremely small) with ferroin.

The occurring dash waves propagate in a similar way as waves studied in Refs. [100, 101]. In particular, the behavior of free wave fronts depends on the local excitability of the medium. They are found to increase or shorten their length, according to the given conditions [102].

The studied dash waves in this work, are observed to start segmentation of wave fronts near the spiral core, since the curvature of the wave front is highest there. Due to the convex wave front, the dash waves rapidly obtain enough lateral space to reach their splitting length. With decreasing curvature, the number of splitting dashes decreases. The curvature  $K$ , for which the most frequent splitting occurs, is  $(1.22 \pm 0.2) \text{ mm}^{-1}$ ; independent of oil and shape of the dominant pattern. The segmentation is found not to depend on the front velocity, since its change (which is a function of  $K$ ), is smaller than 0.5 ‰ of the velocity of a plane wave.

The displacement of the dashes between wave fronts may occur due to the predominant generation of the inhibitor in the dashes [69]. Therefore, this trace is not yet excitable, when the next wave front reaches it.

Furthermore, in microemulsions, long range interactions can be expected to occur due to percolation and the inhibitor dissolved in the oil phase. This can be seen in Fig. 7.2(b), where the bulk oscillation stops, before emerging Turing patterns. This type of interactions is also found with BP [Fig. 7.5(b)]. In this system, rotating waves and bubble waves have been observed to propagate much slower towards the dash wave front than into the other directions.

The effect of aging is also investigated in this chapter. Only the non-reactive microemulsions are stored for this purpose and mixed together immediately before the experiment starts. The patterns are found to be different than in freshly prepared emulsions and less stable. They exist for nearly 40 min (one day old microemulsions), whereas in the freshly prepared solutions, patterns are found for more than eight hours. When the non-reactive emulsions are stored for more than a day, the time in which patterns are found becomes shorter than 40 min.

Freshly prepared microemulsions have a bimodal distribution of the droplet radius [69, 78], as shown in Sect. 6.2. This seems to be energetically less stable. To further investigate this phenomenon, the droplet radius of stored emulsions is measured. As for the freshly prepared solutions, a bimodal distribution of the droplet radius can be observed [Fig. 7.9]. However, the

peaks of this distribution come closer together as longer as the emulsions are stored. The peaks are expected to merge, such that they form a single maximum located around 7 nm. In this case, droplet clusters are present in the system and Turing patterns cannot be found anymore.



# 8. The BZ-AOT system with 1,4-Cyclohexanedione

In this part, the BZ-AOT system as described in the previous sections and the bubble-free BZ reaction are combined (i. e., dissolving the bubble-free BZ reaction in the microemulsion) in a way, such that a bubble-free BZ-AOT microemulsion system is created. Thus, the phenomenon of anomalous dispersion and exotic patterns found in microemulsions should be linked to discover new patterns. Again, ferrouin and BP are used as catalysts. However, the patterns look similar in both cases. An overview of reactant concentrations is given in Table C.4.

The experiments always proceed in the same way: Starting with some initial waves or oscillations, the system transforms into an excited phase (for both catalysts) with the duration of several minutes up to a few hours. Afterwards, three different types of patterns are found, namely transient lines, wave turbulence and an intermediate pattern, representing a mixture of transient lines and wave turbulence. The kind of the resulting pattern depends on the initial concentrations of  $H_2SO_4$ ,  $NaBrO_3$  and CHD. In analogy to the BZ system with malonic acid [44], a ratio between initial concentrations of the reactants  $\varepsilon$  is defined as:

$$\varepsilon = \frac{[H_2SO_4][NaBrO_3]}{[CHD]}. \quad (8.1)$$

A series of experiments is performed to determine the influence of reactant concentrations on the resulting patterns (a selection of recipes is listed in Tables 4.6 and 4.7). The complete list of experiments is given in Table C.4. Transient lines are found for small values of the ratio  $\varepsilon$ . High values of  $\varepsilon$  result in chaotic wave propagation or spiral chaos and an intermediate ratio yields a mixed state between wave turbulence and transient lines, which is called intermediate state. This state and the transient lines differ slightly for the used two catalysts.

The investigated patterns in the BZ-AOT system with CHD are qualitatively comparable for ferrouin and BP.

Below, an overview for the ferrouin- and BP-catalyzed BZ-AOT system is given, listing the values of  $\varepsilon$  together with the resulting pattern:

- $0.096 \text{ M} \leq \varepsilon \leq 0.104 \text{ M}$ : transient lines (ferrouin and BP),
- $0.148 \text{ M} \leq \varepsilon \leq 0.150 \text{ M}$ : transient lines or intermediate state of ferrouin,
- $0.148 \text{ M} \leq \varepsilon \leq 0.200 \text{ M}$ : intermediate state of BP or wave turbulence,

- $0.185 \text{ M} \leq \varepsilon < 0.230 \text{ M}$ : intermediate state of ferroin,
- $0.230 \text{ M} \leq \varepsilon \leq 0.300 \text{ M}$ : intermediate state of ferroin or wave turbulence.
- $0.230 \text{ M} \leq \varepsilon \leq 0.500 \text{ M}$ : wave turbulence (ferroin and BP).

To study the effects of the reaction conditions in detail, two different droplet fractions are used, such that the effect of percolation can be investigated. In the BZ-AOT system with malonic acid, the droplet fraction governs the kind of pattern, since Turing patterns can only be found below the percolation transition [16]. In this chapter, droplet fractions of 0.4 and 0.59 are used in the microemulsion with CHD as organic substrate. No difference in the resulting patterns could be observed.

The remainder of this chapter is organized as follows: The first section describes initial waves and the excited state (Sect. 8.1), followed by the three types of observed patterns, transient lines, intermediate state and wave turbulence (Sects. 8.2–8.4). For all these cases, the results for both used catalysts are compared. The results will be discussed in the last section (Sect. 8.5).

## 8.1. Excited State

In all experiments with the bubble-free BZ-AOT system, the same course of events is observed: Starting with some initial waves or oscillations, the system transforms into an excited phase. Afterwards, three different types of patterns can occur.

Before the excited state sets in, some waves and/or bulk oscillations occur in the reaction. Circular waves are extinguished due to the oscillation. However, the period of the waves is slightly shorter than that of the bulk oscillation, such that the former dominate the reaction medium. The waves occurring before the excited state sets in show a remarkable behavior. Circular waves do not form a refractory state behind the front, but the medium remains excited. Closely behind such waves in the excited regime, a second wave front emerges, causing the previous wave to speed up [Fig. 8.1]. The second wave appears simultaneously behind the entire wave front (arrows in Fig. 8.1(a) and (b)) and leads to an increase in the velocity of the precursor wave front: Before the second wave emerges, the velocity of the first wave is  $(5.8 \pm 0.3) \mu\text{m s}^{-1}$ . With the formation of the second front, the velocity of the first one increases to  $(6.4 \pm 0.2) \mu\text{m s}^{-1}$ . The second wave propagates with a velocity equal to that of the first wave, before the second one emerges (i. e.,  $(5.8 \pm 0.3) \mu\text{m s}^{-1}$ ). After the disappearance of the precursor wave [Fig. 8.1(c)], again a new wave front is formed behind the remaining wave front (arrow in Fig. 8.1(d)).



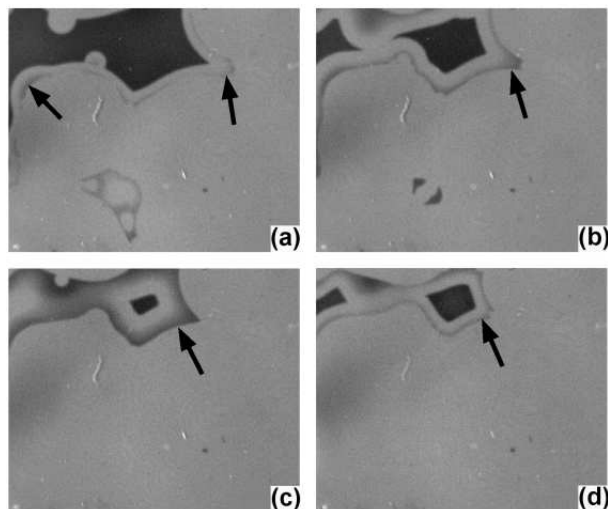


**Fig. 8.1.:** Waves occurring in the excited regime of the ferroin-catalyzed BZ-AOT system (recipe I, Table 4.6). (a) Behind the first wave front, a second one (arrows) emerges at  $t = 53$  min ( $t = 0$  corresponds to the start of the experiment). (b) The first wave front starts to propagate faster than the second one ( $t = 55$  min), such that (c) the distance between both wave fronts increases ( $t = 57$  min). When the first wave front disappears (d), a new front occurs behind the precursor (arrow) at  $t = 62$  min. The arrows mark the wave fronts, which occur behind the first one in the excited state. Image size:  $10.6 \times 7.9$  mm<sup>2</sup>.

The described scenario is also shown in a time-space plot [Fig. 8.2]. The green lines represent the first wave and the purple ones indicate the wave occurring behind the first wave. The slope of the green lines changes, when a wave occurs behind them. However, before a second wave occurs, the slope of green and purple lines is equal. The latter becomes the leading front (i. e., green line), when the first wave front disappears due to other waves or bulk oscillations.

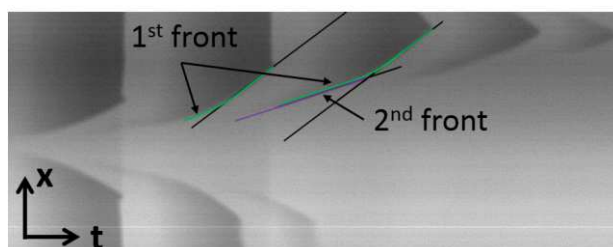


**Fig. 8.2.:** Time-space plot of waves in the BZ-AOT system with CHD. Behind a wave (green line), the medium remains excited, but a second wave emerges within (purple line). The black lines represent the propagation velocity of the wave fronts, to illustrate the different slopes of the first and second wave. The purple line shows the second wave, which becomes green, when the precursor (first) wave disappears. Space resolution: 1 pixel = 0.14 mm, time resolution: 1 pixel = 2 s.

Furthermore, the conductivity of the CHD system with ferroin is measured to determine the percolation threshold [Fig. 8.3]. The course of the conductivity of recipe III is comparable to that in the standard system (compare Fig. 6.1). However, at  $\varphi_d = 0.5$ , the conductivity in the bubble-free BZ-AOT system is above  $1 \mu\text{S cm}^{-1}$ , whereas with malonic acid it is below 1

$\mu\text{S cm}^{-1}$  (compare Fig. 6.1).

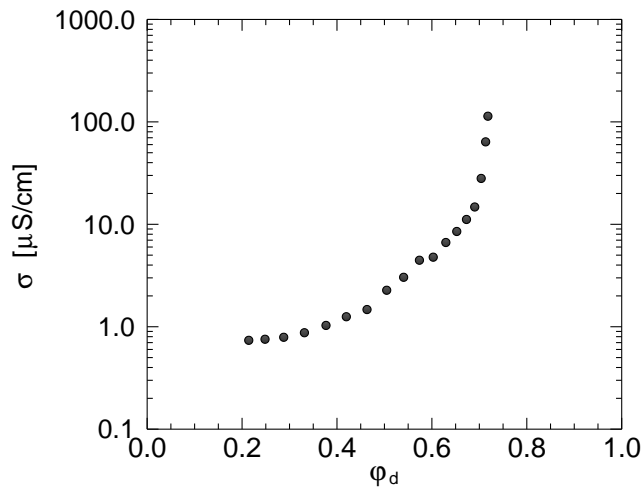


**Fig. 8.3.:** Conductivity of two different recipes (Table 4.6) in the bubble-free BZ-AOT system with ferriin.

The duration of the excited state is different in the experiments. It lasts between 50 and 225 min. The corresponding distribution of the duration of the excited state for ferriin (red bars) and BP (yellow bars) is shown in Fig. 8.4. For the majority of cases, the excited state lasts for about 165 min. This value is found to be independent of the used catalysts, since the distribution of the duration is almost the same for both catalysts.

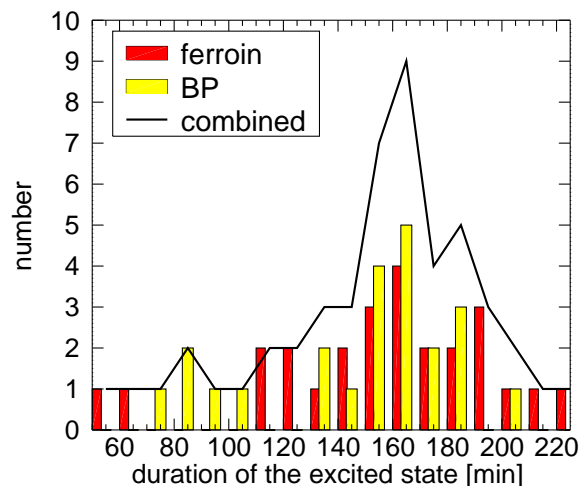


**Fig. 8.4.:** Histogram of the duration of the excited state for ferriin (red bars) and BP (yellow bars). The black line indicates the combination of both catalysts.

The relation between  $\varepsilon$  and the duration of the excited state is studied in Fig. 8.5(a). It becomes

apparent, that most of the values of the excited state duration lie around the maximum of 165 min, but at very different ratios  $\varepsilon$ . Furthermore, no effect of the droplet fraction on the duration of the excited state is found [Fig. 8.5(b)].

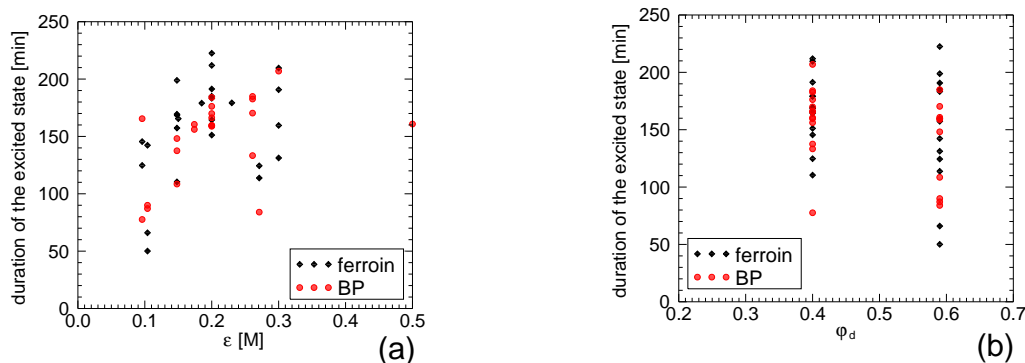


**Fig. 8.5.:** (a) Duration of the excited state versus the ratio of the reactant concentrations and (b) duration of the excited state versus droplet fraction  $\varphi_d$  of the BZ-AOT system for ferroin (black diamonds) and BP (red circles).

## 8.2. Transient Lines

When the excited state is over, three different kinds of patterns can emerge, depending on the ratio between the reactants  $\varepsilon$ : transient lines, wave turbulence or an intermediate state. In this section, transient lines for the catalysts ferroin and BP are presented.

In the ferroin-catalyzed system, the excited state (bright regimes in Fig. 8.6) disappears in a way, that some regimes become excitable (dark) and the rest remains excited. Thus, the excited state develops spacial discontinuities. A small value of  $\varepsilon$  (i. e.,  $0.096 \text{ M} \leq \varepsilon \leq 0.150 \text{ M}$ ) yields line formation. This proceeds in the following manner: in some regimes, the system recovers and returns to the excitable state. The other regimes stay excited and a line pattern remains. These lines are called "transient lines", since they exist only for a short time (between 20 and 35 min). In Fig. 8.6 an example of these lines is shown. Transient lines appear gradually [Fig. 8.6(a) and (b)], until they occupy the entire reactor [Fig. 8.6(c)]. The resulting pattern looks like a mixture of target and labyrinth-like patterns, but they are no Turing patterns. An amplitude spectrum of Fig. 8.6(c) is calculated using the spatial Fourier transform to examine this statement. A homogeneous wavelength distribution from 0 to  $(95 \pm 10) \mu\text{m}$  is found with no specific wavelength standing out [Fig. 8.6]. Subsequently, the transient lines start to disappear [Fig. 8.6(d)]. Note, this process begins in the regime, where the transient lines are formed first.

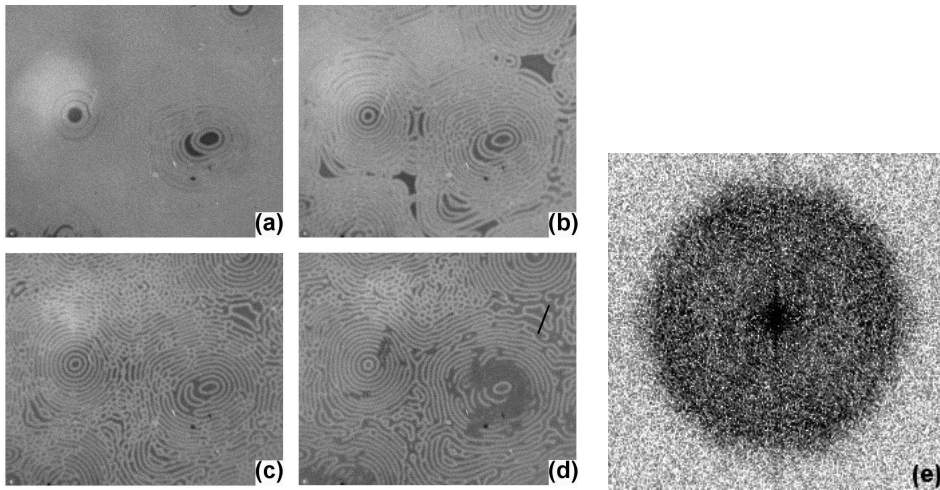


**Fig. 8.6.:** Transient lines emerging after the excited state in the ferroin-catalyzed system (recipe I, Table 4.6). (a) Target pattern-like structures start emerging at  $t = 119$  min, (b) which grow with time ( $t = 127$  min), (c) until they occupy the entire reactor at  $t = 137$  min. (d) After a short time, the transient lines start disappearing near the center of the target-like structures, where they developed first ( $t = 174$  min). (e) Amplitude spectrum of (c). Image size:  $10.6 \times 7.9$  mm<sup>2</sup>.

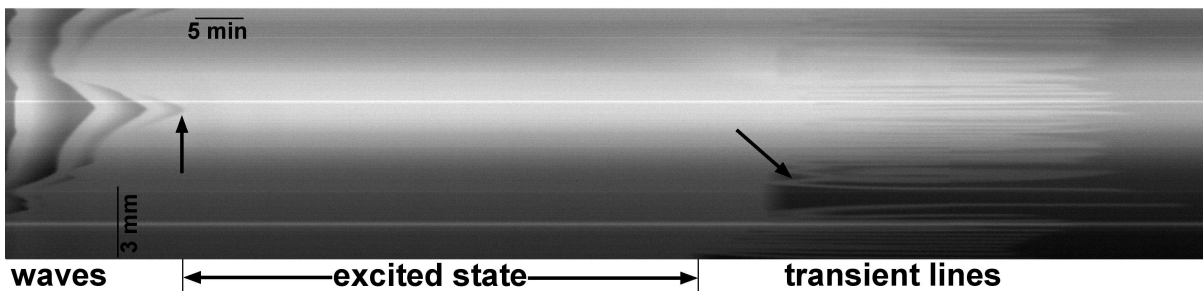


**Fig. 8.7.:** Time-space plot of the development of transient lines of recipe I (Table 4.6). After starting the experiment, waves develop as described in Sect. 8.1. Behind the first wave front a second one emerges directly from the excited state (left arrow). The excited state lasts 50 min and afterwards transient lines appear. The line emerging first, splits up into two ones shortly after its formation (right arrow).

In Fig. 8.7, a time-space plot of the experiment in Fig. 8.6 is shown. At the left side (marked with "waves") some circular waves emerge, which grow together and form the excited state. The left arrow indicates a second wave front, which is formed in the excited regime behind a precursor wave front, as described above. Some of the transient lines remain after the excited state expired. Initially some of them are single ones, splitting up into two lines (right arrow in Fig. 8.7). These lines slightly drift away from each other and remain in close distance from each other for the rest of their lifetime. Lines, which do not split up, remain at their position in most cases.

A gray value profile of transient lines is shown in Fig. 8.8. The individual profiles are rather symmetric, indicating that the transient lines are no propagating waves, which would have a

steep wave front and a slowly decreasing tail [103].

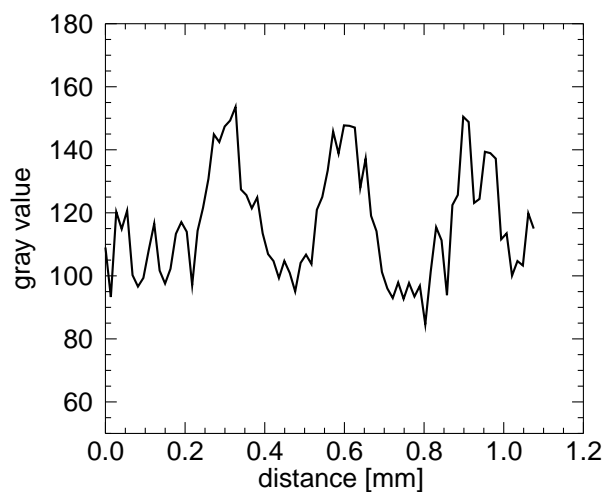


**Fig. 8.8.:** Gray value profile of the transient lines, taken along the black line in Fig. 8.6(d).

In the experiments with BP, transient lines can be observed in the interval  $0.096 M \leq \varepsilon \leq 0.104 M$  [Fig. 8.9]. The excited state disappears [Fig. 8.9(a)] and the lines remain [Fig. 8.9(b)]. It is worth mentioning, that remaining lines have the same shape, as the disappearing excited state. The lines are closer together in the area, where the excited state dissipates slowly, than in the regimes, where it disappears faster. After a short time, the system starts to recover, until it reaches the homogeneous state [Fig. 8.9(c)]. All transient lines disappear in the BP-catalyzed system at almost the same time.

However, the pattern formation in this system differs from that in the ferroin system. Here, the excited state is connected while disappearing. In the ferroin-system, the excited state breaks up such that gaps in the excited state occur, where the system is already in the excitable state.

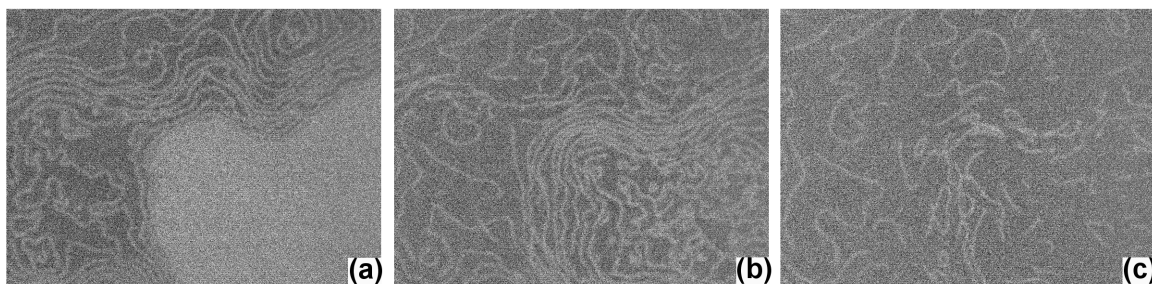


**Fig. 8.9.:** Development of transient lines in the BP-catalyzed BZ-AOT system for recipe 1 (Table 4.7). (a) Transient lines emerge from the excited state at  $t = 208$  min, (b) they are fully developed at  $t = 218$  min and (c) start disappearing at  $t = 229$  min. Image size:  $10.6 \times 7.9$  mm<sup>2</sup>.

Fig. 8.10 shows a time-space plot extracted from Fig. 8.9. At the beginning of the measurement, waves appear, which grow together and form the excited state. Here, the phenomenon of a second

wave forming behind the first one can also be observed (arrow in Fig. 8.10), as already described above. Furthermore, it can be seen, that the excited state does not end abruptly, but becomes excitable earlier in certain regimes than in others. This results in some propagation of the transient lines, until they remain at their place (horizontal lines on the right side of Fig. 8.10).

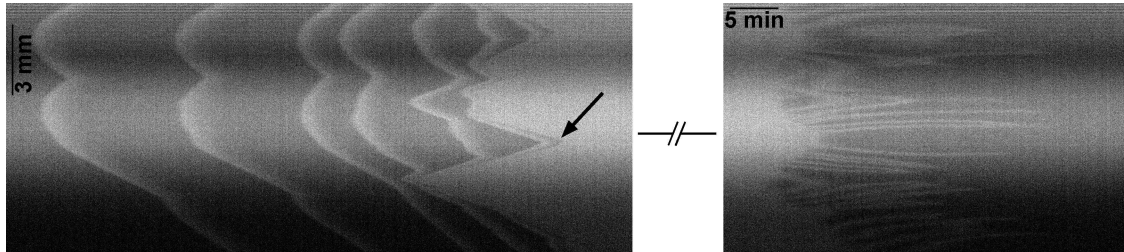


**Fig. 8.10.:** Time-space plot of the transient lines in the BP-catalyzed BZ-AOT system for recipe 1 (Table 4.7). At the beginning, waves occur in the system as well as second waves (arrow) forming within the excited state (as in Fig. 8.7). After 77.6 min, they are fully merged and form the excited state. Afterwards, the transient lines emerge.

### 8.3. Intermediate State

The intermediate state is a mixture of transient lines and turbulent waves. It occurs in an interval of a mean  $\varepsilon$ :  $0.150 \text{ M} \leq \varepsilon < 0.230 \text{ M}$  for ferroin and  $0.148 \text{ M} \leq \varepsilon \leq 0.200 \text{ M}$  for BP. The patterns show both, the characteristics of transient lines and wave turbulence [Fig. 8.11]. When the system becomes excitable, some excited lines remain [Fig. 8.11(a)], which propagate slowly. These lines tend to form waves [Fig. 8.11(b)].

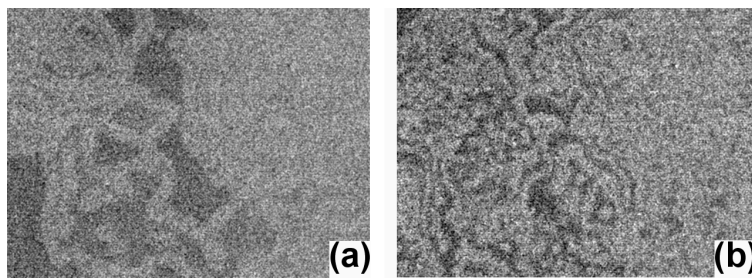


**Fig. 8.11.:** Intermediate state of the ferroin-catalyzed system (recipe II, Table 4.6). (a) From the excited state, large, thick lines remain at  $t = 115 \text{ min}$ . These lines split up and form smaller ones. (b) Subsequently, a transition from these lines into propagating waves occurs at  $t = 139 \text{ min}$ . Image size:  $8.4 \times 6.3 \text{ mm}^2$ .

The difference between the intermediate state and the two other types of patterns found in this system can be clearly seen in the time-space plot [Fig. 8.12]. When the system recovers to the excitable state, some thick lines remain (arrows in Fig. 8.12). These lines split up and form wave fronts, which propagate into opposite directions (similar to the Turing-Hopf interactions

in the BZ-AOT system with malonic acid [66]). These waves, however, propagate very slowly, i. e., in the range of  $0.1 \mu\text{m s}^{-1}$ .

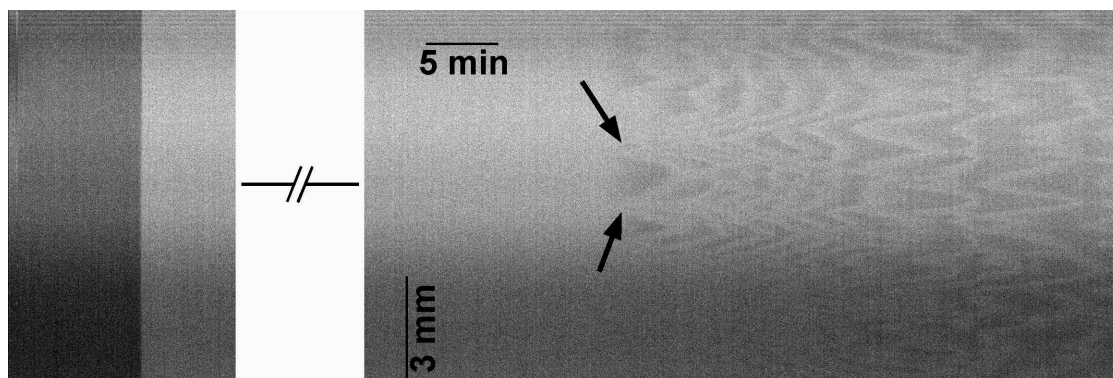


**Fig. 8.12.:** Time-space plot of the development of the intermediate state with ferroin (recipe II, Table 4.6). The arrows indicate the emergence of thick lines which split up into smaller ones. From these lines a transition into propagating waves occurs. The duration of the excited state is 110.4 min.

In the BP-catalyzed system, the intermediate state differs qualitatively from the patterns found with ferroin. At first glance, the lines in Fig. 8.13 look similar to transient lines. However, these lines have a larger distance from each other than transient lines and tend to form spirals or circular waves. The waves in Fig. 8.13(a) occur after the excited state in the same manner as the transient lines in Fig. 8.9. They are propagating very slowly (i. e.,  $0.62 \mu\text{m s}^{-1}$ ) towards the upper left corner of the image [Fig. 8.13(b)]. Over time, the distance between the waves is getting larger. This might be attributed to aging [Fig. 8.13(c)]. Furthermore, the waves can merge with circular waves in front of them, such that the wave front remains intact. Note, that most of the wave fronts are not interrupted within the field of view. In Fig. 8.13(b) and (c), some wave fronts break and open wave ends remain (arrows). These open ends tend to form spirals, but the velocity of the waves is too slow to complete spiral formation.

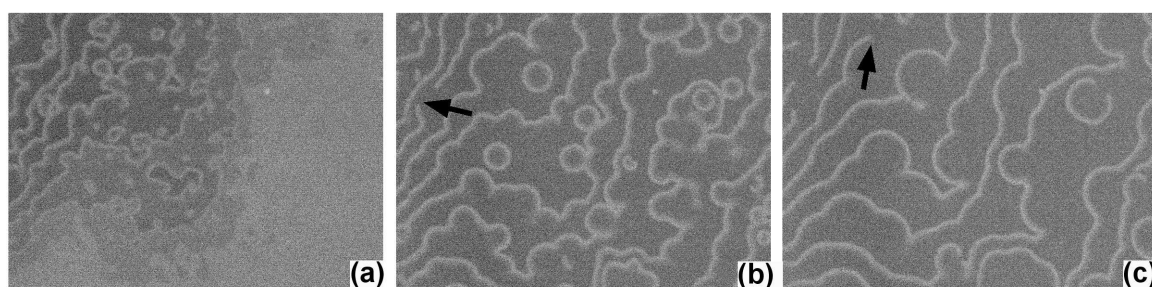


**Fig. 8.13.:** Development of the intermediate state in the BP-catalyzed system (recipe 2, Table 4.7). (a) Slowly propagating waves remain when the excited state ends at  $t = 229$  min. (b) Fully developed intermediate state at  $t = 239$  min. (c) The distance between the waves increases and later they start to disappear at  $t = 252$  min. The arrows point to open wave ends that fail to form spiral waves. Image size:  $10.6 \times 7.9 \text{ mm}^2$ .

In Fig. 8.14, a time-space plot extracted from Fig. 8.13 (intermediate state) is shown. At the beginning, waves are formed and a second wave emerges in the refractory regime of a precursor wave (arrow) as described in Sect. 8.1. When the excited state is over, typical wave propagation can be seen: some of the lines in the time-space plot are inclined and run parallel to each other.

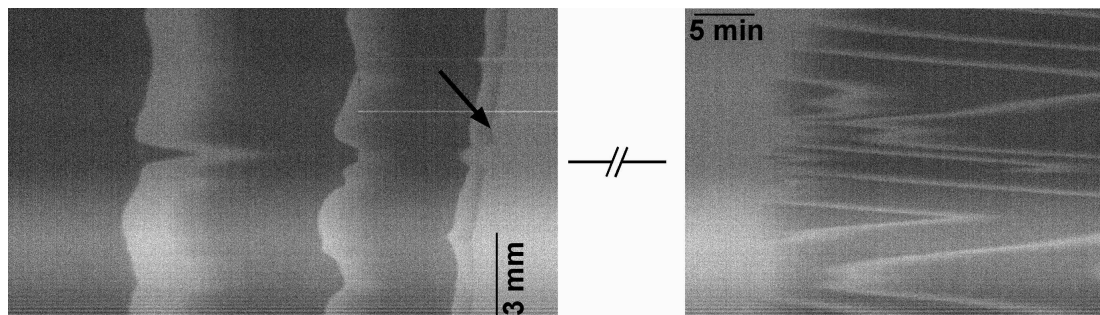


**Fig. 8.14.:** Time-space plot of the intermediate state with BP (recipe 2, Table 4.7). A second wave occurs within the excited state (arrow) as in Fig. 8.7. The excited state takes 159.6 min and afterwards, slowly propagating waves occur.

## 8.4. Wave Turbulence

A high ratio of the reactant concentrations of the BZ medium ( $0.230 \text{ M} \leq \varepsilon \leq 0.300 \text{ M}$  for ferroin and  $0.230 \text{ M} \leq \varepsilon \leq 0.500 \text{ M}$  for BP) results in chaotic waves after the excited state.

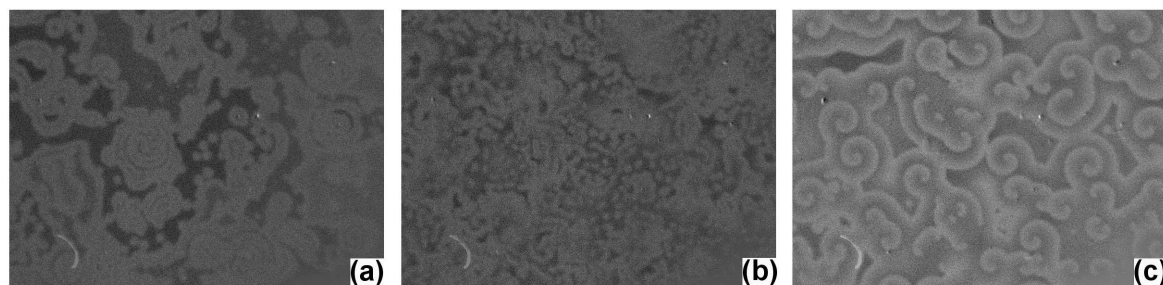


**Fig. 8.15.:** Spiral turbulence developing after the excited state in the ferroin system (recipe III, Table 4.6). (a) At  $t = 139$  min the developing patterns are characterized by large distances between each other. (b) This distance becomes smaller at  $t = 151$  min. (c) Fully developed spiral turbulence ( $t = 193$  min), in which the wavelength of the spirals is larger than in (b). Image size:  $10.6 \times 7.9 \text{ mm}^2$ .

The image sequence in Fig. 8.15 illustrates the development of such a turbulence for ferroin. Initially, the patterns look similar to those shown in Fig. 8.11. Analogue to that system, thick lines are also formed here [Fig. 8.15(a)]. However, they propagate much faster than the patterns in the intermediate state and interact with neighboring waves [Fig. 8.15(b)]. Thus, the resulting structures are spiral waves [Fig. 8.15(c)] or many small interacting waves. During the evolution of the wave turbulence, the wavelength of the patterns changes; it first decreases and increases



again, when the spirals are formed. This can also be seen in the corresponding time-space plot [Fig. 8.16]. The distance between the waves in horizontal direction changes until spiral waves are fully developed. When spirals are formed, the wavelength remains constant.

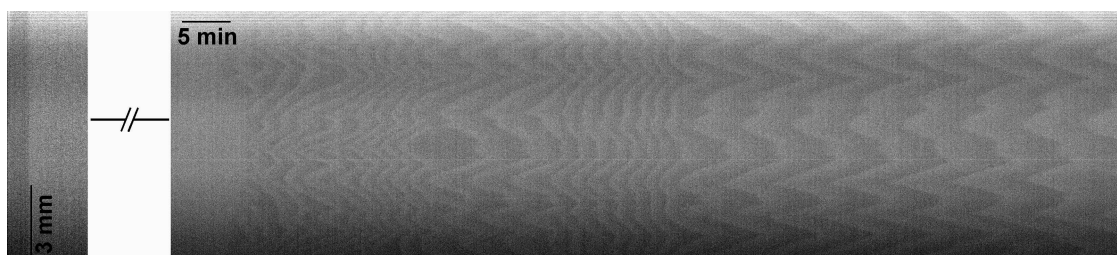


**Fig. 8.16.:** Time-space plot of wave turbulence with ferroin (recipe III, Table 4.6) extracted from Fig. 8.15. The excited state lasts 124.4 min and afterwards turbulent waves occur, which change their wavelength. Subsequently, spiral chaos is formed.

A high ratio  $\varepsilon$  with BP also results in turbulent waves or spiral chaos following the excited state (recipe 3, Table 4.7). This is comparable to the observations made with ferroin.

## 8.5. Discussion

In this chapter, the ferroin- and BP-catalyzed bubble-free BZ reaction embedded in a microemulsion is studied. This system varies significantly with respect to the standard BZ-AOT system with malonic acid (as described in Sect. 7). Some new kinds of patterns are found, governed by the ratio  $\varepsilon$  of initial concentrations of  $\text{NaBrO}_3$ ,  $\text{H}_2\text{SO}_4$  and CHD. The ratio  $\varepsilon$  is defined as  $\varepsilon = [\text{H}_2\text{SO}_4][\text{NaBrO}_3][\text{CHD}]^{-1}$  referring to the definition with malonic acid [16]. This ratio gives only a rough relation of the activating and inhibitory interactions of the chemical species [16], but is quite useful to characterize the studied system.

All experiments proceed in the same manner: At the beginning, some waves and/or bulk oscillations appear, followed by an excited state, which lasts between 50 and 225 min. Subsequently, transient lines, an intermediate state or wave turbulence occur, depending on  $\varepsilon$ . A small ratio  $\varepsilon$  yields transient lines whereas for a high ratio wave turbulence can be found. The intermediate state occurs in between. These three types of patterns are qualitatively comparable for the catalysts ferroin and BP.

Before the excited state begins, some waves occur in the experiment. These waves show a fascinating behavior, since behind a wave front, a second one is formed without the presence of a pacemaker. With the occurrence of the second wave, the precursor speeds up [Fig. 8.2]. A similar behavior can be found in the aqueous bubble-free BZ system, when anomalous dispersion of wave propagation occurs [22, 35, 37]. In the aqueous system, the initial wave is slower than

the following waves, such that they merge with the leading pulse or get stacked behind. In fact, the distance between the waves determines their propagation velocity [22].

In this study, the velocity of the first wave changes, whereas in the aqueous system, propagation velocity remains constant. The described increase in the propagation velocity of a wave (when a second one is formed in its wake) might be a hint that anomalous dispersion can occur in the studied system. However, no stacking or merging of waves could be observed in this work. Probably, the excitability of the used recipes is too low. Anomalous dispersion in the aqueous system can only be found at high excitability [35]. Additionally, a requirement for anomalous dispersion is the existence of periodic wave trains [38], which have not been observed in the bubble-free BZ-AOT system.

The excited state that is observed after the above mentioned waves might correspond to some kind of induction time of the reaction, since no pattern formation occurs during this time. An induction time is well known from the aqueous BZ reaction with CHD [33]. However, in the aqueous system, no waves or oscillations occur before the induction time sets in.

The measurement of the electric conductivity of the bubble free BZ-AOT system reveals a behavior of the conductivity (as a function of the droplet fraction) which is comparable to that of the standard BZ-AOT system (compare Figs. 6.1 and 8.3). However, the conductivity using recipe I does not decrease as fast as for recipe III with increasing amount of oil. Furthermore, the conductivity at  $\varphi_d = 0.71$  is much higher than in the measurement of recipe III. During the conductivity measurement of recipe I, the microemulsion did not enter the excited state or showed oscillations, contrary to all other measurements using this recipe. This indicates, that the measurement of the conductivity of recipe I is not representative. However, together with the conductivity of recipe III it shows, that the electric conductivity is above  $1 \mu\text{S cm}^{-1}$  at  $\varphi_d = 0.5$  in the CHD system, whereas with malonic acid the conductivity is below  $1 \mu\text{S cm}^{-1}$  (compare Fig. 6.1).

In the results of the observation of patterns in this system, no difference between the patterns above and below  $\varphi_d = 0.50$  could be observed. Thus, with the used droplet fraction of 0.40, the conductivity is still too high to observe other patterns than with  $\varphi_d = 0.59$ . Probably patterns occurring below the percolation threshold might be observed at a droplet fraction of 0.30.

The intervals of the initial concentration ratio  $\varepsilon$  are found to be almost equal for the two used catalysts, as far as it can be stated from the limited number of experiments (compare Table C.4). This, as well as the fact that the observed patterns are qualitatively almost the same for both catalysts, is surprising, since in the standard BZ-AOT system (with malonic acid) patterns differ significantly for these two catalysts. Below the percolation transition Turing patterns

(spots or labyrinths) can be found, in the ferroin-catalyzed system. With BP, dash waves and discontinuously propagating waves, like jumping and bubble waves, have been observed [44, 66]. The only remarkable difference between the patterns described in this chapter, is their formation process. In the ferroin case, the excited state disappears non-homogeneously. The system returns to the excitable state at different regimes of the medium, leaving behind some excited thick lines. From these lines, all three types of patterns can develop.

"Transient lines" [Fig. 8.6], for example, develop when thick lines split up into two lines that slightly propagate away from each other, such that their distance is almost equal to the thickness of a line. However, transient lines have nothing in common with Turing patterns. In the studied system, a homogeneous wavelength distribution is found [Fig. 8.6], whereas in the Turing case, a single well-defined wavelength dominates [1].

With BP, the excited state is spatially connected and starts to disappear at one point, from which the excitable state expands. The resulting type of pattern remains. This different disappearance behavior might be caused by the catalyst. BP is more hydrophobic than ferroin, which means, that the water droplets with BP are larger. Due to its hydrophobic character, the BP molecules are mostly located in the AOT shell. This changes the observed pattern in the standard BZ-AOT system [66]. Furthermore, the appearance of transient lines and intermediate state differs slightly with the two catalysts. However, in the standard BZ-AOT system, the difference of patterns is much clearer than in the bubble-free microemulsion.

The intermediate state can be characterized as slowly propagating wave-like structures, which can be seen in the corresponding time-space plots [Figs. 8.12 and 8.14]. The clear wave structures with BP show open wave ends [Fig. 8.13] that do not form spirals. This behavior is already known from the aqueous BZ reaction with malonic acid with low excitability [101]. It also gives a hint that the used excitability in the experiments is too low to observe anomalous dispersion. Fig. 8.4 shows the duration of the excited state for ferroin, BP and for the combination of both. The mean duration lies around 165 min, which is much longer than the typical time of the induction period in the aqueous CHD-BZ system (5 – 90 min) [33]. In that system, the induction period is known to depend on the concentrations of the reactants (i. e., bromide ions) [33]. In the microemulsion system, however, no influence of the reactant concentrations could be found. With equal concentrations, the duration of the excited state varies around 100 min in repeated experiments [Fig. 8.5(a)]. Here, the duration of the excited state for ferroin and BP shows no correlation with the excitability of the medium. Also the droplet fraction does not show any effect on the duration. However, this can be explained by the conductivity at  $\varphi_d = 0.5$ , which suggests, that the system is still above the percolation threshold. Thus, it is assumed,

that the duration of the excited state is almost random.

# 9. Electric Field Effects on Patterns in a Microemulsion

In this chapter, the effect of homogeneous electric fields is studied. Here, only octane is used as the solvent but ferroin and BP are taken as catalysts. With ferroin, Turing patterns can be observed. These stationary patterns are well suited to study drift of patterns induced by an electric field. In the BP-catalyzed system, spiral waves are the common observed patterns. The drift of these dynamic patterns results either from their own rotation or from the electric field. The layer thickness is changed in experiments with electric fields (Sect. 9.1). These experiments are only performed using DC. For follow-up experiments, both direct current (Sect. 9.2.1) and alternating current (Sect. 9.2.2) are used. Patterns are found to drift under the influence of static electric fields. However, alternating electric fields do not result in pattern drift.

## 9.1. Effect of the Layer Thickness

Two different values of the layer thickness are used in the performed experiments, to investigate its effect. The used electrodes are 100  $\mu\text{m}$  and 220  $\mu\text{m}$  thick.

The layer thickness affects the studied system in different ways: using ferroin in 220  $\mu\text{m}$  thick layers, three dimensional effects can be observed, thus the patterns are blurred. The characteristic wavelength of the patterns lies around 200  $\mu\text{m}$ , which lies in the range of the electrodes with 220  $\mu\text{m}$  thickness. Nevertheless, the three-dimensionality has no effect on the qualitative drift of the patterns. The drift velocity lies around 0.74  $\mu\text{m s}^{-1}$  for electric field strengths between 11 and 14  $\text{V cm}^{-1}$ . A layer thickness of 100  $\mu\text{m}$  results in velocities of 0.28 up to 1.26  $\mu\text{m s}^{-1}$  for field strengths between 9 and 16  $\text{V cm}^{-1}$ . In both cases, the drift is linear during the measurement, as shown in Fig. 9.6. A detailed analysis of the pattern drift with layer thickness of 100  $\mu\text{m}$  is presented in Sect. 9.2.

Using the BP-catalyzed system with a layer thickness of 220  $\mu\text{m}$ , the patterns drift into opposite directions, when the field is applied, i. e., they smear. In Fig. 9.1, the layer thickness is 220  $\mu\text{m}$ . Rotating and jumping waves can be observed together with co-existing bulk oscillations as shown in Fig. 9.1(a). At the bottom of the image, jumping waves develop from a target pattern. The upper structure is initially a counter-rotating pair of spiral waves, which also develops into jumping waves. After applying an electric field, this patterns show a drift into two directions:

towards the positive and the negative electrode, under a certain angle with respect to the horizontal field lines [Fig. 9.1(b and c)]. The upper pattern shows a larger inclination to the field lines than the lower one, since the rotation of the spirals affects the drift [48]. The patterns drift into two directions (they are "smearing out") as a result of the layer thickness (220  $\mu\text{m}$ ) of the microemulsion. The sodium ions of the surfactant AOT, which are located inside the water droplets, are positively charged and can polarize the droplets [60]. Other ions (positively and negatively charged) from the BZ reaction also contribute to the polarization. Thus, a pattern drift towards the negative electrode occurs due to the protons and sodium ions (right side of Fig. 9.1), whereas the inhibitor and some other ions are negatively charged, leading to a drift towards the positive electrode.

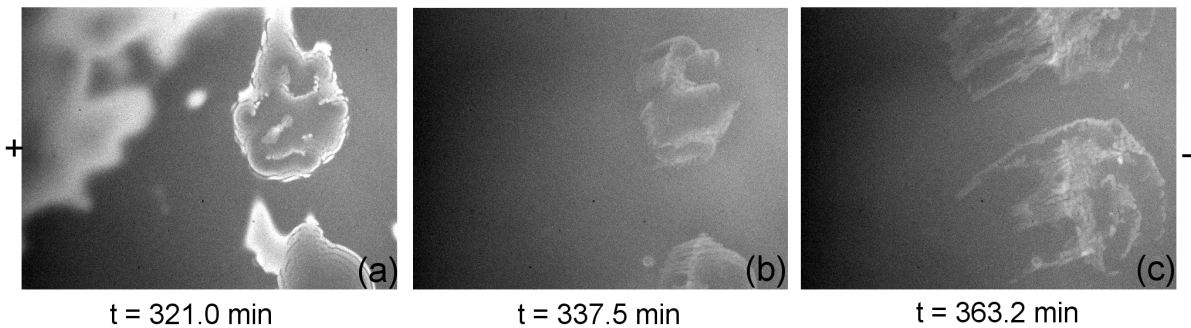


**Fig. 9.1.:** Snapshots of smearing patterns in the BP-catalyzed BZ-AOT system with a layer thickness of 220  $\mu\text{m}$ . (a) Jumping and rotating waves co-exist with bulk oscillations in the system before an electric field is applied. (b and c) Immediately after the application of the electric field (10  $\text{V cm}^{-1}$ ) patterns start to drift diagonally, with respect to the field lines, towards both electrodes. Concentrations:  $[\text{MA}] = 0.291 \text{ M}$ ,  $[\text{NaBrO}_3] = 0.175 \text{ M}$ ,  $[\text{H}_2\text{SO}_4] = 0.195 \text{ M}$  and  $[\text{BP}] = 4.94 \text{ mM}$ ,  $\varphi_d = 0.7$ ,  $\omega = 14.9$ . Image size:  $11.7 \times 8.6 \text{ mm}^2$  [104].

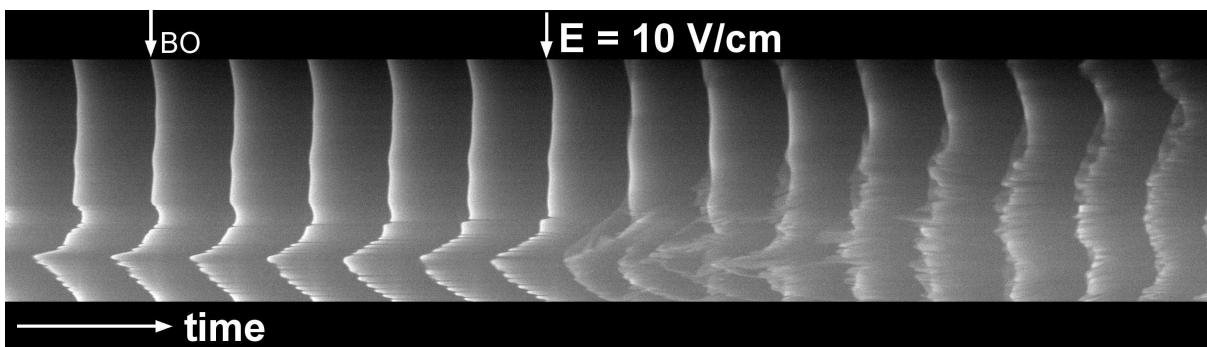


**Fig. 9.2.:** Time-space plot from 140.51 to 237.18 min of Fig. 9.1 along a horizontal line through the lower pattern (initially target pattern). The bulk oscillations (BO) are the vertical lines and the broken lines correspond to jumping waves. After the application of the field (10  $\text{V cm}^{-1}$ ), the patterns drift towards the positive and negative electrode. The space resolution is 1 pixel = 0.18 mm and the time resolution 1 pixel = 2 s [104].

In the corresponding time-space plot [Fig. 9.2], the drift of the patterns from Fig. 9.1 into opposite directions is clearly observable. The bright vertical lines are bulk oscillations (BO) in

the system and the broken lines in the lower part correspond to jumping waves. These clear wave structures are instantaneously destroyed after the application of the electric field (field onset indicated by the arrow in Fig. 9.2). Weak structures occur in front of the initial wave and partly behind.

A layer thickness of 100  $\mu\text{m}$  yields a clearly observable drift of patterns towards the positive electrode. In Fig. 9.3, some pairs of counter-rotating spiral waves are shown. The upper pair drifts towards the positive electrode, directly after the application of the field. In Fig. 9.3(c) the trajectory of the left core from the upper spiral pair is shown. Over a duration of 85 min, the spiral pair drifts 0.39 cm into the direction of the positive electrode. Thus, the resulting drift velocity is  $(0.76 \pm 0.01) \mu\text{m s}^{-1}$ . As expected for a layer thickness of 100  $\mu\text{m}$ , no "smearing" of patterns can be detected.

The drift of patterns with a layer thickness of 100  $\mu\text{m}$  is studied in detail in the following section.

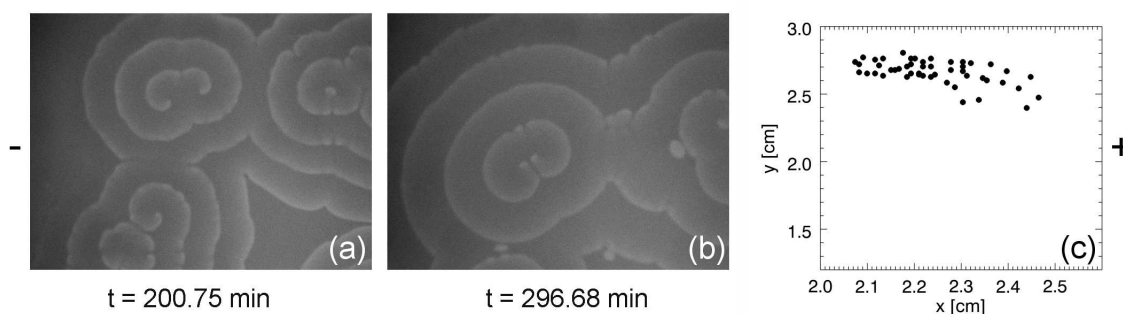


**Fig. 9.3.:** (a) and (b) Drift of patterns in the BP-catalyzed BZ-AOT system with a layer thickness of 100  $\mu\text{m}$ . (c) The tracked trajectory from the left spiral wave of the upper spiral pair after the application of the electric field ( $8.7 \text{ V cm}^{-1}$ ) for 85 min. Concentrations:  $[\text{MA}] = 0.242 \text{ M}$ ,  $[\text{NaBrO}_3] = 0.174 \text{ M}$ ,  $[\text{H}_2\text{SO}_4] = 0.194 \text{ M}$  and  $[\text{BP}] = 6 \text{ mM}$ ,  $\varphi_d = 0.455$ ,  $\omega = 12$ . Image size:  $5.4 \times 4.1 \text{ mm}^2$  [104].

## 9.2. Electric Field Effects in Microemulsions

### 9.2.1. Direct Current

The effect of an electric field on labyrinth-like Turing patterns in a microemulsion of 100  $\mu\text{m}$  thickness is analyzed in the range from  $3.0$  to  $15.7 \text{ V cm}^{-1}$ . The reactant concentrations are equal for all experiments in this section:  $[\text{MA}] = 0.259 \text{ M}$ ,  $[\text{NaBrO}_3] = 0.155 \text{ M}$ ,  $[\text{H}_2\text{SO}_4] = 0.207 \text{ M}$  and  $[\text{ferroin}] = 1.74 \text{ mM}$ ,  $\omega = 18.03$ . For the droplet fraction the values 0.48 and 0.52 are chosen, which are close to the percolation threshold ( $\varphi_d \approx 0.5$ ). However, in both cases Turing patterns can be observed.

The control parameter of the measurements is the electric field strength, since the electric current changes drastically during the measurement [Fig. 9.4(a)]. After switching on the field,

the current increases rapidly up to 250 – 400  $\mu\text{A}$  and subsequently decreases towards 5 – 60  $\mu\text{A}$ . This final value remains almost constant during the rest of the measurement. Whether the maximum of the current lies around 250 or 400  $\mu\text{A}$  and the final value around 5 or 60  $\mu\text{A}$  depends on the used droplet fraction. For  $\varphi_d = 0.48$ , the maximum lies between 250 – 300  $\mu\text{A}$  and the final value at around 5 – 25  $\mu\text{A}$ , whereas above the percolation transition ( $\varphi_d = 0.52$ ) the peak reaches 350 to 400  $\mu\text{A}$  and the final value lies between 30 and 60  $\mu\text{A}$ .

The current in the microemulsion always decreases very slowly, but continuously, which allows the measurement of the patterns' drift velocity as a function of the electric current [Fig. 9.4(b)]. The continuous decrease of the current makes the estimation of the drift velocity challenging, since it requires a linear part of a line in the corresponding time-space plot. Thus, the quality of the time-space plot determines the estimation of the pattern's drift velocity.

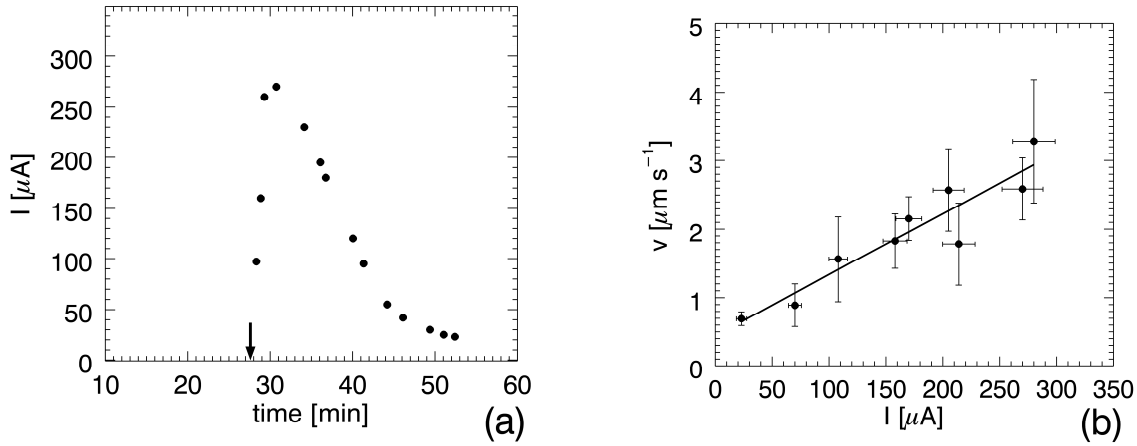


**Fig. 9.4.:** (a) Course of current during a measurement for  $\varphi_d = 0.52$ . After switching on the constant electric field (arrow), the current increases quickly and subsequently decreases slowly, until it reaches a final value. (b) Drift velocity of Turing patterns versus the electric current. The velocity is measured in a time interval between 100 and 600 s during the period of current decrease (declining part of (a)). A linear fit has been computed with a correlation coefficient of 0.934 [105].

In Fig. 9.5 snapshots of labyrinth-like Turing patterns are shown, drifting towards the positive electrode located at the left side of the figure, when an electric field is applied. The labels mark certain positions in the image to illustrate the pattern drift. Label "A" and label "B" mark the same position at different instants of time. They are connected through an inclined black line to clarify the drift. Label "B" marks the projection of label "B" in (a). From these images, a horizontal time-space plot is constructed along the horizontal black line [Fig. 9.6]. The positive slope of the bright lines between the two arrows is caused by a drift towards the positive electrode at a field strength of  $8.7 \text{ V cm}^{-1}$  (compare Fig. 9.6). After switching the polarity of the field, the patterns change their drift direction immediately. The magnitude of the slope of both lines is equal, with opposite signs. This shows, that the drift behaves linearly during a measurement,



given that the current is constant.

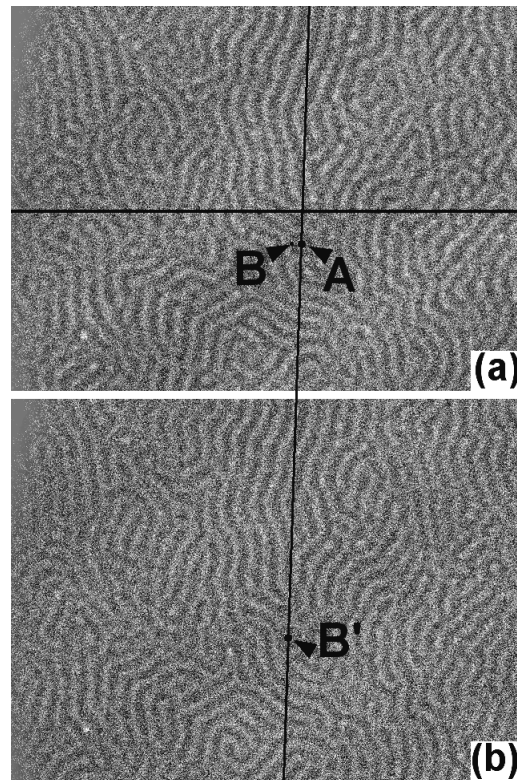


**Fig. 9.5.:** Two snapshots of drifting Turing patterns at  $E = 8.7 \text{ V cm}^{-1}$  with  $\varphi_d = 0.48$  at different instants of time. A time-space plot is extracted along the horizontal line in (a) [Fig. 9.6]. Patterns are drifting towards the positive electrode, which is located at the left side of the image. (a) Label "A" marks the position of a bright spot in the image at  $t = 55.3 \text{ min}$ . Label "B" marks the position of the same spot at  $t = 63.7 \text{ min}$ . (b) Here, label "B'" marks the same bright spot as the one labeled "A", but at another position. Label "B'" and "A" are connected through the inclined line. Image size:  $4.2 \times 3.1 \text{ mm}^2$  [105].

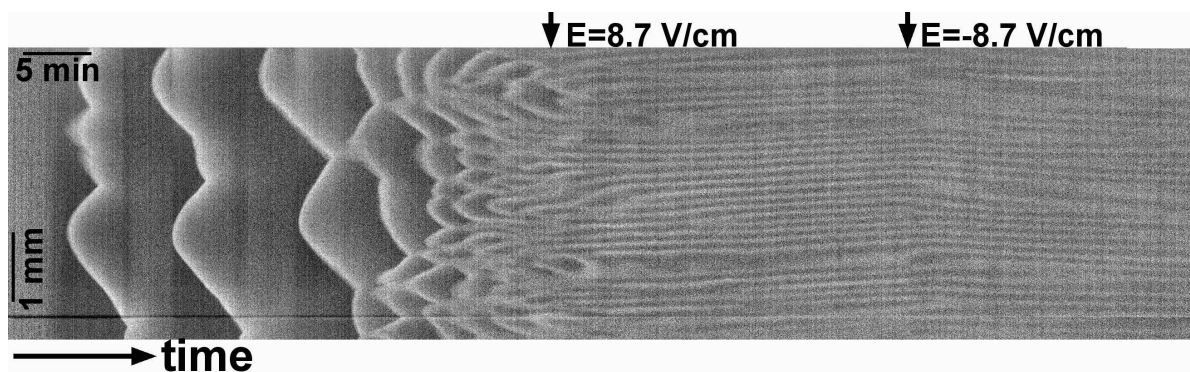


**Fig. 9.6.:** Time-space plot of drifting Turing patterns with  $\varphi_d = 0.48$ . An electric field is applied when Turing patterns are fully developed (first arrow), causing a drift towards the positive electrode. After 27 min, the polarity is changed (second arrow) and the drift reverses its direction immediately [105].

Turing patterns are found to drift under the influence of the electric field in the microemulsion. However, this drift depends on the droplet fraction [Fig. 9.7]. Above the percolation transition, a linear increase of the drift velocity of Turing patterns with increasing electric field strength

is found (red diamonds in Fig. 9.7). Below the percolation transition, the course of the drift velocity is nonlinear, presumably exponential (black circles), compare Tables B.2 and B.3.

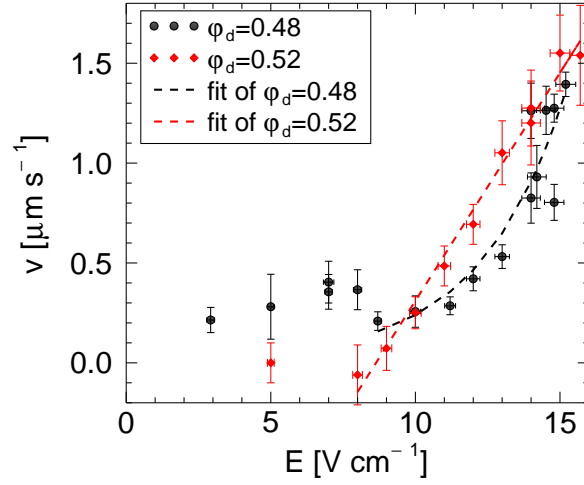


**Fig. 9.7.:** Drift velocity  $v$  of Turing patterns depending on the applied field strength  $E$ . Below the percolation threshold (black circles), an exponential increase of the velocity with increasing field strength is found (correlation coefficient = 0.8382). Above this threshold (red diamonds), a linear behavior is observed, as in the homogeneous system (correlation coefficient = 0.9874). The dashed lines are the fitted curves, respectively. Note, that each data point represents an individual experiment [105].

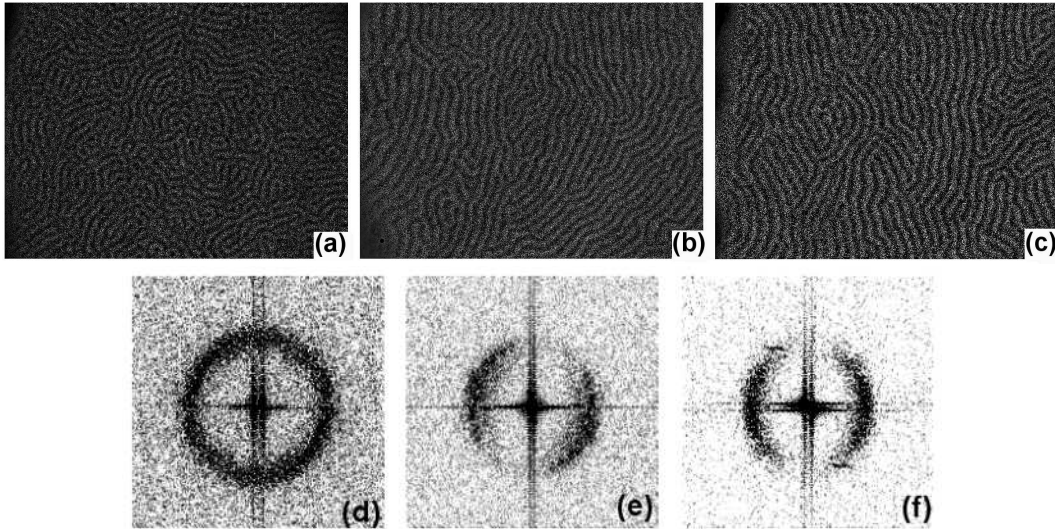


**Fig. 9.8.:** Alignment of Turing patterns at different field strengths for  $\varphi_d = 0.52$ . The cathode is located on the left side and the field lines are oriented horizontally. Turing patterns (a) are randomly oriented at  $5 \text{ V cm}^{-1}$ , (b) show a preferred orientation at  $12 \text{ V cm}^{-1}$  and (c) are oriented almost perpendicular to the field lines at  $15.7 \text{ V cm}^{-1}$ . Image size:  $5.2 \times 3.8 \text{ mm}^2$ . (d-f) Amplitude spectrum of the Turing patterns (a-c) to illustrate the reorientation of the patterns [105].

An exponential fit of the data for the drift velocity below the percolation threshold is performed for electric fields larger than  $8.7 \text{ V cm}^{-1}$ . Lower values of the drift velocity are scattered in the range between  $0.2$  and  $0.4 \mu\text{m s}^{-1}$ . The errors are too large to include these in the exponential

fit. A statistical test [106] is performed to examine, whether a linear or an exponential fit is the better choice for the data points below the percolation transition (Tables B.2 and B.3). In Fig. 9.8, the reorientation of Turing patterns induced by the electric field is shown. For a weak field strength (up to  $5 \text{ V cm}^{-1}$ ), the labyrinth-like structures are randomly oriented without a preferred direction [Fig. 9.8(a)]. A medium strength of the field ( $5 - 12 \text{ V cm}^{-1}$ ) causes a more ordered arrangement of the structures, in which most of them have a certain angle to the horizontal field lines [Fig. 9.8(b)]. Larger values of the field strength (about  $14 \text{ V cm}^{-1}$ ) generate a highly ordered labyrinth-like pattern, with stripes that are oriented almost perpendicular with respect to the field lines [Fig. 9.8(c)]. To illustrate the reorientation, a spatial Fourier transform of these three images is computed to get the amplitude spectrum of the original images [Fig. 9.8(d-f)]. Here it can be seen, that for a low field strength the wavelength distribution is homogeneous around the point of origin [Fig. 9.8(d)]. At a medium field strength, the distribution is not homogeneous anymore, but shows a gap in the upper right (and lower left) corner [Fig. 9.8(e)]. The position of the gap corresponds to the angle between the Turing patterns and the field vector. The gap rotates further with increasing field strength, such that it is located at the top (and bottom) of the ring of the wavelength distribution at high field strengths [Fig. 9.8(f)]. When the gap is located at the top (bottom), the reorientation of the Turing patterns is completed. They are now perpendicular with respect to the field vector. This reorientation occurs in a continuous fashion and is found above and below the percolation threshold.

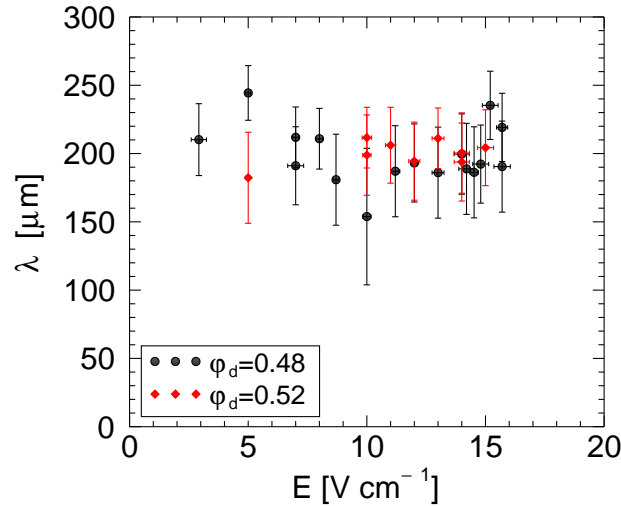


**Fig. 9.9.:** Characteristic wavelength of Turing patterns as a function of the electric field strength with different droplet fractions. Below (black circles) and above the percolation transition (red diamonds) the wavelength of Turing patterns is almost equal [105].

The characteristic wavelength of Turing patterns with different field strengths is shown in Fig.

9.9. Here, the wavelength above and below the percolation transition is estimated. For both situations, the wavelength is almost equal and lies around 200  $\mu\text{m}$ . Even the reorientation and thus, the electric field do not affect the values of the wavelength.

### 9.2.2. Alternating Current

For the experiments with alternating current (AC) a layer thickness of 100  $\mu\text{m}$  is used. Three different wave forms are taken: sine, rectangle and short pulses. The frequency is varied between 0.001 and 11.3 Hz. An overview is given in Table 9.1. In most experiments a rectangular wave form is used. In these cases, the droplet fraction is changed. However, a significant effect on the pattern drift caused by the alternating field could not be found.

**Table 9.1.:** Overview of measurements using alternating electric fields, with a sine, pulse and rectangular wave form and the used frequencies. The frame rate is adopted to the used frequencies and the time column gives the time, when the field is switched on after starting the experiment.

wave form	$\varphi_d$	frequency [Hz]	frame rate [Hz]	time [min]
sine	0.48	0.010	0.9902	39.5
sine	0.48	0.001	0.9902	37.1
sine	0.48	0.020	0.9902	38.2
rectangle	0.48	0.020	0.9902	44.3
rectangle	0.48	0.002	0.4951	45.1
rectangle	0.48	0.005	0.9902	40.1
rectangle	0.48	10.000	11.3154	20.2
rectangle	0.48	10.000	11.3154	26.0
rectangle	0.48	0.001	0.9902	18.3
rectangle	0.52	0.020	0.9902	21.3
rectangle	0.52	0.005	0.9902	18.3
rectangle	0.52	0.050	0.9902	19.4
rectangle	0.52	0.050	0.9902	22.7
pulse	0.48	4.000	5.0200	33.4
pulse	0.48	1.000	1.9802	23.1
pulse	0.48	0.100	0.4951	34.7
pulse	0.48	0.200	0.4951	35.8

In Fig. 9.10 an example of an experiment with AC and a frequency of 0.05 Hz (rectangular wave form) is shown. With that particular frequency, the direction of the field changes every 10 sec.

Since the voltage changes between -10 V and 10 V, the electric field strength changes between  $-4 \text{ V cm}^{-1}$  and  $4 \text{ V cm}^{-1}$  (distance between electrodes is 2.5 cm).

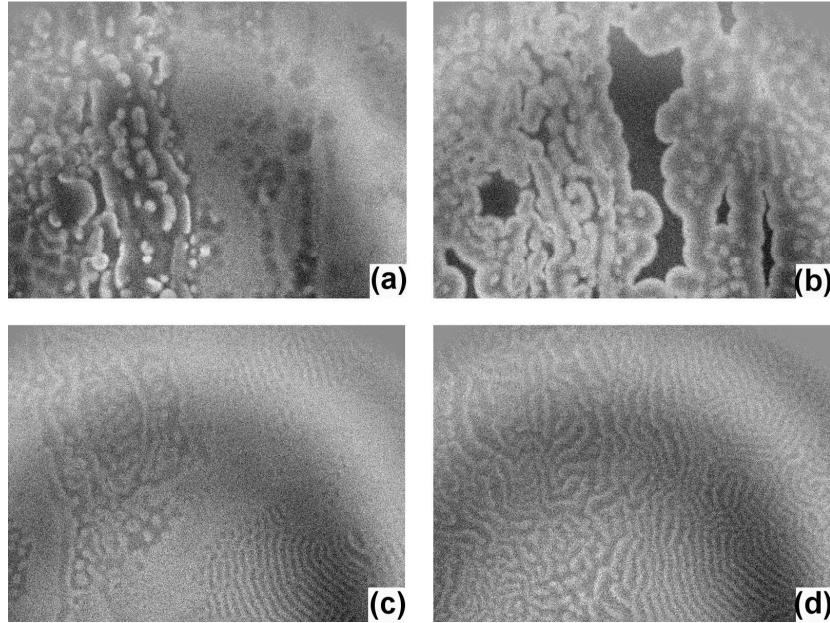


**Fig. 9.10.:** Development of Turing patterns with alternating electric fields (rectangular wave form) with  $\varphi_d = 0.52$  at (a) 12.7 min, (b) 15.8 min, (c) 60.2 min and (d) 70.5 min after starting the experiment. The applied frequency of the field is 0.05 Hz and the field is switched on at 22.7 min. As long as pattern development is not finished some regimes without any structures remain (a) and (c). In these regimes the patterns develop later and remain with a larger wavelength compared to the early-developed patterns (d). Image size:  $6.4 \times 4.8 \text{ mm}^2$ .

In Fig. 9.10(c) and (d) different wavelengths of the Turing patterns can be observed in the monitored area of the experiment. On the left side, the wavelength is larger (i. e.,  $(280 \pm 20) \mu\text{m}$ ) than on the right side ( $(160 \pm 13) \mu\text{m}$ ). In (c) the regimes of different wavelength are separated by areas without any patterns. These areas get smaller in the course of the experiment and two different wavelengths remain.

Regimes without patterns are observed in almost all experiments with AC, however, different wavelengths are unusual.

### 9.3. Discussion

Patterns in the BZ reaction are known to drift under the influence of an electric field [48, 107] and this drift can also be found in microemulsions [80]. However, the effect of electric fields in the latter system is hardly studied. In this chapter, the effect of an electric field with direct and alternating current on patterns in a microemulsion is analyzed.

First, the layer thickness of the ferroin- and BP-catalyzed emulsion is varied. Electrodes of  $100 \mu\text{m}$  and  $220 \mu\text{m}$  are used. The layer thickness of  $220 \mu\text{m}$  lies in the range of the characteristic

wavelength of the studied Turing pattern. This yields three-dimensional effects of pattern formation. The structures are blurred and have no distinct shape. The same holds true for the BP-catalyzed system. However, when switching on the electric field in the BP-catalyzed system, the wave structures smear, since they are drifting in opposite directions, whereas the patterns in a 100  $\mu\text{m}$  thick layer drift into one direction with a constant velocity. In contrast, Turing patterns drift almost equal in 100  $\mu\text{m}$  and 220  $\mu\text{m}$  thick layers.

The "smearing" of patterns in the thick layer might be a consequence of the hydrophobic character of BP. The molecules are located mostly at the AOT shell [66], which could effect the distribution of the charge carriers. Both catalysts (ferroin and BP) have two positive charges in their reduced state. When the catalyst is located in the water phase, the positive charges will not have much effect due to the large number of other free charges in the water phase (i. e., protons). However, when the catalyst is located at the AOT shell, the positive charges may lead to a drift towards the negative electrode in the electric field. Probably, the 100  $\mu\text{m}$  thick layer does not provide enough vertical space for the clustered droplets in the BP-catalyzed system to be able to drift towards the negative electrode. Thus, a smearing of patterns in the BP-catalyzed microemulsion can just be observed with a layer thickness larger than 100  $\mu\text{m}$ .

Using DC, the measured current in the microemulsion changes during the experiment. After switching on the electric field, the current increases rapidly up to 250 – 400  $\mu\text{A}$  and decreases to 5 or 60  $\mu\text{A}$ . However, the value of the maximum and final values depends on the droplet fraction. For  $\varphi_d = 0.48$ , the current lies between 250 and 300  $\mu\text{A}$  and the final value between 5 and 25  $\mu\text{A}$ . Above the percolation transition ( $\varphi_d = 0.52$ ) the peak reaches 350 to 400  $\mu\text{A}$  and the final value lies between 30 and 60  $\mu\text{A}$ .

The temporal evolution of the current can be explained by the large number of free charge carriers, such as  $\text{Br}^-$  ions (located in the oil phase),  $\text{SO}_3^-$  and  $\text{Na}^+$  (ions from the surfactant, located in the water phase). After switching on the electric field, the negatively charged ions follow the field immediately, until most of them reach the positive electrode. When reaching the final value of the current, only newly produced ions can follow the electric field. If these ions are trapped in the water droplets (below the percolation transition), they move much slower than ions, which can move freely through the water channels (above the percolation transition). Therefore, the flux of charge carriers should be higher above than below the percolation transition.

The behavior of the current is also well correlated with the electric conductivity  $\sigma$  of the system, which is almost one order of magnitude larger for  $\varphi_d = 0.52$  than for  $\varphi_d = 0.48$  (compare Fig. 6.1). The higher the conductivity the higher the value for the electric current.

In the aqueous BZ system, the drift velocity of patterns depends linearly on the field strength or

on the electric current [48, 107], which is also true for the chlorine dioxide-iodine-malonic acid reaction [25].

However, in microemulsions the course of the pattern drift velocity depends on the droplet fraction [Fig. 9.7] and thus, on the percolation process. Above the percolation transition, a linear increase in drift velocity with increasing field strength is found. Here, the electric current can flow directly through the water channels and one observes the same linear behavior as in the homogeneous system [Fig. 9.7] [48, 107]. Below the threshold, a more rapid increase of the velocity with increasing field strength is found from 8.7 to 15.7 V cm<sup>-1</sup>. This increase is primarily nonlinear, justifying an empirical exponential fit in the measured range. With higher field strengths, this exponential function might become linear, when the system is percolated due to the electric field. However, there is no appropriate theory explaining such an exponential behavior.

Interestingly, this exponential increase was not found by Carballido-Landeira et. al. [80]. They studied drifting Turing spots up to  $\varphi_d = 0.56$  and found a linear dependence of the drift velocity on the electric field. However, the largest field strength they used was 10 V cm<sup>-1</sup> [80].

The values of the drift velocity at high electric field strength ( $> 14$  V cm<sup>-1</sup>, [Fig. 9.7]) are almost equal for both used droplet fractions (i. e., below and above the percolation transition). This might be attributed to electric-field induced percolation.

Above the percolation transition, patterns do not start to move until the field strength reaches 9 V cm<sup>-1</sup>. Within the range of  $9 \text{ V cm}^{-1} \leq E \leq 14 \text{ V cm}^{-1}$  the maximally reached current exceeds that below the percolation transition. This indicates, that the ion flux is higher above the transition and provides a hint, that the current is governed by the ions in the water phase. Thus, bromide ions add only a small contribution to the electric current.

Structural changes in the microemulsion, induced by the electric field appear to be responsible for the observed nonlinear velocity increase. Due to the action of the field, the nanodroplets become more elongated and polarized (mediated by dissociation into  $\text{SO}_3^-$  and  $\text{Na}^+$ ) [65, 85], thus forming droplet clusters. In these clusters, the monolayer of AOT molecules opens up and water molecules can diffuse from one droplet within the cluster into an adjacent one [84]. As a result, the conductivity of the microemulsion increases [65]. This might be a case of the so-called electric-field induced percolation.

This effect may also be the reason for the reorientation of the patterns in Fig. 9.8.

Moreover, in other systems, like in the polyacrylamide methyleneblue-sulfide-oxygen reaction (PA-MBO), the orientation of Turing patterns is found to change with the strength of the electric field. In this system, a weak electric field (up to 5 V cm<sup>-1</sup>) leads to a parallel orientation

to the field, whereas fields above  $10 \text{ V cm}^{-1}$  produce patterns, which are oriented perpendicular to the field vector [108].

Experiments with alternating electric fields do not show any effect on pattern movement. Three different wave forms are used: sine, rectangle and pulses in a  $100 \text{ }\mu\text{m}$  thick ferroin-catalyzed microemulsion. Frequencies of the field between  $0.001$  and  $11.3 \text{ Hz}$  are used. Nevertheless, a drift of Turing patterns cannot be observed in any case. For a reaction of the system on a sine wave form and/or high frequencies, the microemulsion is too inert. However, frequencies in the range of  $0.001 \text{ Hz}$  are expected to at least show a change in the drift direction as it is observed for static fields in Fig. 9.6. A reason might be, that the electric field strength is too low to observe a drift, since it changes between  $-4 \text{ V cm}^{-1}$  and  $4 \text{ V cm}^{-1}$ . In this regime, patterns exposed to DC fields show no prominent drift. Nevertheless, the patterns move under the influence of an electric gradient.

Furthermore, alternating electric fields have an effect on the evolution of Turing patterns as shown in Fig. 9.10. Some regimes remain homogeneous (i. e., without any patterns) for a short time after the application of the field. Additionally, different wavelengths of the Turing patterns can be observed at the same time. Regimes without patterns are found in almost all experiments with AC, but not in any of the DC cases.

In the past, some experiments with AC in aqueous BZ reaction were performed as predicted in Ref. [52]. Here, the system behaves equally for AC and DC, independent of the frequency [52].



## **Part V.**

# **Conclusion and Outlook**



---

Microemulsions show a fascinating variety of patterns; starting with Turing patterns which play an important role in biological morphogenesis and ending with gradient fields, affecting the diffusion of ions and thus the communication between compartments.

In this study, a mechanism for the effect of two different hydrocarbon solvents on pattern formation is suggested. This was previously thought not to be important for pattern formation in microemulsion systems.

In the ferroin-catalyzed system, the way Turing patterns emerge is quite different for both solvents. In n-octane, bulk oscillations merge with evolving Turing patterns, forming a new excitation front, which splits up and propagates into two opposite directions: towards the existing patterns and away from them. In hexane, however, the bulk oscillation stops in front of the existing patterns and forms a new ring of excitation around the structures.

Furthermore, in microemulsions long-range interactions can be expected to occur, since the inhibitor diffuses into the oil phase. This is observable in hexane, where the bulk oscillation stops, in front of the emerging Turing patterns. This type of interactions is also observed with BP. A representative observation is the phenomenon that rotating waves and bubble waves propagate much slower towards the dash wave front than into the other directions. This underlines the complexity of the studied system and therefore, makes it an interesting model case for complexity, in particular for biological morphogenesis.

Changing the organic substrate in the aqueous BZ reaction yields anomalous dispersion [22, 35]. This phenomenon is coupled to the BZ-AOT system, such that a new system is developed, showing new patterns. This newly developed system shows behavior of the aqueous BZ reaction, either with malonic acid and CHD, as well as some aspects of the standard BZ-AOT system. It is expectable that still plenty of patterns remain to be observed in the BZ-AOT system with CHD. Further experiments should include higher excitabilities and a variance in  $\omega$  and droplet fractions, to observe structures in the system far away from the percolation threshold.

Furthermore, the effect of an electric field on labyrinth-like Turing patterns is investigated below and above the percolation transition. Below this transition, a nonlinear increase of the drift velocity with increasing electric field strength is found. This may be due to the phenomenon of electric-field induced percolation. However, until now this type of percolation has only been reported for high electric fields (in the range of  $\text{kV cm}^{-1}$ ) in a microemulsions without chemical reactions [59]. In microemulsions loaded with the BZ-reaction, a much higher amount of ions is present. This may lead to an earlier start of the percolation at weaker electric field strengths than that reported in Ref. [59]. With the onset of percolation, all chemical species can migrate faster than below percolation, since they can flow through the water channels. This leads to an

---

increase in the conductivity and hence, the ion flux.

The exponential relation between the electric field strength and the drift velocity (below the percolation threshold) of Turing patterns is verified by statistical tests. The correlation coefficient of a linear fit is found to be smaller than that of an exponential fit on a significance level of 99 %. Above the percolation transition, a linear behavior of the drift velocity prevails, as known from aqueous systems.

Another important finding is the reorientation of the labyrinth-like patterns at high electric field strengths, as observed below and above the percolation transition. In living cells, electric fields can also induce a reorientation of the cells due to the induction of dipoles [109]. The results presented here emphasize the complexity of the BZ-AOT system, as suggested by the assumed exponential increase of the drift velocity. This should motivate a more detailed investigation of the physical properties of pattern forming microemulsions by further experimental and theoretical efforts.

Especially the application of the studied system on biological cells is very promising, since many properties of cells are already fulfilled: the communication between droplets (compartments) and long-range interactions between them. This type of interaction between compartments based on a self-induced (chemical) gradient is the way biological cells communicate.

Especially, studying Turing patterns might create a better understanding of morphogenesis. It is quite surprising that such small compartments can create a pattern with a wavelength several orders of magnitude larger than the compartments themselves. It is very interesting that so many different aspects of biological systems can be studied in the BZ-AOT system. Indeed, this system is full of surprises.

# Bibliography

- [1] A. M. Turing. “The Chemical Basis of Morphogenesis”. *Phil. Trans. R. Soc. Lond. B* **237** (641), 37 (1952).
- [2] A. T. Winfree. “Electrical turbulence in three-dimensional heart muscle”. *Science* **266** (5187), 1003 (1994).
- [3] F. H. Fenton, E. M. Cherry, H. M. Hastings, and S. J. Evans. “Multiple mechanisms of spiral wave breakup in a model of cardiac electrical activity”. *Chaos* **12** (3), 852 (2002).
- [4] G. Gerisch and B. Hess. “Cyclic-AMP-Controlled Oscillations in Suspended Dictyostelium Cells: Their Relation to Morphogenetic Cell Interactions”. *Proc. Nat. Acad. Sci.* **71** (5), 2118 (1974).
- [5] N. A. Gorelova and J. Bureš. “Spiral waves of spreading depression in the isolated chicken retina”. *J. Neurobiol.* **14** (5), 353 (1983).
- [6] J. Lechleiter, S. Girard, E. Peralta, and D. Clapham. “Spiral calcium wave propagation and annihilation in *Xenopus laevis* oocytes”. *Science* **252** (5002), 123 (1991).
- [7] M. T. Lippert et al. “Methods for Voltage-Sensitive Dye Imaging of Rat Cortical Activity With High Signal-to-Noise Ratio”. *J. Neurophysiol.* **98** (1), 502 (2007).
- [8] M. A. Dahlem and S. C. Müller. “Migraine aura dynamics after reverse retinotopic mapping of weak excitation waves in the primary visual cortex”. *Biol. Cybern.* **88** (6), 419 (2003).
- [9] B. P. Belousov. “A periodic reaction and its mechanism”. *Collection of short papers on radiation medicine for 1958*. Med. Publ., Moscow, 1959.
- [10] A. N. Zaikin and A. M. Zhabotinsky. “Concentration Wave Propagation in Two-dimensional Liquid-phase Self-oscillating System”. *Nature* **225** (5232), 535 (1970).
- [11] R. J. Field, E. Körös, and R. M. Noyes. “Oscillations in chemical systems. II. Thorough analysis of temporal oscillation in the bromate-cerium-malonic acid system”. *J. Am. Chem. Soc.* **94** (25), 8649 (1972).
- [12] Q. Ouyang et al. “Bubble-free Belousov-Zhabotinskii-type reactions”. *J. Phys. Chem.* **91** (8), 2181 (1987).

- [13] V. Castets, E. Dulos, J. Boissonade, and P. De Kepper. “Experimental evidence of a sustained standing Turing-type nonequilibrium chemical pattern”. *Phys. Rev. Lett.* **64** (24), 2953 (1990).
- [14] V. K. Vanag and I. R. Epstein. “Pattern Formation in a Tunable Medium: The Belousov-Zhabotinsky Reaction in an Aerosol OT Microemulsion”. *Phys. Rev. Lett.* **87** (22), 228301 (2001).
- [15] S. Kondo and T. Miura. “Reaction-Diffusion Model as a Framework for Understanding Biological Pattern Formation”. *Science* **329** (5999), 1616 (2010).
- [16] V. K. Vanag and I. R. Epstein. “Patterns of Nanodroplets: The Belousov-Zhabotinsky-Aerosol OT-Microemulsion System”. *Self-Organized Morphology in Nanostructured Materials*. Ed. by K. Al-Shamery and J. Parisi. Vol. 99. Springer Series in Materials Science. Springer, Berlin, Heidelberg, 2008, pp. 89–113. ISBN: [978-3-540-72674-6](#).
- [17] G. Nicolis and A. De Wit. “Reaction-diffusion systems”. *Scholarpedia* **2** (9), 1475 (2007). revision #137222.
- [18] M. C. Cross and P. C. Hohenberg. “Pattern formation outside of equilibrium”. *Rev. Mod. Phys.* **65** (3), 851 (1993).
- [19] A. T. Winfree. *The geometry of biological time*. 2nd. Vol. 12. Interdisciplinary Applied Mathematics. New York: Springer-Verlag, 2001.
- [20] V. S. Zykov. “Excitable media”. *Scholarpedia* **3** (5), 1834 (2008).
- [21] J. Ross, S. C. Müller, and C. Vidal. “Chemical Waves”. *Science* **240** (4851), 460 (1988).
- [22] N. Manz, S. C. Müller, and O. Steinbock. “Anomalous Dispersion of Chemical Waves in a Homogeneously Catalyzed Reaction System”. *J. Phys. Chem. A* **104** (25), 5895 (2000).
- [23] J. J. Tyson and J. P. Keener. “Singular perturbation theory of traveling waves in excitable media (a review)”. *Physica D* **32** (3), 327 (1988).
- [24] I. Lengyel and I. R. Epstein. “Modeling of Turing Structures in the Chlorite-Iodide-Malonic Acid-Starch Reaction System”. *Science* **251** (4994), 650 (1991).
- [25] B. Schmidt, P. De Kepper, and S. C. Müller. “Destabilization of Turing Structures by Electric Fields”. *Phys. Rev. Lett.* **90** (11), 118302 (2003).
- [26] M. Menzinger and A. Rovinsky. *Chemical Waves and Patterns*. Ed. by R. Kapral and K. Showalter. Kluwer, Dordrech, 1995, p. 89.

- [27] R. M. Noyes, R. Field, and E. Körös. “Oscillations in chemical systems. I. Detailed mechanism in a system showing temporal oscillations”. *J. Am. Chem. Soc.* **94** (4), 1394 (1972).
- [28] R. J. Field and R. M. Noyes. “Oscillations in chemical systems. IV. Limit cycle behavior in a model of a real chemical reaction”. *J. Chem. Phys.* **60** (5), 1877 (1974).
- [29] M. L. Smoes. “Period of homogeneous oscillations in the ferroin-catalyzed Zhabotinskii system”. *J. Chem. Phys.* **71** (11), 4669 (1979).
- [30] A. F. Taylor, B. R. Johnson, and S. K. Scott. “Effect of oxygen on wave propagation in the ferroin-catalysed Belousov-Zhabotinsky reaction”. *J. Chem. Soc., Faraday Trans.* **94** (8), 1029 (1998).
- [31] A. F. Taylor, B. R. Johnson, and S. K. Scott. “Scroll waves in the Belousov-Zhabotinsky reaction: exploitation of O-2-effect on the ferroin-catalysed system”. *Phys. Chem. Chem. Phys.* **1** (5), 807 (1999).
- [32] K. Kurin-Csörgei, I. Szalai, and E. Körös. “The 1,4-cyclohexanedione-bromate-acid oscillatory system. II. Chemical Waves”. *React. Kinet. Catal. Lett.* **54** (1), 217 (1995).
- [33] K. Kurin-Csörgei, A. M. Zhabotinsky, M. Orbán, and I. R. Epstein. “Bromate-1,4-Cyclohexanedione-Ferroin Gas-Free Oscillating Reaction. 1. Basic Features and Crossing Wave Patterns in a Reaction-Diffusion System without Gel”. *J. Phys. Chem.* **100** (13), 5393 (1996).
- [34] I. Szalai, K. Kurin-Csörgei, I. R. Epstein, and M. Orbán. “Dynamics and Mechanism of Bromate Oscillators with 1,4-Cyclohexanedione”. *J. Phys. Chem. A* **107** (47), 10074 (2003).
- [35] C. T. Hamik, N. Manz, and O. Steinbock. “Anomalous Dispersion and Attractive Pulse Interaction in the 1,4-Cyclohexanedione Belousov-Zhabotinsky Reaction”. *J. Phys. Chem. A* **105** (25), 6144 (2001).
- [36] J. D. Dockery, J. P. Keener, and J. J. Tyson. “Dispersion of traveling waves in the belousov-zhabotinskii reaction”. *Physica D* **30** (1-2), 177 (1988).
- [37] C. T. Hamik and O. Steinbock. “Excitation waves in reaction-diffusion media with non-monotonic dispersion relations”. *New J. Phys.* **5** (1), 58 (2003).
- [38] G. Bordyugov et al. “Anomalous dispersion in the Belousov-Zhabotinsky reaction: Experiments and modeling”. *Physica D* **239** (11), 766 (2010).
- [39] R. J. Field. “Oregonator”. *Scholarpedia* **2** (5), 1386 (2007). revision #91613.

- [40] J. J. Tyson. “A quantitative account of oscillations, bistability, and traveling waves in the Belousov-Zhabotinsky reaction”. *Oscillations and Traveling Waves in Chemical systems*. Ed. by R. J. Field and M. Burger. John Wiley & Sons, New York, 1985.
- [41] J. J. Tyson and P. C. Fife. “Target patterns in a realistic model of the Belousov–Zhabotinskii reaction”. *J. Chem. Phys.* **73** (5), 2224 (1980).
- [42] G. R. Armstrong, A. F. Taylor, S. K. Scott, and V. Gaspar. “Modelling wave propagation across a series of gaps”. *Phys. Chem. Chem. Phys.* **6** (19), 4677 (2004).
- [43] P. K. Becker and R. J. Field. “Stationary concentration patterns in the Oregonator model of the Belousov-Zhabotinskii reaction”. *J. Phys. Chem.* **89** (1), 118 (1985).
- [44] V. K. Vanag. “Waves and patterns in reaction-diffusion systems. Belousov-Zhabotinsky reaction in water-in-oil microemulsions”. *Physics-Uspekhi* **47** (9), 923 (2004).
- [45] H. Ševčíková and M. Marek. “Chemical front waves in an electric field”. *Physica D* **13** (3), 379 (1984).
- [46] H. Ševčíková, M. Marek, and S. C. Müller. “The Reversal and Splitting of Waves in an Excitable Medium Caused by an Electrical Field”. *Science* **257** (5072), 951 (1992).
- [47] R. Kapral and K. Showalter. *Chemical Waves and Patterns*. Kluwer, Dordrecht, 1995.
- [48] O. Steinbock, J. Schütze, and S. C. Müller. “Electric-field-induced drift and deformation of spiral waves in an excitable medium”. *Phys. Rev. Lett.* **68** (2), 248 (1992).
- [49] B. Schmidt and S. C. Müller. “Forced parallel drift of spiral waves in the Belousov-Zhabotinsky reaction”. *Phys. Rev. E* **55** (4), 4390 (1997).
- [50] J. Schütze, O. Steinbock, and S. C. Müller. “Forced vortex interaction and annihilation in an active medium”. *Nature* **356** (6364), 45 (1992).
- [51] V. Perez-Muñuzuri et al. “Super-spiral structures in an excitable medium”. *Nature* **353**, 740 (1991).
- [52] V. Pérez-Muñuzuri, R. Aliev, B. Vasiev, and V. I. Krinsky. “Electric current control of spiral wave dynamics”. *Physica D* **56** (2), 229 (1992).
- [53] A. P. Muñuzuri et al. “Parametric resonance of a vortex in an active medium”. *Phys. Rev. E* **50** (5), 4258 (1994).
- [54] C. Luengviriya, S. C. Müller, and M. J. B. Hauser. “Reorientation of scroll rings in an advective field”. *Phys. Rev. E* **77** (1), 015201 (2008).
- [55] C. Luengviriya and M. J. B. Hauser. “Stability of scroll ring orientation in an advective field”. *Phys. Rev. E* **77** (5), 056214 (2008).



- 
- [56] J. F. Tutz, H. Engel, and O. Steinbock. “Spatial Confinement Causes Lifetime Enhancement and Expansion of Vortex Rings with Positive Filament Tension”. *Arxiv preprint* **1401.6550** (2014).
- [57] M. Kotlarchyk, S.-H. Chen, and J. S. Huang. “Critical behavior of a microemulsion studied by small-angle neutron scattering”. *Phys. Rev. A* **28** (1), 508 (1983).
- [58] Y. Feldman, N. Kozlovich, I. Nir, and N. Garti. “Dielectric relaxation in sodium bis (2-ethylhexyl) sulfosuccinate-water-decane microemulsions near the percolation temperature threshold”. *Phys. Rev. E* **51** (1), 478 (1995).
- [59] G. Ilgenfritz and F. Runge. “Electric field induced percolation in microemulsions: simulation of the electric conductivity”. *Physica A* **181** (1), 69 (1992).
- [60] H.-F. Eicke and J. Naudts. “Non-linear field effects due to activation-energy-controlled charge transport in microemulsions”. *Chem. Phys. Lett.* **142** (1–2), 106 (1987).
- [61] L. Schlicht et al. “Temperature-, electric field- and solute-induced percolation in water-in-oil microemulsions”. *Biophysical Chemistry* **58** (1-2), 39 (1996).
- [62] V. K. Vanag and I. R. Epstein. “Pattern formation in a tunable medium: The Belousov-Zhabotinsky reaction in an aerosol OT microemulsion”. *Phys. Rev. Lett.* **87** (22), 228301 (2001).
- [63] A. Maitra. “Determination of size parameters of water-Aerosol OT-oil reverse micelles from their nuclear magnetic resonance data”. *J. Phys. Chem.* **88** (21), 5122 (1984).
- [64] C. Cametti et al. “Electrical conductivity and percolation phenomena in water-in-oil microemulsions”. *Phys. Rev. A* **45** (8), R5358 (1992).
- [65] H.-F. Eicke, M. Borkovec, and B. Das-Gupta. “Conductivity of water-in-oil microemulsions: a quantitative charge fluctuation model”. *J. Phys. Chem.* **93** (1), 314 (1989).
- [66] P. Dähmlow, V. K. Vanag, and S. C. Müller. “Effect of solvents on the pattern formation in a Belousov-Zhabotinsky reaction embedded into a microemulsion”. *Phys. Rev. E* **89** (1), 010902(R) (2014).
- [67] M. Holdefer. *Relative Dielektrizitätskonstante  $\epsilon_r$  (DK-Werte) von flüssigen und festen Medien*. Endress+Hauser Meßtechnik GmbH+Co., 1999.
- [68] V. K. Vanag and I. R. Epstein. “Segmented spiral waves in a reaction-diffusion system”. *Proc. Natl. Acad. Sci. USA.* **100** (25), 14635 (2003).
- [69] V. K. Vanag and I. R. Epstein. “Dash Waves in a Reaction-Diffusion System”. *Phys. Rev. Lett.* **90** (9), 098301 (2003).

- [70] L. Yang, I. Berenstein, and I. R. Epstein. “Segmented waves from a spatiotemporal transverse wave instability”. *Phys. Rev. Lett.* **95** (3), 038303 (2005).
- [71] D. Horváth, V. Petrov, S. K. Scott, and K. Showalter. “Instabilities in propagating reaction diffusion fronts”. *J. Chem. Phys.* **98** (8), 6332 (1993).
- [72] Y. Kuramoto and H. Arakai. *Chemical Oscillations, Waves and Turbulence*. Springer-Verlag, Berlin, 1984.
- [73] M. Markus, G. Kloss, and I. Kusch. “Disordered waves in a homogeneous, motionless excitable medium”. *Nature* **371** (6496), 402 (1994).
- [74] V. S. Zykov, A. S. Mikhailov, and S. C. Müller. “Wave Instabilities in Excitable Media with Fast Inhibitor Diffusion”. *Phys. Rev. Lett.* **81** (13), 2811 (1998).
- [75] A. A. Cherkashin, V. K. Vanag, and I. R. Epstein. “Discontinuously propagating waves in the bathoferroin-catalyzed Belousov–Zhabotinsky reaction incorporated into a microemulsion”. *J. Chem. Phys.* **128** (20), 204508 (2008).
- [76] L. J. Schwartz et al. “Motions of Water, Decane, and Bis(2-ethylhexyl)sulfosuccinate Sodium Salt in Reverse Micelle Solutions”. *Langmuir* **15** (17), 5461 (1999).
- [77] V. K. Vanag and I. R. Epstein. “Dash Waves in a Reaction-Diffusion System”. *Phys. Rev. Lett.* **90** (9), 098301 (2003).
- [78] E. Villar-Álvarez et al. “Modulation of volume fraction results in different kinetic effects in Belousov-Zhabotinsky reaction confined in AOT-reverse microemulsion”. *J. Chem. Phys.* **134** (9), 094512 (2011).
- [79] R. Johannsson, M. Almgren, and J. Alsins. “Fluorescence and phosphorescence study of AOT/water/alkane systems in the L2 reversed micellar phase”. *J. Phys. Chem.* **95** (9), 3819 (1991).
- [80] J. Carballido-Landeira, P. Taboada, and A. P. Muñozuri. “Effect of electric field on Turing patterns in a microemulsion”. *Soft Matter* **8** (10), 2945 (2012).
- [81] R. R. Aliev and K. I. Agladze. “Critical conditions of chemical wave propagation in gel layers with an immobilized catalyst”. *Physica D* **50** (1), 65 (1991).
- [82] D. Stauffer and A. Aharony. *Introduction To Percolation Theory*. Taylor and Francis, London, 1991.
- [83] F. Runge, L. Schlicht, J.-H. Spilgies, and G. Ilgenfritz. “Electric field-induced structure changes in water-in-oil microemulsions: Time-resolved Kerr effect measurements”. *Ber. Bunsenges. Phys. Chem.* **98** (3), 506 (1994).

- [84] Y. Feldman et al. "Mechanism of Transport of Charge Carriers in the Sodium Bis(2-ethylhexyl) Sulfosuccinate-Water-Decane Microemulsion near the Percolation Temperature Threshold". *J. Phys. Chem.* **100** (9), 3745 (1996).
- [85] O. D. Bedford and G. Ilgenfritz. "Electric field effects in AOT w/o microemulsions: Field-induced percolation and dynamics of structure changes". *Progr. Colloid Polym. Sci.* **278**, 692 (2000).
- [86] R. McIlwaine, V. K. Vanag, and I. R. Epstein. "Temperature control of pattern formation in the Ru(bpy)<sub>3</sub><sup>2+</sup>-catalyzed BZ-AOT system". *Phys. Chem. Chem. Phys.* **11** (10), 1581 (2009).
- [87] J. Carballido-Landeira, V. K. Vanag, and I. R. Epstein. "Patterns in the Belousov-Zhabotinsky reaction in water-in-oil microemulsion induced by a temperature gradient". *Phys. Chem. Chem. Phys.* **12** (15), 3656 (2010).
- [88] H.-F. Eicke, R. Hilfiker, and H. Thomas. "Connectivity-controlled charge transport in water-in-oil microemulsions". *Chem. Phys. Lett.* **125** (3), 295 (1986).
- [89] E. Tekle, M. Ueda, and Z. A. Schelly. "Dynamics of electric field induced transient-phase separation in water-in-oil microemulsion". *J. Phys. Chem.* **93** (16), 5966 (1989).
- [90] R. Tóth et al. "Flow-driven instabilities in the Belousov-Zhabotinsky reaction: Modelling and experiments". *Phys. Chem. Chem. Phys.* **3** (6), 957 (2001).
- [91] ITT Visual Information Solutions. *Image Processing in IDL*. ITT Visual Information Solutions, 2009.
- [92] V. K. Vanag and I. R. Epstein. "Inwardly Rotating Spiral Waves in a Reaction-Diffusion System". *Science* **294** (5543), 835 (2001).
- [93] V. K. Vanag and I. R. Epstein. "Stationary and Oscillatory Localized Patterns, and Subcritical Bifurcations". *Phys. Rev. Lett.* **92** (12), 128301 (2004).
- [94] I. R. Epstein et al. "Chemical Oscillators in Structured Media". *Acc. Chem. Res.* **45** (12), 2160 (2012).
- [95] J. M. Koehler and S. C. Müller. "Frozen Chemical Waves in the Belousov-Zhabotinsky Reaction". *J. Phys. Chem.* **99** (3), 980 (1995).
- [96] J. M. Bodet, J. Ross, and C. Vidal. "Experiments on phase diffusion waves". *J. Chem. Phys.* **86** (8), 4418 (1987).
- [97] A. De Wit, D. Lima, G. Dewel, and P. Borckmans. "Spatiotemporal dynamics near a codimension-two point". *Phys. Rev. E* **54** (1), 261 (1996).

- [98] M. Toiya et al. "Synchronization of Chemical Micro-oscillators". *J. Phys. Chem. Lett.* **1** (8), 1241 (2010).
- [99] V. K. Vanag and I. R. Epstein. "Excitatory and inhibitory coupling in a one-dimensional array of Belousov-Zhabotinsky micro-oscillators: Theory". *Phys. Rev. E* **84** (6), 066209 (2011).
- [100] T. Sakurai, E. Mihaliuk, F. Chirila, and K. Showalter. "Design and Control of Wave Propagation Patterns in Excitable Media". *Science* **296** (5575), 2009 (2002).
- [101] Z. Nagy-Ungvarai, A. M. Pertsov, B. Hess, and S. C. Müller. "Lateral instabilities of a wave front in the Ce-catalyzed Belousov-Zhabotinsky reaction". *Physica D* **61** (1-4), 205 (1992).
- [102] Z. Nagy-Ungvarai and S. C. Müller. "Characterization of Wave Front Instabilities in the Belousov-Zhabotinsky Reaction: An Overview". *Int. J. Bifurcat. Chaos* **04** (05), 1257 (1994).
- [103] P. M. Wood and J. Ross. "A quantitative study of chemical waves in the Belousov-Zhabotinsky reaction". *J. Chem. Phys.* **82** (4), 1924 (1985).
- [104] P. Dähmow, C. Luengviriyaya, and S. C. Müller. "Bottom-Up Self-Organization in Supramolecular Soft Matter: Principles and Prototypical Examples of Recent Advances". Ed. by C. S. Müller and J. Parisi. Springer International Publishing, 2015. Chap. Electric Field Effects in Chemical Patterns, p. 65. ISBN: 978-3-319-19410-3.
- [105] P. Dähmow and S. C. Müller. "Nonlinear effects of electric fields in the Belousov-Zhabotinsky reaction dissolved in a microemulsion". *Chaos* **25** (4), 043117 (2015).
- [106] Student. "The Probable Error of a Mean". *Biometrika* **6** (1), 1 (1908).
- [107] K. I. Agladze and P. De Kepper. "Influence of electric field on rotating spiral waves in the Belousov-Zhabotinskii reaction". *J. Phys. Chem.* **96** (13), 5239 (1992).
- [108] A. F. Münster, M. Watzl, and F. W. Schneider. "Two-dimensional Turing-like patterns in the PA-MBO-System and effects of an electric field". *Phys. Scr.* **1996** (T67), 58 (1996).
- [109] J. Teissié. "Effects of electric fields and currents on living cells and their potential use in biotechnology: A survey". *Bioelectrochem. Bioenerg.* **20** (1-3), 133 (1988).

# Appendix

## A.1. Absorption Spectra of the Catalysts

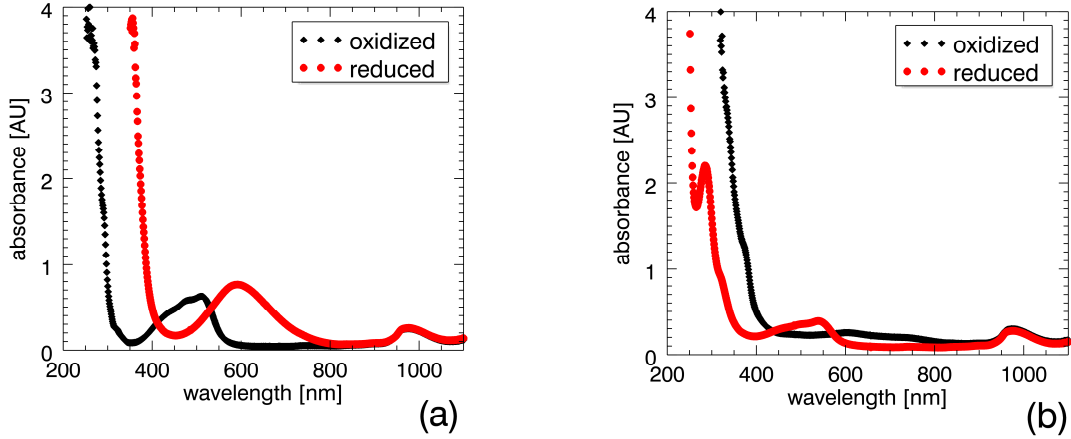


Fig. 11.: Absorption spectra of the used catalysts. (a) Absorption of oxidized and reduced state of ferriin and (b) of BP.

## A.2. Statistical Test of Exponential Increase of Drift Velocity

To test the hypothesis of an exponential correlation between electric field strength and drift velocity at  $\varphi_d = 0.48$  in Fig. 9.7, a linear and an exponential fit of the values between 8.7 and 15.7 V cm<sup>-1</sup> is carried out. The linear one yields a correlation coefficient of 0.7727, whereas the correlation coefficient for the exponential fit is 0.8382. To check whether the found difference is statistically significant, linear and exponential fits of the graph at  $\varphi_d = 0.48$  are computed with two measured values left out for each fit. All possible permutations are considered (see Tables B.2 and B.3).

Using the values in Tables B.2 and B.3, a t-test is done with a significance level of 99 % to test, which of the mean values of the correlation coefficients (linear or exponential) is larger. The null hypothesis is that the correlation coefficients of the linear and the exponential fit are equal. The t-test leads to the result that the null hypothesis is rejected. It turns out that the mean value of the correlation coefficient of the exponential fit is significantly larger than that of the linear fit. More specifically, the correlation coefficients of the exponential fit is higher by at least a value of 0.0491 than the correlation coefficients of the linear fit.

**Table B.2.:** Correlation coefficients of the linear fit of the relationship between drift velocity of Turing patterns and the electric field strength below the percolation transition (data points from Fig. 9.7). The number in the top row gives the first value, which is left out and the number in the left column the second value. Note that for the results on the diagonal only one value is left out.

	1	2	3	4	5	6	7	8	9	10	11	12
1	0.7773	0.7620	0.7286	0.7582	0.7936	0.7899	0.8109	0.7803	0.7737	0.7609	0.8545	0.7480
2	0.7619	0.7352	0.6970	0.7251	0.7582	0.7471	0.7628	0.7370	0.7312	0.7193	0.7969	0.7089
3	0.7286	0.6969	0.7562	0.7561	0.7864	0.7696	0.7817	0.7587	0.7530	0.7423	0.8177	0.7350
4	0.7581	0.7251	0.7561	0.7733	0.8033	0.7865	0.7965	0.7758	0.7697	0.7598	0.8333	0.7531
5	0.7936	0.7582	0.7864	0.8033	0.7976	0.8121	0.8185	0.8010	0.7931	0.7840	0.8607	0.7778
6	0.7899	0.7471	0.7696	0.7865	0.8121	0.7828	0.8007	0.7847	0.7748	0.7652	0.8430	0.7568
7	0.8109	0.7628	0.7817	0.7965	0.8185	0.8007	0.7946	0.7913	0.7982	0.7848	0.8405	0.7818
8	0.7803	0.7369	0.7587	0.7758	0.8010	0.7847	0.7913	0.7730	0.7642	0.7541	0.8309	0.7450
9	0.7737	0.7312	0.7530	0.7697	0.7931	0.7748	0.7982	0.7642	0.7677	0.7508	0.8165	0.7438
10	0.7609	0.7193	0.7423	0.7598	0.7840	0.7652	0.7848	0.7541	0.7508	0.7577	0.8083	0.7286
11	0.8545	0.7969	0.8177	0.8333	0.8607	0.8430	0.8405	0.8309	0.8165	0.8083	0.8252	0.8004
12	0.7480	0.7089	0.7350	0.7531	0.7778	0.7568	0.7818	0.7450	0.7438	0.7286	0.8004	0.7503

**Table B.3.:** Correlation coefficients of the exponential fit of the relationship between drift velocity of Turing patterns and the electric field strength below the percolation transition (data points from Fig. 9.7). The number in the top row gives the first value, which is left out and the number in the left column the second value. Note that for the results on the diagonal only one value is left out.

	1	2	3	4	5	6	7	8	9	10	11	12
1	0.8069	0.7559	0.7647	0.7842	0.8035	0.8107	0.8741	0.8068	0.8073	0.7872	0.9089	0.7629
2	0.7559	0.8113	0.7732	0.7908	0.8093	0.8153	0.8758	0.8112	0.8118	0.7926	0.9095	0.7695
3	0.7647	0.7732	0.8175	0.8001	0.8192	0.8225	0.8770	0.8178	0.8181	0.8001	0.9124	0.7786
4	0.7842	0.7908	0.8001	0.8274	0.8294	0.8318	0.8843	0.8274	0.8279	0.8109	0.9169	0.7912
5	0.8035	0.8093	0.8192	0.8294	0.8404	0.8456	0.8919	0.8407	0.8402	0.8247	0.9286	0.8070
6	0.8107	0.8153	0.8225	0.8318	0.8456	0.8416	0.8918	0.8411	0.8392	0.8235	0.9301	0.8052
7	0.8741	0.8758	0.8770	0.8843	0.8919	0.8918	0.8913	0.8891	0.9073	0.8823	0.9699	0.8614
8	0.8068	0.8112	0.8178	0.8274	0.8407	0.8411	0.8891	0.8373	0.8344	0.8178	0.9255	0.7981
9	0.8073	0.8118	0.8181	0.8279	0.8402	0.8392	0.9073	0.8344	0.8375	0.8173	0.9198	0.7915
10	0.7872	0.7926	0.8001	0.8109	0.8247	0.8235	0.8823	0.8178	0.8173	0.8211	0.9110	0.7676
11	0.9089	0.9095	0.9124	0.9169	0.9286	0.9301	0.9699	0.9255	0.9198	0.9110	0.9218	0.9104
12	0.7629	0.7695	0.7786	0.7912	0.8070	0.8052	0.8614	0.7981	0.7915	0.7676	0.9104	0.8023

### A.3. Experiments with 1,4-cyclohexanedione

**Table C.4.:** Overview of the used concentrations of the reactants, droplet fraction  $\varphi_d$ , the ratio of the reactants  $\varepsilon$ , the duration of the excited state and the resulting pattern in the BZ-AOT system with CHD ( $\omega = 18$ ).

catalyst	NaBrO <sub>3</sub> [M]	H <sub>2</sub> SO <sub>4</sub> [M]	CHD [M]	catalyst [mM]	$\varphi_d$	$\varepsilon$ [M]	duration [min]	Pattern
Ferroin	0.120	0.200	0.250	2.50	0.40	0.096	124.7	transient lines
Ferroin	0.120	0.200	0.250	2.50	0.40	0.096	145.5	transient lines
Ferroin	0.120	0.200	0.230	2.50	0.59	0.104	142.3	transient lines
Ferroin	0.120	0.200	0.230	2.50	0.59	0.104	66.0	transient lines
Ferroin	0.120	0.200	0.230	2.50	0.59	0.104	50.1	transient lines
Ferroin	0.120	0.200	0.230	2.50	0.59	0.104	91.7	transient lines
Ferroin	0.120	0.250	0.200	2.50	0.40	0.150	165.5	transient lines
Ferroin	0.150	0.200	0.100	2.05	0.59	0.300	159.6	wave turbulence
Ferroin	0.150	0.200	0.100	2.05	0.59	0.300	190.7	intermediate state

A.3. EXPERIMENTS WITH 1,4-CYCLOHEXANEDIONE

---

Ferroun	0.150	0.200	0.100	2.05	0.59	0.300	131.2	intermediate state
Ferroun	0.150	0.200	0.100	2.05	0.40	0.300	209.6	wave turbulence
Ferroun	0.150	0.160	0.120	2.05	0.40	0.200	191.3	intermediate state
Ferroun	0.150	0.160	0.120	2.05	0.40	0.200	211.9	intermediate state
Ferroun	0.150	0.160	0.120	2.05	0.59	0.200	183.3	intermediate state
Ferroun	0.150	0.160	0.120	2.05	0.59	0.200	222.5	wave turbulence
Ferroun	0.150	0.160	0.120	2.05	0.59	0.200	185.0	intermediate state
Ferroun	0.155	0.350	0.200	2.05	0.59	0.271	113.8	wave turbulence
Ferroun	0.155	0.350	0.200	2.05	0.59	0.271	124.4	wave turbulence
Ferroun	0.170	0.200	0.230	2.50	0.59	0.148	198.9	intermediate state
Ferroun	0.170	0.200	0.230	2.50	0.59	0.148	157.3	intermediate state
Ferroun	0.170	0.200	0.230	2.50	0.40	0.148	169.3	transient lines
Ferroun	0.170	0.200	0.230	2.50	0.40	0.148	110.4	intermediate state
Ferroun	0.170	0.200	0.230	2.50	0.40	0.148	168.6	intermediate state
Ferroun	0.170	0.250	0.230	2.50	0.40	0.185	179.0	intermediate state
Ferroun	0.230	0.200	0.230	2.50	0.40	0.200	164.4	intermediate state
Ferroun	0.230	0.200	0.230	2.50	0.40	0.200	151.2	intermediate state
Ferroun	0.230	0.160	0.120	2.05	0.40	0.230	179.3	intermediate state
BP	0.120	0.200	0.250	5.00	0.40	0.096	165.5	transient lines
BP	0.120	0.200	0.250	5.00	0.40	0.096	77.6	transient lines
BP	0.120	0.200	0.230	5.00	0.59	0.104	87.1	transient lines
BP	0.120	0.200	0.300	5.00	0.59	0.104	90.0	transient lines
BP	0.150	0.160	0.120	4.10	0.40	0.200	176.2	intermediate state
BP	0.150	0.160	0.120	4.10	0.40	0.200	159.6	intermediate state
BP	0.150	0.160	0.120	4.10	0.59	0.200	158.8	intermediate state
BP	0.150	0.160	0.120	4.10	0.59	0.200	159.6	intermediate state
BP	0.150	0.200	0.100	4.10	0.40	0.300	206.9	wave turbulence
BP	0.155	0.350	0.200	4.10	0.59	0.271	84.0	wave turbulence
BP	0.170	0.200	0.230	5.00	0.59	0.148	108.5	intermediate state
BP	0.170	0.200	0.230	5.00	0.59	0.148	148.2	intermediate state
BP	0.170	0.200	0.230	5.00	0.40	0.148	137.5	wave turbulence
BP	0.200	0.200	0.230	5.00	0.40	0.174	156.1	wave turbulence



---

BP	0.200	0.200	0.230	5.00	0.40	0.174	160.5	wave turbulence
BP	0.200	0.300	0.120	5.00	0.59	0.500	160.8	wave turbulence
BP	0.230	0.200	0.200	2.50	0.40	0.230	154.6	wave turbulence
BP	0.230	0.200	0.230	5.00	0.40	0.200	166.2	wave turbulence
BP	0.230	0.200	0.230	5.00	0.40	0.200	169.9	wave turbulence
BP	0.230	0.200	0.230	5.00	0.40	0.200	184.0	wave turbulence
BP	0.300	0.200	0.230	5.00	0.59	0.261	170.3	wave turbulence
BP	0.300	0.200	0.230	5.00	0.59	0.261	184.9	wave turbulence
BP	0.300	0.200	0.230	5.00	0.40	0.261	133.3	wave turbulence
BP	0.300	0.200	0.230	5.00	0.40	0.261	182.6	wave turbulence

---



# Selbstständigkeitserklärung

Hiermit erkläre ich, dass ich die von mir eingereichte Dissertation zum Thema

**Spatio-temporal pattern formation in microemulsions under different physical and chemical conditions**

selbstständig verfasst, nicht schon als Dissertation verwendet habe und die benutzten Hilfsmittel und Quellen vollständig angegeben wurden.

Weiterhin erkläre ich, dass ich weder diese noch eine andere Arbeit zur Erlangung des akademischen Grades doctor rerum naturalium (Dr. rer. nat.) an anderen Einrichtungen eingereicht habe.

Magdeburg, den 25.08.2015



# Curriculum Vitae

## PERSONAL INFORMATION

Name Patricia Dähmlow  
Date of Birth 04/13/1988  
Place of Birth Magdeburg, Germany  
Nationality german

## SCHOOL EDUCATION

1994 - 1998 "Grundschule Beverspring", Bregenstedt  
1998 - 2000 "Albert Niemann Schule", Erxleben  
2000 - 2007 "Freiherrr-vom-Stein Gymnasium", Weferlingen

## UNIVERSITY EDUCATION

2007 - 2012 **Study of Physics** at the Otto-von-Guericke University  
Magdeburg, Faculty of Natural Sciences  
09/2012 **Diplom**  
Title of Diploma thesis: Twist of Opposite Handedness  
on Scroll Waves (Supervisor: M. J. B. Hauser)  
2012 - 2015 **Doctoral project** at the Otto-von-Guericke University  
Magdeburg, Faculty of Natural Sciences, Germany  
Title of Thesis: Spatio-temporal pattern formation in mi-  
croemulsions under different physical and chemical condi-  
tions (Supervisor: S. C. Müller)